University of Ioannina

School of Sciences

Department of Materials Science and Engineering

Nanostructured High Magnetic Anisotropy Pt-TM (TM=Co,Fe,Cr) Films

Anastasios D. Markou

Doctoral Dissertation

Ioannina 2014

University of Ioannina

School of Sciences

Department of Materials Science and Engineering

Nanostructured High Magnetic Anisotropy Pt-TM (TM=Co,Fe,Cr) Films

Anastasios D. Markou

Doctoral Dissertation

Ioannina 2014

«Η έγκριση της διδακτορικής διατριβής από το Τμήμα Μηχανικών Επιστήμης Υλικών της Σχολής Θετικών Επιστημών του Πανεπιστημίου Ιωαννίνων δεν υποδηλώνει αποδοχή των γνωμών του συγγραφέα Ν. 5343/32, άρθρο 202, παράγραφος 2».

Ημερομηνία αίτησης του κ. Μάρκου Αναστάσιου: 27-1-2009

Ημερομηνία ορισμού Τριμελούς Συμβουλευτικής Επιτροπής: 6-3-2009 (συνεδρία 163 Γ.Σ. ΤΜΕΥ)

Μέλη Τριμελούς Συμβουλευτικής Επιτροπής:
Επιβλέπων
Παναγιωτόπουλος Ιωάννης, Καθηγητής Τμήματος Μηχανικών Επιστήμης Υλικών Πανεπιστημίου Ιωαννίνων
Μέλη
Μπάκας Θωμάς, Καθηγητής Τμήματος Φυσικής Πανεπιστημίου Ιωαννίνων
Eammon Devlin, Ερευνητής Β' Ινστιτούτου Νανοεπιστήμης και Νανοτεχνολογίας Ε.Κ.Ε.Φ.Ε. «Δημόκριτος»

Ημερομηνία ορισμού θέματος: 6-3-2009
«Έλεγχος της νανοδομής και της χημικής τάξης σε υμένια με δομή $L1_0$».

Ημερομηνία Ανασυγκρότησης Τριμελούς Συμβουλευτικής Επιτροπής:
6-2-2013 (συνεδρία 244 Γ.Σ. ΤΜΕΥ)

Μέλη Τριμελούς Συμβουλευτικής Επιτροπής:
Επιβλέπων
Παναγιωτόπουλος Ιωάννης, Καθηγητής Τμήματος Μηχανικών Επιστήμης Υλικών Πανεπιστημίου Ιωαννίνων
Μέλη
Μπάκας Θωμάς, Καθηγητής Τμήματος Φυσικής Πανεπιστημίου Ιωαννίνων
Δούβαλης Αλέξιος, Επίκουρος Καθηγητής Τμήματος Φυσικής Πανεπιστημίου Ιωαννίνων

Τροποποίηση Θέματος: 6-2-2013
«Νανοδομημένα υμένια υψηλής μαγνητικής ανισοτροπίας Pt-TM (TM=Co, Fe, Cr)».
«Nanostructured high magnetic anisotropy Pt-TM (TM=Co, Fe, Cr) Films».

ΔΙΟΡΙΣΜΟΣ ΕΠΤΑΜΕΛΟΥΣ ΕΞΕΤΑΣΤΙΚΗΣ ΕΠΙΤΡΟΠΗΣ : 24-9-2014

1. Παναγιωτόπουλος Ιωάννης, Καθηγητής Τμήματος Μηχανικών Επιστήμης Υλικών Πανεπιστημίου Ιωαννίνων

2. Μπάκας Θωμάς, Καθηγητής Τμήματος Φυσικής Πανεπιστημίου Ιωαννίνων
3. Μπέλτσιος Κωνσταντίνος, Καθηγητής Τμήματος Μηχανικών Επιστήμης Υλικών Πανεπιστημίου Ιωαννίνων
4. Νιάρχος Δημήτριος, Ερευνητής Α Ινστιτούτου Νανοεπιστήμης και Νανοτεχνολογίας Ε.Κ.Ε.Φ.Ε. «Δημόκριτος»
5. Eammon Devlin, Ερευνητής Β' Ινστιτούτου Νανοεπιστήμης και Νανοτεχνολογίας Ε.Κ.Ε.Φ.Ε. «Δημόκριτος»
6. Δούβαλης Αλέξιος, Επίκουρος Καθηγητής Τμήματος Φυσικής Πανεπιστημίου Ιωαννίνων
7. Μπουρλίνος Αθανάσιος, Επίκουρος Καθηγητής Τμήματος Φυσικής Πανεπιστημίου Ιωαννίνων

Έγκριση Διδακτορικής Διατριβής με βαθμό **«ΑΡΙΣΤΑ»** στις 30-10-2014

Ο Πρόεδρος του Τμήματος	**Η Γραμματέας του Τμήματος**
Καρακασίδης Μιχαήλ **Καθηγητής**	**Ξανθή Τουτουνζόγλου**

Table of Contents

Acknowledgements

A marvelous journey has come to an end. It was rich in instructive experiences, sometimes difficult, but unforgettable nonetheless. At this point I would like to express my gratitude towards the academic milieu.

I am deeply grateful to my supervisor Professor Ioannis Panagiotopoulos for his guidance and constant support through this work. Professor Panagiotopoulos is a role model of scientist with never-ending new ideas and I have learned so many things from him.

I would like to give my sincere gratitude to Professor Thomas Bakas for the endless discussions, his valuable tips and the navigation during my first steps in materials science and magnetism.

I am also grateful to the Assistant Professors Alexios Douvalis and Athanasios Bourlinos for their illuminating and helpful discussions and a lot of scientific input.

I would, also, like to thank the other members of my Ph.D. committee who monitored my work and took effort in reading and providing me with valuable comments: Director of research Dr. Dimitris Niarchos, Senior Researcher Dr. Eamonn Devlin and Professor Konstantinos Beltsios.

Professor George Hadjipanayis, Senior Researcher Konstantina Mergia, Assistant Professor Nikos Kourkoumelis, Professor Alexandru Stancu and Assistant Professor Leonidas Gergidis for the TEM, GIXRD, EDX, FORC measurements and micromagnetic calculations, respectively, are thankfully acknowledged.

I would like to thank my colleagues and friends Theofanis Vergos, George Lykoskoyfis and Dr. Christina Papachristodoulou through their competent help, scientific and often non-scientific discussions, created a nice atmosphere both at work and outside the lab.

I would like to thank Dr. A. Polymeros and P. Triantafyllou for their technical support.

Finally, I would like to thank my parents Dimitris and Alexandra Markou for their support, encouragement and understanding over this period.

Abstract

The 3d transition metal alloys are today prospective materials for high density magnetic recording. These include the chemically ordered FePt, CoPt, $CrPt_3$ alloys and the Co/Pt superlattices. The main goal of this work is to provide a comprehensive morphological, structural and magnetic characterization of nanostructured films. The work focuses on four different areas that deal with the optimization of these materials by control of their magnetic anisotropy and microstructural characteristics.

Firstly, the effect of layering and thickness studied in $CrPt_3$ and CoPt films: In films obtained by heat-treatment of bilayers and trilayers (of different Co/Pt content) higher degree of chemical ordering and coercivity can be achieved compared to single layer films. The TEM analysis of Co-Pt films reveals that the twin density in trilayers is larger compared to single layers. The average size of grains in CoPt single layers are 32nm, while the average size of Co/CoPt/Pt trilayers is 42nm.

Secondly, the study of the effect of layering and magnetic annealing on the texture of Co/Pt multilayers shows that the (001) texture sets in as a result of transformation strain driven selective grain growth of (001) at expense of the other possible textures. This correlation between strain and texture is clear only for magnetically annealed samples. This shows that the main function of the applied field is to correlate local strains in a macroscopic level thus increasing their effect along with directly driving the formation of easy axis (001) towards its direction.

Thirdly, the study of switching behavior of regular magnetic FePt nanoislands obtained by sputter deposition of the magnetic layer on monolayers of polystyrene nanospheres (of 970nm and 173nm diameter) used as masks. The nanoislands are magnetically hard and are characterized by non-zero dM-plots. These findings were compared with micromagnetic modeling studies which shows that for anisotropy values high enough to match the observed coercivity, multidomain islands can result in due to the existence of either a softer part or different anisotropy direction part within each magnetic entity.

Finally, the previous approach is extended to the study of magnetization reversal in graded anisotropy Co/Pt multilayers which are deposited both onto nanospheres and Si substrates for comparison. The study was based on First Order Reversal Curve diagrams

(FORC). Using regular nanostructures the following complication that the study of grade anisotropy films presents, can be dealt with if the thickness exceeds a certain limit above which the formation of stripe domains becomes favorable the straight forward interpretation of the effect of the anisotropy profile on the reversal is not possible. It is found that multilayers can be used to create model graded perpendicular anisotropy systems only when lateral domain propagation is suppressed by appropriate nanostructuration.

Περίληψη

Στην παρούσα εργασία πραγματοποιήθηκε ο μορφολογικός, μαγνητικός και δομικός χαρακτηρισμός νανοδομημένων υμενίων υψηλής μαγνητικής ανισοτροπίας κραμάτων λευκόχρυσου-μεταβατικού μετάλλου (Μ.Μ.=κοβάλτιο, σίδηρος και χρώμιο). Η μελέτη επικεντρώθηκε σε τέσσερα κυρίως θέματα.

Στο πρώτο μέρος μελετήθηκε η επίδραση της στρωματικότητας και του πάχους σε υμένια $L1_2$-$CrPt_3$ και $L1_0$-CoPt. Παρατηρήθηκε ότι στις στρωματικές δομές επιτυγχάνονται υψηλότερες τιμές συνεκτικού πεδίου και αποκατάσταση της χημικής τάξης.

Στο δεύτερο μέρος μελετήθηκε η επίδραση του μαγνητικού πεδίου κατά την ανόπτηση στον προσανατολισμό πολυστρωματικών υμενίων $L1_0$-Co/Pt. Τα υμένια που έχουν υποστεί θερμική επεξεργασία παρουσία μαγνητικού πεδίου αναπτύσσουν (001) προσανατολισμό και συνεπώς κάθετη μαγνητική ανισοτροπία. Υπολογίστηκε και παρατηρήθηκε, επίσης, συσχέτιση διαξονικών εφελκυστικών παραμορφώσεων, εξαιτίας του μαγνητικού πεδίου, σε μακροσκοπικό επίπεδο ευνοώντας τον (001) προσανατολισμό.

Το τρίτο μέρος περιλαμβάνει τη χρήση μονοστρώματος νανοσφαιρών πυκνής εξαγωνικής διάταξης δύο διαφορετικών μεγεθών (970nm και 173nm) ως μάσκα για την εναπόθεση υμενίων FePt με νανοδομικά χαρακτηριστηκά (νησίδες). Μετά από ανόπτηση οι νησίδες κρυσταλλώνονται στην τετραγωνική $L1_0$ δομή και είναι μαγνητικά σκληρές. Οι νησίδες χαρακτηρίζονται από μη μηδενικές μεταξύ τους αλληλεπιδράσεις. Επίσης, πραγματοποιήθηκε και έγινε σύγκριση των παραπάνω αποτελεσμάτων με μικρομαγνητικούς υπολογισμούς. Οι μικρομαγνητικοί υπολογισμοί έδειξαν ότι οι νησίδες αποτελούνται από τοιχώματα πολλών περιοχών, εξαιτίας της παρουσίας μαλακών φάσεων ή νησίδων με διαφορετικό προσανατολισμό ανισοτροπίας.

Στο τελευταίο μέρος μελετήθηκε η αντιστροφή της μαγνήτισης πολυστρωματικών υμενίων βαθμιδωτής ανισοτροπίας, με καμπύλες ανάκρουσης πρώτης τάξης, που έχουν εναποτεθεί είτε σε υποστρώματα πυριτίου είτε σε μονόστρωμα νανοσφαιρών. Τα αποτελέσματα έδειξαν ότι τα πολυτρωματικά υμένια μπορούν να χρησιμοποιηθούν σαν

μοντέλο για τη δημιουργία βαθμιδωτής κάθετης ανισοτροπίας όσο η εγκάρσια διάδοση των τοιχωμάτων περιορίζεται από τα νανοδομικά χαρακτηριστικά.

List of Figures

List of Tables

Introduction

Magnetism is phenomenon that has fascinated, in the past, many researchers. Today, it still remains an interesting and exciting area for scientific research. A wide range of state-of-the art applications in science, technology and medicine are based on magnetic effects. One of these applications, widely used in everyday modern life is magnetic recording.

Magnetic recording is the dominant storage technology and has played a leading part in the development of audio, video and computer applications. The first hard disk drive (RAMAC) manufactured by IBM in 1956 and brought about a revolution in magnetic storage. The areal density of hard disk drives (HDD) has been increasing exponentially for over 60 years. The average areal density exceeds 30%, reaching the astonishing rate of 100% in 1990s (figure 1). Hard disk drive surpass other competing technologies, such as Josephson memory, semiconductor memory, magneto-optical (MO) recording and solid state devices (SSD), as it combines high areal density with fast access times.

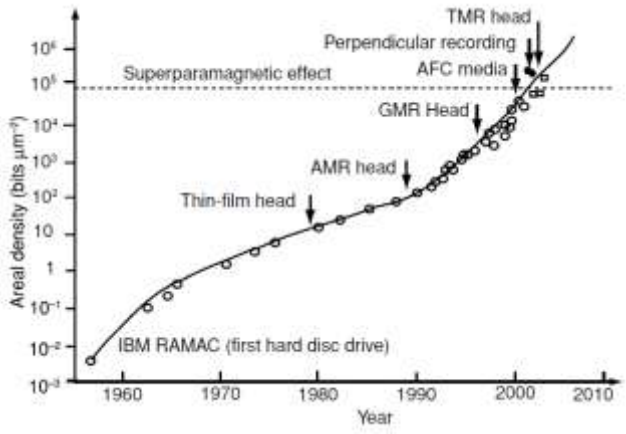

Figure 1: Time evolution of magnetic recording areal density [1].

Today, the goal is to produce hard disks with areal densities in the range 1-5Tbit/in^2. To achieve this goal we have to overcome the technological barriers limiting

areal density. In the following pages some of the candidate magnetic materials and alternative magnetic technologies are analyzed. It will become clear that this technical goal is closely connected with several open problems related to materials optimization, phase and microstructure control, and nanotechnology processing. The sensitive dependence of magnetic properties on microstructural characteristics imposes stringent limitations on the preparation of these magnetic materials. Thus, these technical requirements instigate the study of more basic questions regarding for instance the magnetization reversal mechanisms, and the chemical ordering and growth kinetics of the crystallographic phases involved. Furthermore, as conflicting design requirements create additional challenges. Different approaches which have been proposed and tested in recent years, each one targeting different aspects of recording media design have inspired the studies included in this thesis.

CHAPTER 1

1. Magnetic Recording

The growing demand for ever increasing storage capacities in computers and consumer electronics is the market pull behind magnetic recording media research and development. Recently, it has been calculated that the upper limit for current conventional perpendicular media is 500Gbit/in^2 [2]. Further progress will require major breakthroughs and alternative technologies in order to manufacture ultra-high density recording hard disks with capacities exceeding 1Tbit/in^2 [3,4]. Media design requirements include high signal-to-noise ratio (SNR), high thermal stability and fast writability that pushes the write head field requirements beyond those available. These three requirements constitute the so-called "magnetic recording trilemma [5], as they conflict with each other (figure 1.1).

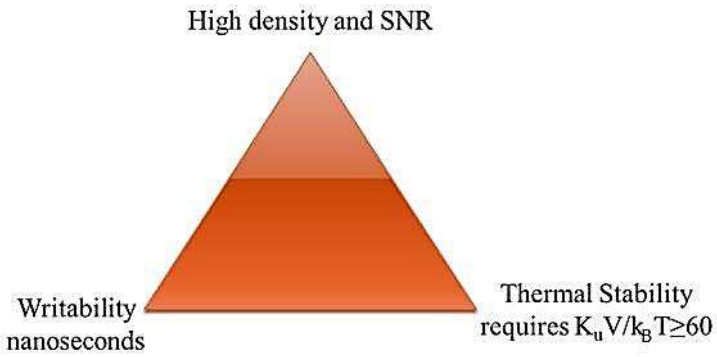

Figure 1.1: The magnetic recording trilemma.

An increase of areal density is associated with the simultaneous reduction of the bit length (B) and the track width (W). The signal-to-noise ratio (SNR) is proportional to the number of independent grains contained in a single bit and is estimated from the equation:

$$SNR = 10\log_{10}\frac{BxW}{D^2} \qquad (1.1)$$

,where D is the grain diameter [6]. The above equation (1.1) indicates that the SNR increases by increasing of number of grains and the reduction of grain size. The reduction of grain size leads to thermal instability problems and the appearance of the phenomenon of superparamagnetism [7]. This arises when the reduced anisotropy energy K_uV of each grain is insufficient to keep the magnetization direction stable for times longer than the timescale of our experiment. In the case of magnetic recording, the magnetization thermal stability criterion of for a period of 10 years is:

$$\frac{K_u V}{k_B T} \geq 60 \tag{1.2}$$

,where K_u is the magnetocrystalline anisotropy, V is the grain volume, k_B is the Boltzmann constant and T is the temperature in Kelvin [8,9]. Thus, for thermal stability we need materials with high magnetocrystalline anisotropy, but increased anisotropy means higher fields are required to write a bit, exceeding the current head writability limit (FeCo with $\mu_o M_s$=2.4T) [5,10]. The conflict is further complicated by the short (nanosecond) access time as opposed to the long (decade) storage time required.

To resolve the magnetic recording trilemma and achieve high areal densities we need to combine high anisotropy materials, such as Co/Pt multilayers, FePt, CoPt, and $CrPt_3$ with perpendicular media, graded exchange-spring media, patterned and self-assembled media.

1.1 Perpendicular Media

Perpendicular magnetic recording (PMR) was introduced by Iwasaki and Takemura in 1975 [11]. In perpendicular media the direction of the magnetic easy axis is perpendicular to the film surface. These media offer better thermal stability than the longitudinal media, because the PMR demagnetizing fields are smaller [12,13]. In addition, perpendicular media require single pole heads and a soft magnetic underlayer with in-plane anisotropy under the perpendicular recording layer, so as to close the magnetic flux loop (figure 1.2(a)). With the combination of single pole heads and soft underlayers (SUL) higher writing fields can be achieved; as a consequence materials with high K_u can be used as recording layers [14]. Even though it was calculated that the upper limit for current

conventional perpendicular media would be 500Gbit/in^2 [2], in August of 2010 hard disk drives of 667Gbit/in^2 were commercially available.

The most commonly used perpendicular media materials are the CoCrX (X=Pt, Ta) alloys. The CoCrPt alloy is usually combined with an oxide of Si or Ti (figure 1.2(b)). The presence of oxides at grain boundaries helps to control the grain size, magnetically decouple the grains, and reduce the signal noise [15,16]. The main drawback of using CoCr-oxide as a recording layer is the reduced anisotropy in comparison with similar longitudinal media [17]. Other materials that can be used for perpendicular recording are Co/Pt and Co/Pd multilayers [18], the chemically ordered $CrPt_3$ alloy [19] and the ordered CoPt, FePt alloys crystallized in the $L1_0$ structure with the c-axis oriented perpendicular to the surface [20].

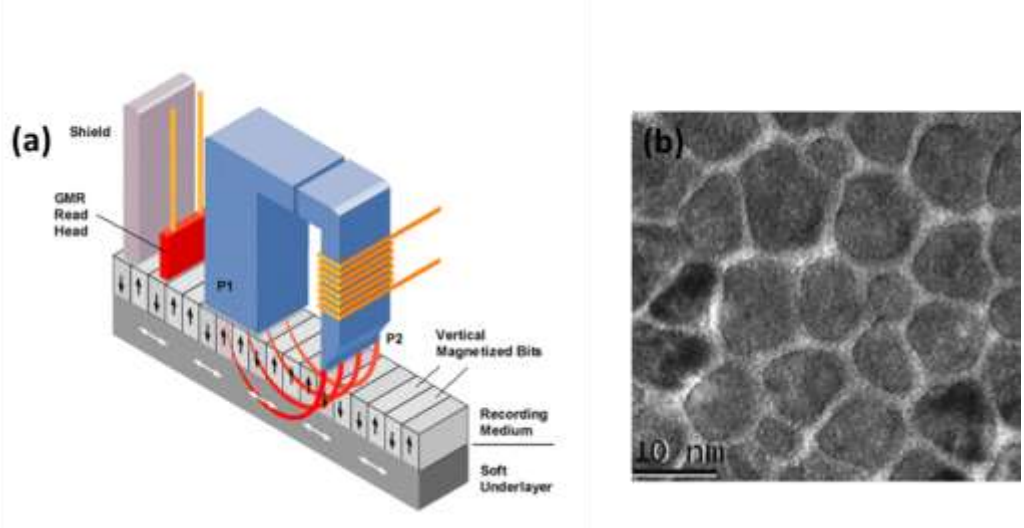

Figure 1.2: (a) The single pole head and SUL in perpendicular magnetic recording, (b) Transmission electron microscope (TEM) image of granular CoCrPt:SiO_2 perpendicular media [21].

1.2 Graded Exchange Spring Media

Recently, graded exchange spring media [22,23] have been proposed to achieve storage density up to 1Tb/in^2, as they can reduce the switching fields while keeping the thermal stability constant. When two magnetic phases of substantially different anisotropy are combined into coupled layered superstructures the magnetization reversal exhibits an

interesting behavior which has been termed “exchange spring” [24]. Counter-intuitively the coupling between the two phases was found to be more effective in the case of an interface with a graded anisotropy profile rather than for a sharp one [25]. More recently hard/soft bilayers with graded interfaces have been proposed as a means to deal with the conflicting constrains of thermal stability (figure 1.3) and writability in current ultra-high density magnetic recording media [26,27,28,29,30]. The conflict arises from the fact that long term thermal stability at high densities requires high anisotropy, which in turn increases the write head field requirements beyond those available. However, the reversal modes induced by the external write field are significantly different from the thermally activated switching processes. Thus, the bilayers can be optimized in order to achieve a high thermal stability without an increase of the coercive field.

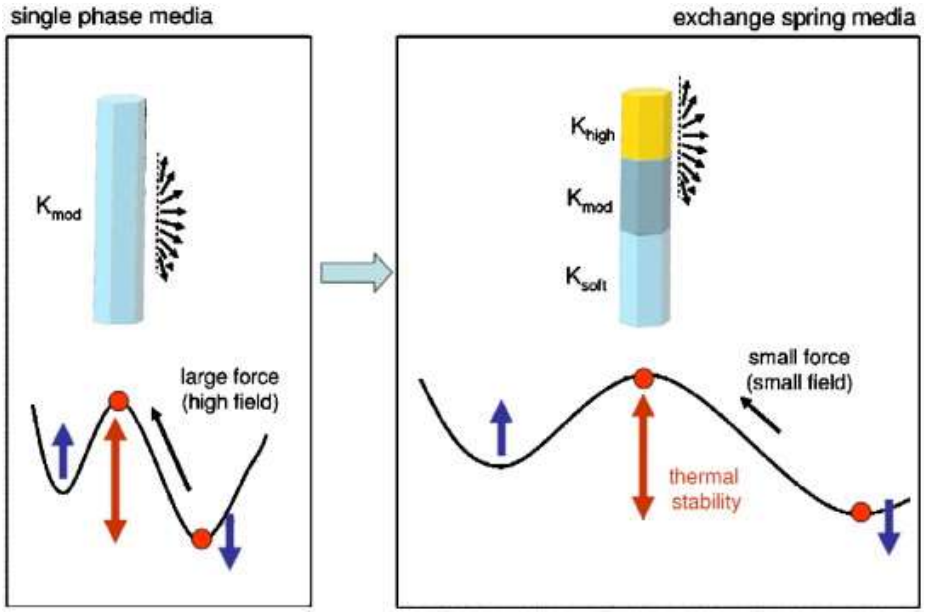

Figure 1.3: Thermal stability difference between single phase and graded exchange spring media [30].

There are several ways to create graded anisotropy media. One is to simply combine high anisotropy and low anisotropy materials, like FePt($L1_0$)/CoPt(A1) multilayers [31], FePtCu/(Co/Pt) [32] and $L1_0$-FePt/Fe [33]. Another approach is by varying the pressure during sputtering of Co/Pd multilayers [34] or adding a ternary element, like Cu in FePt films [35,36].

1.3 Patterned and Self-assembled Media

The spectacular growth of magnetic recording media applications in recent decades has intensified efforts for the preparation and characterization of nanostructures consisting of uniform, single domain, non-interacting magnetic entities with high anisotropy [37]. The most typical example of such structures are patterned media [38,39,40]. Patterned media can be produced with either top-down or bottom-up techniques (figure 1.4). Top-down techniques include e-beam and x-ray lithography, but due to their high cost and the desire for serial processing, the bottom-up approach is preferred.

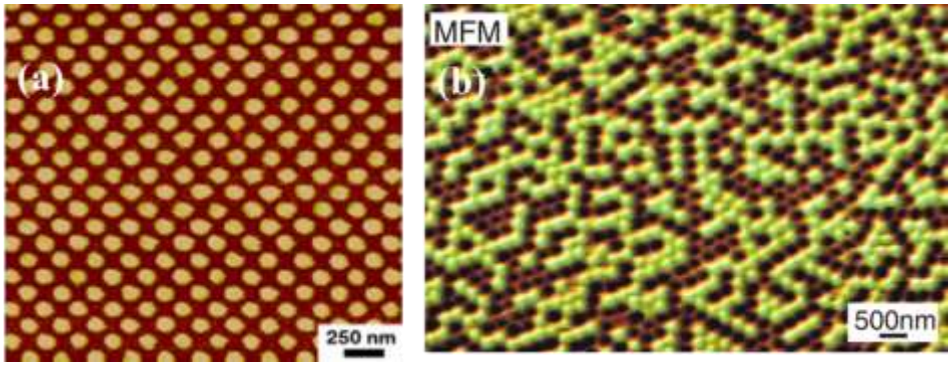

Figure 1.4: (a) Atomic force microscope (AFM) image of top-down fabricated 60nm $L1_0$-FePt dots [41] and (b) Magnetic force microscope (MFM) image of bottom-up fabricated single domain particles of Co/Pd multilayers deposited on nanospheres [42].

A promising alternative method is to use materials by which model nanostructures are obtained using bottom-up approaches that are capable of producing nanostructures over large surface areas in a facile low-cost way. Examples are anodized alumina [43,44] and single layer monodisperse nanospheres, which tend to form hexagonal close packed patterns [45,46,47,48,49]. The latter can be used either as a template for the deposition of magnetic layers, producing so called ‘nanocaps’ [42,50,51] or as a mask for the formation of triangular-like islands [52,53]. Candidate materials for patterned media are Co/Pt or Co/Pd multilayers with perpendicular anisotropy and high anisotropy materials such as fct CoPt and FePt alloys.

CHAPTER 2

2. Materials Challenges for Tb/in^2 Magnetic Recording

In the last twenty years 3d transition metal alloys have been investigated as prospective materials for magneto-optical and magnetic recording. Some of these materials are the chemically ordered FePt, CoPt, $CrPt_3$ alloys and the Co/Pt superlattices. These materials exhibit high magnetization, high anisotropy, high coercivity and high squareness. The following pages will give a comprehensive review of their properties.

2.1 $L1_0$ Structure of FePt Alloy

The $L1_0$ FePt magnet was discovered by Graf and Kussmann [54] and exhibits high coercivity, arising from the large magnetocrystalline anisotropy. The $L1_0$ FePt is a ferromagnetic material with Curie temperature of T_c=750K, spontaneous magnetization at room temperature J_s=1.43T and first magnetic anisotropy constant K_1=6.6MJ/m^3 [1,55,56].

At room temperature the as-deposited FePt film crystallizes in an fcc A1 structure and is magnetically soft. In the A1 phase the FePt alloy is chemically disordered and the Fe and Pt atoms randomly occupy the unit cell (figure 2.1(a)). The lattice parameters are a=b=c=3.744Å. The $L1_0$ is thermodynamically the low temperature phase, but due to kinetic limitations, it is obtained by annealing the disordered A1 (fcc) phase. In the chemically ordered equiatomic FePt phase, Fe and Pt occupy alternating atomic planes along the crystallographic c-axis of the tetragonal $L1_0$ unit cell (figure 2.1(b)), which is the magnetic easy axis. During the A1 to $L1_0$ transformation a distortion of the cubic unit cell takes place; the a lattice parameter expands approximately 2%, while the c lattice parameter shrinks by approximately 2.5% [57]. The lattice parameters in $L1_0$ structure become a=b=3.838Å and c=3.715Å.

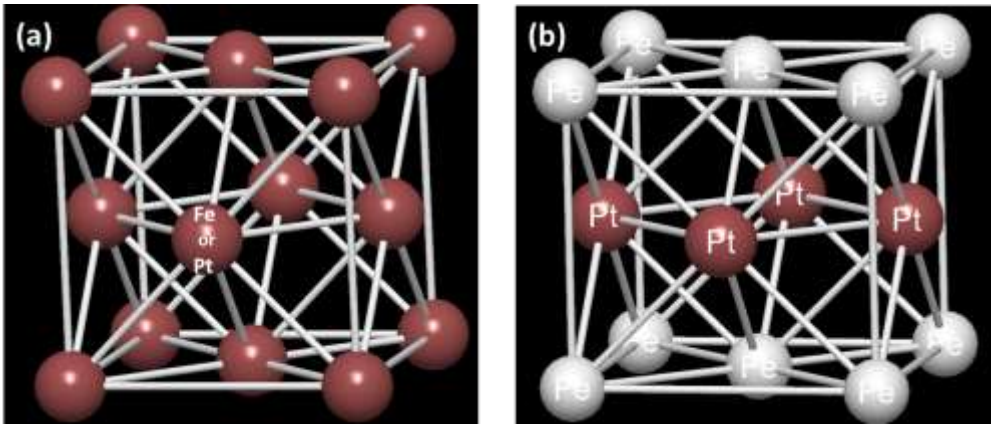

Figure 2.1: Schematic illustration of the unit cell of (a) A1 and (b) $L1_0$ FePt phase.

The $L1_0$ phase can be produced in thin film form by sputtering [58] and molecular beam epitaxy [59] with subsequent annealing at elevated temperatures of the as-deposited A1 films. Direct synthesis of $L1_0$ FePt films can be accomplished by the use of heaters during the deposition of films [60]. Many attempts have been made to process $L1_0$ FePt at lower temperatures using e.g. monolayer deposition using molecular beam epitaxy [61], annealing of Fe/Pt multilayers [62] and addition of a ternary element (Cu) to the FePt films [63]. Apart from the film form, the $L1_0$ FePt phase can be fabricated by chemical synthesis of nanoparticles [64,65] and in bulk form [66,67].

2.2 $L1_0$ Structure of CoPt Alloy

The $L1_0$ CoPt magnet was discovered by Jellinghaus [68] and exhibits high magnetocrystalline anisotropy, which is intrinsic to the tetragonal symmetry of the crystal structure. The $L1_0$ CoPt alloy is a ferromagnetic material with Curie temperature of T=840K, spontaneous magnetization at room temperature J_s=0.99T, saturation magnetization M_s=0.81MA/m and first order magnetic anisotropy constant K_1=4.9MJ/m^3 [1,69].

The easiest method to produce the $L1_0$ CoPt structure is through heat treatment of the A1 CoPt structure at high temperatures. The $L1_0$ CoPt structure is formed, when the cubic symmetry of the A1 structure is broken by the chemical ordering of Co and Pt on alternate planes along the c-axis. The lattice parameters are a=b=c=3.835Å and a=b=3.803Å, c=3.703Å for the A1 and $L1_0$ phase, respectively. X-ray diffraction (XRD) is

a powerful technique to identify the transition from the chemically disordered A1 phase to the chemically ordered $L1_0$ phase. In the A1 structure only fundamental reflections, such as (111), (200) and (220) peaks (figure 2.2(a)) are present. In the $L1_0$ structure a splitting of the fundamental reflections is observed with the appearance of additional superstructure reflections, such as the (001) and (110) peaks (figure 2.2(b)).

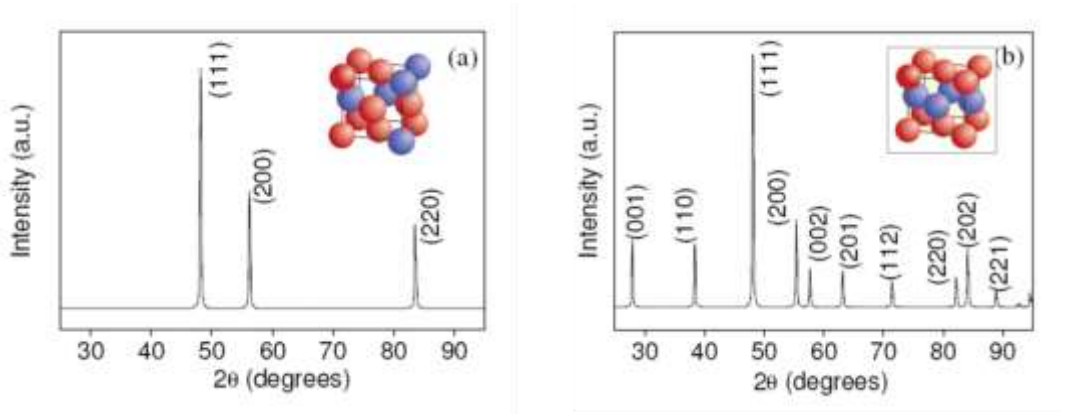

Figure 2.2: X-ray diffraction patterns of (a) A1 and (b) $L1_0$ CoPt structures.

2.3 Magnetocrystalline Anisotropy in $L1_0$ Structure

Magnetic anisotropy is the free energy dependence of the direction of the magnetization relative to the structural axes of the material. There are five different sources of magnetic anisotropy: magnetocrystalline anisotropy, shape anisotropy, magnetoelastic anisotropy, induced anisotropy and surface/interface anisotropy [1,6,70]. Magnetocrystalline anisotropy is the magnetic anisotropy that leads to a preferential alignment along some specific crystallographic axis and stems from relativistic spin-orbit coupling and electrostatic crystal-field interaction [6,71].

The strong magnetocrystalline anisotropy in FePt and CoPt $L1_0$ magnets originates from the large spin-orbit coupling in Pt and the 3d(Fe or Co)-5d(Pt) hybridization [56,72]. Magnetocrystalline anisotropy in $L1_0$ magnets is affected by the tetragonal lattice distortion and the chemical ordering during the transformation from the cubic A1 to the tetragonal $L1_0$ structure. The origin of the large magnetocrystalline anisotropy in the $L1_0$ phase is under investigation, as the lattice distortion and chemical ordering are correlated. The majority of studies made until now indicate that the magnetocrystalline anisotropy

energy (MAE) is sensitive to both factors, but lattice distortion has a more minor effect on MAE than that of chemical ordering [72,73,74,75].

2.4 $L1_2$ Structure of $CrPt_3$ Alloy

The chemically ordered $CrPt_3$ alloy crystallizes in the Cu_3Au ($L1_2$) crystal structure. In the $L1_2$ phase, the Cr and Pt atoms are located at each of the corners and the face centers of the cubic unit cell, respectively (figure 2.3). Measurements with polarized neutron diffraction revealed that the chemically ordered bulk $CrPt_3$ alloy is ferrimagnetic with magnetic moments of μ_{Cr}=3.37μB and μ_{Pt}=-0.27μB [76]. In the $L1_2$ phase the $CrPt_3$ film shows a Curie temperature of Tc=500K [77], saturation magnetization of M_s=0.2MA/m and an anisotropy constant of K_u=0.8MJ/m^3 [19].

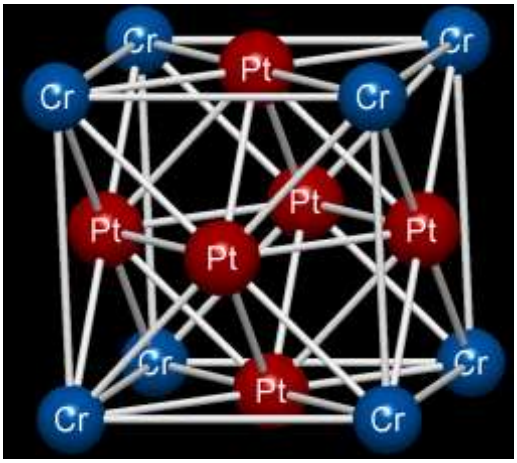

Figure 2.3: Schematic illustration of the $L1_2$ $CrPt_3$ unit cell.

The chemically ordered $CrPt_3$ exhibits strong perpendicular magnetic anisotropy (PMA) [19,78] and is ideal for perpendicular magnetic recording, since the easy axis is along the [111] direction, which is the usual texture of sputtered films. The magnetocrystalline anisotropy in $L1_2$ $CrPt_3$ alloy is the largest that has been observed in cubic structures and at the same is unexpected, by virtue of the cubic symmetry. The magnetocrystalline anisotropy arises from the ferrimagnetic order between the nearest Cr-Pt neighbors, due to the spin-orbit coupling of the Pt atoms through the 3d(Cr)-5d(Pt)

hybridization [79]. Finally, the $L1_2$ $CrPt_3$ alloy is a promising material for magneto-optical recording, by virtue of its large magneto-optical Kerr effect [80,81].

2.5 Perpendicular Anisotropy in Co/Pt Superlattices

In the mid-1980s, the phenomenon of perpendicular anisotropy was observed in ultrathin superlattices consisting of alternating layers of ferromagnetic and non-magnetic metals [82]. Although, the majority of multilayers show in-plane magnetic anisotropy, the Co/Pt and Co/Pd superlattices exhibit strong perpendicular anisotropy and tunable magnetic properties. Perpendicular magnetic anisotropy in the above superlattices originates in the interfacial anisotropy between the magnetic and non-magnetic layers, when the thickness of cobalt is very small ($t_{Co}\approx 4$Å) [83,84]. For larger Co thicknesses, the multilayers are easily magnetized in-plane, as the anisotropy is too small to overcome the demagnetizing fields of the thin film. The effective anisotropy K_{eff} is given by the equation:

$$K_{eff} = K_v + \frac{2}{t} K_s \tag{2.1}$$

,where t is the thickness of the magnetic layer, K_v is the volume anisotropy constant and K_s is the surface anisotropy constant [85]. C.J. Lin and his coworkers achieved K_{eff} equal to 5.5MJ/m^3 in Co/Pt multilayers [86].

On account of their large perpendicular anisotropy the Co/Pt multilayers are candidate materials for high density perpendicular and magneto-optical recording. Therefore, within the past thirty years, there have been studies on the perpendicular anisotropy dependence on Co layer thickness [82,86,87,88], Pt layer thickness [86,89], crystallographic orientation [86,90], and roughness and interdiffusion [80]. Some of the advantages of using $[Co/Pt]_N$ multilayers are the control of perpendicular anisotropy and coercivity, achieved by adjusting the Co and Pt thicknesses and the number of bilayers. Another advantage is the Pt resistance to corrosion and oxidation, avoiding the need for a protective top layer. Furthermore, there is no need for annealing at elevated temperatures, which can lead to oxidation and further film treatment of the, to achieve the desired properties.

Co/Pt multilayers have been combined with alternative magnetic recording processes, leading to new classes of magnetic materials. For example, they have been deposited onto nanoparticles arrays [42,91] and anodic aluminum oxide membranes [92,93], so as to create perpendicular Bit Patterned Media (BPM) and percolated media, respectively. Another approach is to create Co/Pt multilayers with anisotropy gradients to form exchange spring and graded anisotropy media [34,94]. Finally, an extensive study of the magnetization reversal process has been accomplished in the systems described before [92,95].

CHAPTER 3

3. Magnetization Reversal and FORC

Magnetization reversal is one of the most important processes in magnetic material design; its study gives us information on the way that the magnetization changes from one stable direction into another and therefore the appropriateness of a magnetic material for specific applications. Magnetization reversal is determined by several competing energy contributions which characterize magnetic materials, such as exchange energy, magnetocrystalline anisotropy energy and Zeeman energy. In this chapter the magnetization switching mechanisms shall be analyzed with respect to size effects and domain wall propagation in magnetic systems with hard-soft phases. Furthermore, the modeling of hysteresis with First Order Reversal Curves (FORC) will be discussed.

3.1 Domains and Magnetization Reversal Processes

Magnetic materials are composed of magnetic regions called magnetic domains or Weiss domains [96], in which magnetic moments are fully oriented, so as to minimize the exchange energy. At the same time the direction of magnetization differs from one domain to another, in order to minimize the total magnetostatic energy. The interfaces between magnetic domains are called domain walls. The simplest types of domain walls are the Bloch [97] and Néel [98]. In Bloch walls, the magnetization rotates in the plane of the wall (figure 3.1(a)). In sufficiently thin films, on the other hand, Néel walls, in which the magnetization rotates within the plane of film (figure 3.1(b)), may be come favorable so as to minimize magnetostatic energy. Thus, in the case of thin films, the type of domain wall that will dominate depends on film thickness. For film thickness down to a critical value Bloch walls are favored, but below this critical thickness a Néel wall is formed. For thicknesses close to Bloch-Néel transition the cross tie wall is formed, where segments of

Néel walls with opposite polarity are separated by narrow Bloch regions, with a view to reduce magnetostatic energy [1,6].

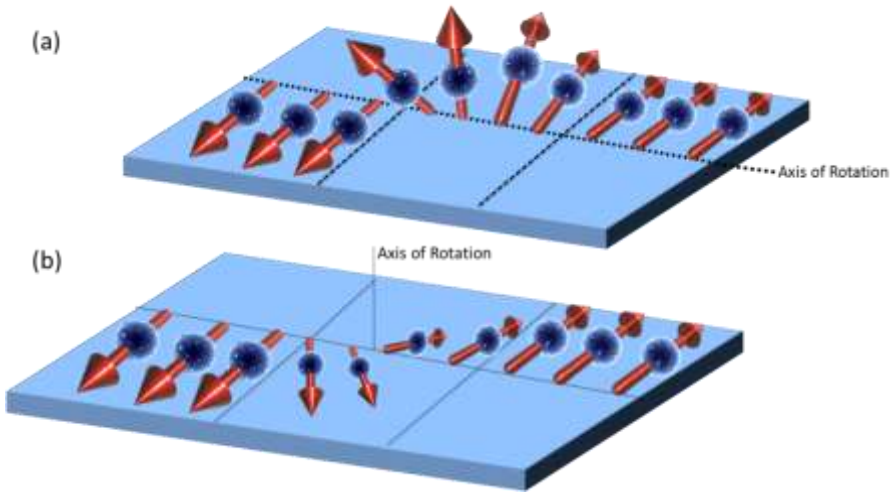

Figure 3.1: (a) A Bloch wall and (b) a Néel wall.

Magnetization reversal processes can be classified in two categories: collective and non-collective. The collective switching includes coherent and incoherent reversal processes, where the magnetization rotates simultaneously. The main difference between coherent and incoherent reversal is that in the former, the magnetization remains uniform everywhere, whereas the latter involves an intermediate state, which is not uniformly magnetized. Incoherent reversal processes introduce more complex modes, such as curling or vortex and buckling. Non-collective switching includes the nucleation of reversed domains and the propagation of Bloch walls. The way that magnetization reversal will take place depends on material's lateral dimensions, shape, microstructure and magnetic properties.

For a perfect crystal, the Bloch wall energy is independent of its position and the wall can be moved freely, if there is no change in its total area, as the energy per unit area remains constant. But real crystals have imperfections, such as defects or dislocations, which have an associated magnetostatic energy. Imperfections differentiate the exchange (A) and anisotropy (K) parameters and as a result the domain wall energy $\gamma = 4\sqrt{AK}$ becomes position dependent in inhomogeneous regions. This mechanism can give rise to the effect of domain wall pinning, where domain walls become trapped in regions where their energy is minimized [1,6,71]. Among imperfections, planar defects have a stronger

pinning effect, since the entire domain wall's energy changes when it encompasses the defect [1,6]. Pinning is more effective when the dimensions of inhomogeneity are comparable with the domain wall width $\delta = \sqrt{\frac{A}{K}}$. The pinning strength can be described by the value of pinning field H_P, which is the field required for a domain wall to propagate through the energy barrier of the inhomogeneity. When the domain wall width is much shorter than that of the imperfection, the pinning field H_P is given by a simple expression:

$$H_P = \frac{1}{2\mu_0 M_S}\frac{d\gamma}{dx} \tag{3.1}$$

Equation (3.1) reveals that the field necessary to depin a domain wall from a planar defect is proportional to the maximal gradient $\left[\frac{\partial\gamma}{\partial x}\right]_{max}$ created along the imperfection (figure 3.2).

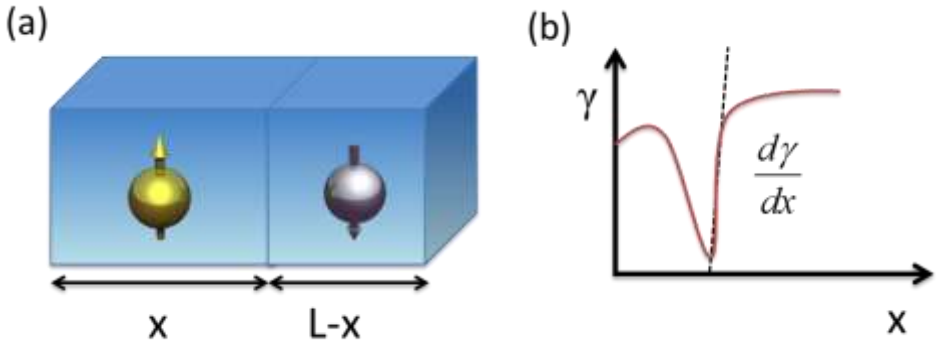

Figure 3.2: (a) Planar wall separating two domains with opposite magnetization, propagating along direction x, (b) domain wall energy as a function of wall position x; the dashed line shows where dγ/dx and pinning strength are largest.

The coercivity as a function of particle size is illustrated in figure 3.3. Magnetic particles of nanometer size are single-domain, because the formation of domain walls becomes energetically unfavorable [99] as the surface to area ratio increases. In the single-domain state the reversal is accomplished with either coherent or incoherent rotation [100] depending on the particle size. Coherent rotation dominates at lower sizes but as the volume of the particles decreases the energy barrier for magnetic reversal (which is

proportional to the particle volume times the anisotropy constant) becomes gradually comparable to the thermal energy and magnetic state of the particles is affected by thermal fluctuations eventually leading to zero coercivity below the so-called superparamagnetic limit [7]. Larger particles are multi-domain and typically show lower coercivity, since magnetization reversal takes place through localized modes (nucleation/propagation). In the multidomain state inhomogeneities may increase the coercivity by providing pinning sites, while in the single domain regime in principle decrease the coercivity as they may act as nucleation centers.

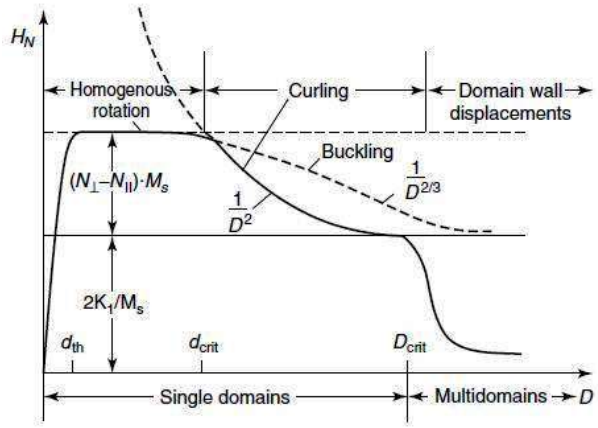

Figure 3.3: Coercivity dependence of particle size [101].

3.2 The Stoner-Wohlfarth Model

The Stoner-Wohlfarth model [102] describes the magnetization reversal with coherent rotation in single domain particles. The aim of Stoner-Wohlfarth model is to calculate the equilibrium directions of magnetization for a given anisotropy and applied field. In this model the exchange energy is zero, since magnetization reversal is taking place with coherent rotation, and the energy of the particle is essentially equal to anisotropy energy. The total energy density for a single domain ellipsoid particle with uniaxial anisotropy is the sum of effective anisotropy and Zeeman energy:

$$E_{tot}(\phi, \mathrm{H}) = \mathrm{K}_u \sin^2 \phi - \mu_o \mathrm{H} \mathrm{M}_S \cos(\theta - \phi) \tag{3.2}$$

,where φ is the angle between magnetization and easy axis, and θ is the angle between the applied field and easy axis [1,6,28,70,103]. The total energy minima can be found using the conditions $dE/d\varphi=0$ and $d^2E/d\varphi^2 \geq 0$. This yields two energy minima, one local and one absolute, separated by an energy barrier. The origin of the hysteresis loop is the irreversible jump of magnetization from the local minimum to the absolute minimum (figure 3.4).

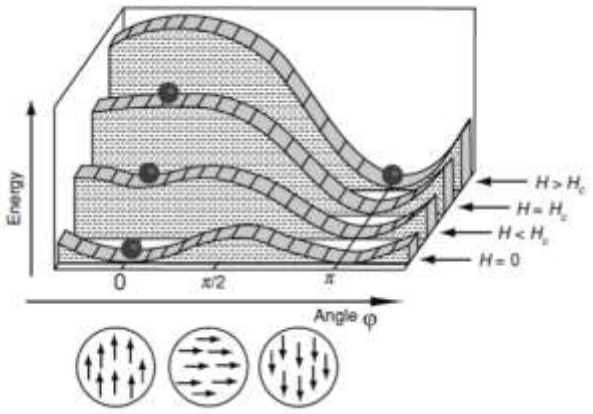

Figure 3.4: Energy landscape and coercivity for Stoner-Wohlfarth model [1].

The shape of the hysteresis loop has a strong dependence on the angle θ (figure 3.5(a)). The most interesting limits are the $\theta=0^o$ (easy axis) and $\theta=90^o$ (hard axis). In the Stoner-Wohlfarth model the maximum coercivity is achieved for $\theta=0^o$, where the hysteresis loop is square, with the coercivity equal to the anisotropy field $H_K=2K/\mu_o M_S$. In contrast, there is no hysteresis when the field is applied along the hard axis ($\theta=90^o$). It is worth mentioning that measurements along the hard axis can be used to calculate the strength of the anisotropy in magnetic materials.

The angular dependence of the nucleation and coercive fields for different values of θ is shown in figure 3.5(b). There are two curves; coercivity (straight curve) and nucleation field (dashed curve). The coercivity is defined as the point of zero magnetization and nucleation field denotes the point of irreversible jump from the upper to the lower branch of the hysteresis loop. The angular dependence of nucleation field and coercivity coincide below 45 degrees. But, above 45 degrees the coercivity is smaller than the nucleation field.

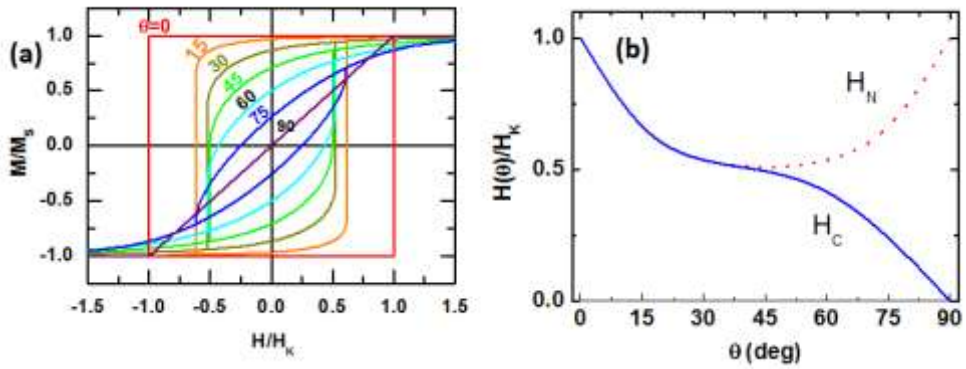

Figure 3.5: (a) Hysteresis loops of Stoner-Wohlfarth particle with uniaxial anisotropy for different angles θ, (b) angular dependence of coercive and nucleation field as a function of the angle θ.

In real particle systems there is a deviation from Stoner-Wohlfarth model, since grain imperfections and crystal defects act as nucleation centers for reverse domains. As a result particles follow Stoner-Wohlfarth-like behavior. Even though some systems show Stoner-Wohlfarth characteristics, for multilayers deposited onto nanospheres the magnetization reversal process is affected by the curvature of the particles and does not follow Stoner-Wohlfarth behavior, but collective processes [104].

3.3 Switching in Magnetic Composites by Domain Wall Propagation

As mentioned in paragraph 1.2 exchange-spring and graded media are composite magnetic materials that consist of soft and hard phases, where the anisotropy at the hard/soft interface changes sharply (exchange spring) or gradually (graded media), respectively. Magnetically soft and hard phases are exchange coupled and the switching process, under the action of an external field, proceeds through two steps (figure 3.5). Initially, with increasing external magnetic field a reverse domain is nucleated in soft phase, forming a domain wall that is pinned at the soft/hard interface. With increasing field, the domain wall will depin and propagate irreversibly through interface into the hard phase [26,105]. The most important critical field values which characterize the switching process are nucleation field (H_{n1}) in the soft phase and the domain wall propagation field (H_{dw} or H_p) in the transition from soft to hard phase. The switching field H_{sw} is given by max(H_{n1} and H_{dw}) [23,106].

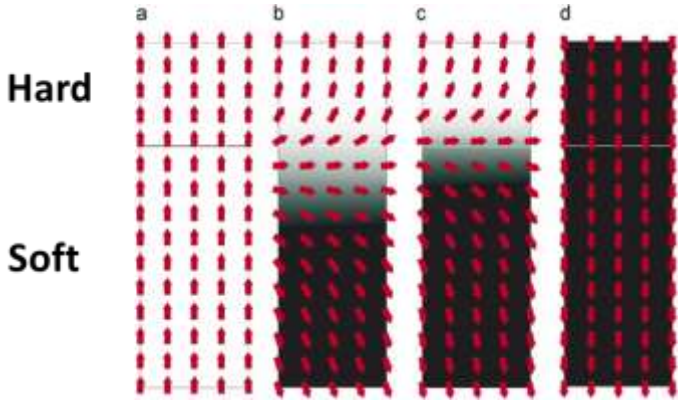

Figure 3.6: Domain wall propagation in exchange coupled composite particle: (a) hard and soft phases before nucleation, (b), (c) nucleation of reverse domain wall in soft phase and pinning in interface, and (d) propagation of domain wall in hard phase [107].

Mukherjee and Berger [106] have developed a simple approach that captures the essential physics of the interfacial domain wall propagation based on the approximation that the total exchange energy of a wall is inversely proportional to its thickness, while the anisotropy contribution is proportional to the thickness. Their method can be described briefly as follows: There are two wall solutions, one in which the wall lies mostly in the soft phase and the other in the hard phase, which correspond to different energies $\sqrt{A_i K_{u,i}}$, implying an energy barrier for the propagation of the domain wall through the interface. The total energy of the soft phase, with a domain wall pinned at the interface and contained mainly in the soft phase side, is the sum of Zeeman, anisotropy and exchange energies:

$$E_1 = (a\varepsilon_1 - l_1)m_1 H_{ext} + 2\varepsilon_1 \mathrm{K}_{u1}/\pi + 2\pi \mathrm{A}/\varepsilon_1 \qquad (3.3)$$

,where α is a constant that can be obtained integrating the angular dependence of Zeeman energy density is within the wall limits, ε_1 is the wall width, l_1 is the soft phase thickness , m_1 is the magnetization, H_{ext} is the external field, K_{u1} is the soft phase anisotropy and A is the exchange stiffness. For $\partial \mathrm{E}_1/\partial\varepsilon_1 = 0$ the equilibrium wall energy and width become equal to $\mathrm{E}_{eq1} = 4\sqrt{AK_{u1'}}$ and $\varepsilon_{eq1} = \pi\sqrt{A/K_{u1'}}$, respectively, where $K_{u1'}$ is the soft phase effective anisotropy in the presence of an external magnetic field $(K_{u1'} = K_{u1} + \alpha\pi m_1 H_{ext}/2)$. With similar arguments for the solution with the domain wall on the hard phase side, the total energy of hard phase is:

$$E_2 = (l_2 - a\varepsilon_2)m_2 H_{ext} + 2\varepsilon_2 \mathrm{K}_{u2}/\pi + 2\pi \mathrm{A}/\varepsilon_2 \qquad (3.4)$$

, the equilibrium wall and width energies are $E_{eq2} = 4\sqrt{AK_{u2'}}$ and $\varepsilon_{eq2} = \pi\sqrt{A/K_{u2'}}$, respectively, where $K_{u2'} = K_{u2} - \alpha\pi m_2 H_{ext}/2$ [106].

The domain wall propagation energy, when the wall energies in the soft and hard phases are equal and the domain wall moves from soft to hard phase, is:

$$H_{dw} = 2(K_{u2} - K_{u1})/(am_1 + am_2)\pi \quad (3.5)$$

We can estimate the parameter $\alpha=1/\pi$ considering that in the case where soft phase is eliminated, (in the limits $K_{u1}\rightarrow 0$ and $m_1\rightarrow 0$) the switching field must give $H=2Ku_2/m_2$. Then equation 3.4 becomes:

$$H_{sw} = H_{dw} = 2(K_{u2} - K_{u1})/(m_1 + m_2) \quad (3.6)$$

This provides the main insight that the pinning field is proportional to the difference of the anisotropies of the two phases. More details on this derivation can be found in [106].

3.4 Characterization of Interactions with Delta-M Plots

A simple and easy approach to describe magnetic interactions in thin films or particles is that of delta-M plots [108]. The origin of delta-M plots is the Wohlfarth relation [109]:

$$2m_{IRM}(H) = m_{rs} - m_{DCD}(-H) \quad (3.7)$$

,where (IRM) and (DCD) are the isothermal remanent magnetization and dc demagnetization remanence (DCD), respectively, m_{IRM} is the IRM moment, m_{rs} is the saturation remanent magnetization and m_{DCD} is the DCD moment. Equation (3.6) describes the relationship between IRM and DCD for non-interacting single-domain particles. Henkel [110] first plotted this Wohlfarth relation and proposed that a deviation from equation (3.6) in real systems can be used as a measure of the interactions between particles. The delta-M plot is defined as the difference of two normalized remanence curves:

$$\delta M = 2M_{IRM} - 1 - M_{DCD} \quad (3.8)$$

Kelly [108] noticed that this is equivalent to the equation:

$$\delta M(H) = 2(P_{IRM} - P_{DCD}) \quad (3.9)$$

,where P_{IRM} and P_{DCD} are the fraction of particles switched at IRM and DCD, respectively.

These approaches can successfully describe, to a high degree, the magnetic interactions between particles, but they do not take into account, systematically, the effects of the magnetic state in interaction problem, especially at the point where m_{IRM} and m_{DCD} are coincided. The calculated delta-M values depend sensitively on the nature of the demagnetized state which is not uniquely defined. The thermally demagnetized state is by definition the most random one but in many cases one has to start from AC demagnetized samples. Stancu [111] introduced the generalized delta-M approach, which can be worked out without starting from a demagnetized state. The generalized delta-M approach is a more complex magnetic state than the delta-M, and including statistical and mean-field interactions (figure 3.6). The equation which describes the generalized delta-M approach is:

$$\delta M(H) = 2m_{IRM}(H) - \left[m_{rs} - m_{DCD}(-H)\right] \tag{3.10}$$

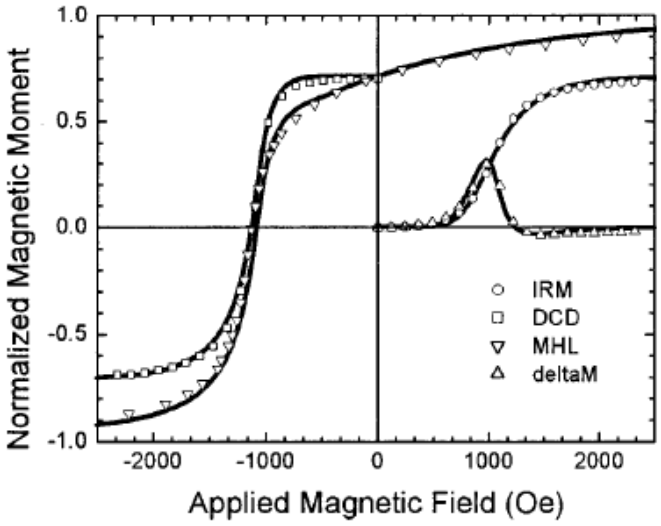

Figure 3.7: IRM (circle), DCD (square), major hysteresis loop (inverted triangle) curves and delta-M plot (triangle) of a barium ferrite powder dispersed film [111].

3.5 First Order Reversal Curves (FORC)

In 1935, Preisach developed a model to describe magnetic hysteresis [112]. The fundamental element of the Classical Preisach Model (CPM) is a rectangular hysteresis loop, which is called the hysteron [113]. Each hysteron has a unique normalized

magnetization, which switches from 1 to -1 under an applied field H=b (left coercivity) and from -1 to 1 under an applied field H=a (right coercivity). Hysterons can be described by two critical fields; one of them is the coercivity field, which is equal to $H_C = \frac{b-a}{2}$ and shows the hysteresis loop width, and the other is an interaction field, which is equal to $H_U = \frac{b+a}{2}$ and represents the hysteron shift along the field axis [114,115]. The above fields can be used to create the Preisach distribution ρ(a,b), which describes the macroscopic hysteresis properties of a particular sample. However, CPM, to some degree, does not have a physical basis, since in order to describe a particular particle system it needs a unique defined Preisach distribution to represent the system. The assumption that there exists a constant, well-defined local interaction at the site of each moment is physically invalid. Furthermore, the presumption that each single particle has a well-defined switching field is also under scrutiny, for the reason that any particle's switching field will be coupled via interactions to the neighboring particles [116].

An alternative approach for describing switching properties is the First Order Reversal Curves (FORC), which is a method for rapidly generating a particular class of Preisach diagram. FORC were first introduced by Mayergoyz [117,118] and developed by Pike [116]. FORC is a powerful method that can be used to evaluate separately the switching and interaction fields. The assemblage of FORC diagrams can be described by the following steps: (i) positive saturation, (ii) ramp down to a reversal field H_R and finally (iii) ramping up from H_R to positive saturation (figure 3.8(a)). The collection of magnetization data $m(H,H_R)$, during third step, is used to generate the FORC distribution:

$$\rho(H, H_R) = -\frac{1}{2}\frac{\partial^2 m(H, H_R)}{\partial H \partial H_R} \tag{3.11}$$

,where this is well defined for $H>H_R$ [114-116,118]. The FORC diagram is a contour plot of the above distribution. Each FORC distribution is plotted in a diagram of reversal field H_R as a function of H (figure 3.8(b)). The diagonal axes represent the rotated coordinates in terms of interaction (H_U) and coercive (H_C) fields, where $H_U = \frac{H+H_R}{2}$ and $H_C = \frac{H-H_R}{2}$, respectively [119,120].

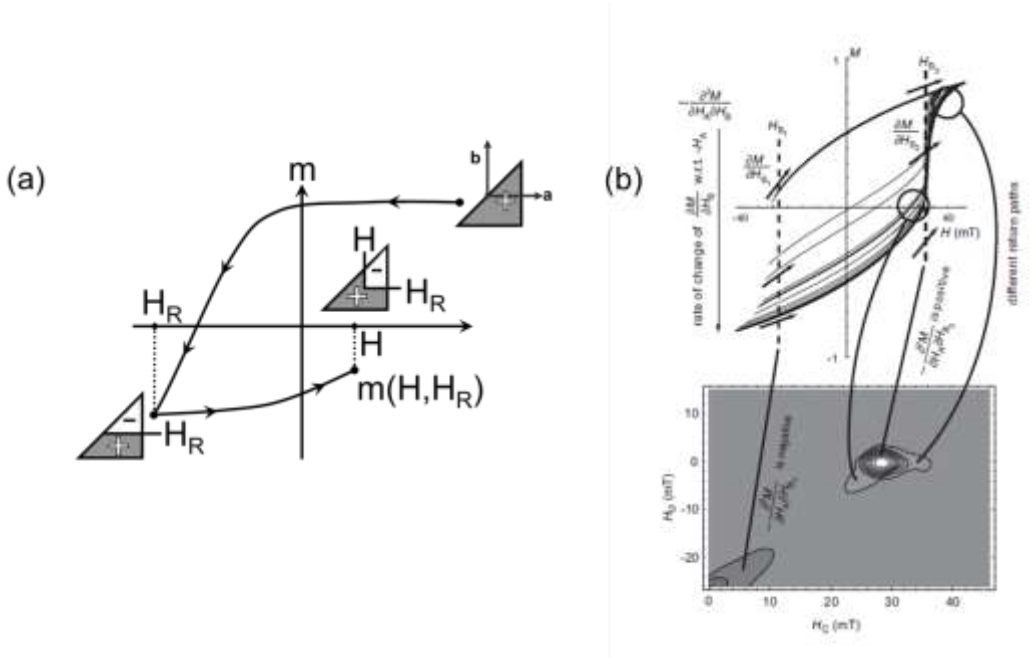

Figure 3.8: (a) Sketch of the measurement protocol by which FORC plots are obtained. The magnetic states are plotted for saturation, reversal field H_R and measurement field H. The magnetic state is defined by the positively and negatively magnetized domains (denoted as grey and white areas, respectively) in the Preisach triangle on Preisach plane (a,b) [115], (b) FORCs and FORC plot for a numerical model of non-interacting single-domain grains with randomly distributed uniaxial anisotropy [121].

A given CPM distribution implies the hysteresis properties under any possible field cycling, including the major loop and any minor loop. A FORC diagram can be considered as a means to extract the CPM distribution based on experimental data that consist of families of minor M versus H reversal curves after applying the formalism (3.11). However, the CPM is only a zero-order approximation that cannot capture the physics of reversal in real systems. Some improvements can be made through the introduction of distributions with variable interaction mean values (moving Preisach [122]) and widths (variable variance Preisach [123]) that are functions of the order parameter M. Thus, the FORC distribution is actually a static image of a dynamic process.

Characterization of magnetic materials with the FORC method is more powerful than simply using delta-M [108] and generalized delta-M procedures on major hysteresis loop data, [111]. Hence, FORC diagrams are widely used for the study of magnetization reversal in patterned media [124,125], graded media [35,126], hard/soft nanocomposite

magnets [127], nanopillars [119], multiferroics [128], geomagnetic [129] and biomagnetic [130] samples.

CHAPTER 4

4. Experimental Techniques

In this chapter, deposition and characterization techniques of films, multilayers and nanostructures shall be briefly described. Thin films, multilayers and metal nanostructures were prepared using a magnetron sputtering deposition system. Nanosphere lithography was used in order to shape metal nanostructures. Structural characterization was accomplished using X-Ray Diffraction (XRD), four-circle XRD, Grazing Incidence Diffraction (GID), X-Ray Reflectivity (XRR) and High Resolution Transmission Electron Microscopy (HRTEM). Morphological studies have been performed utilizing Transmission Electron Microscopy (TEM) and atomic force microscopy (AFM). Finally, the magnetic characterization was carried out using magnetic force microscopy (MFM), vibrating sample magnetometry (VSM) and alternative gradient field magnetometry (AGFM).

4.1 Sputtering

The science and technology of thin film fabrication deals with the mechanisms and processes during the deposition of atoms or molecules from the vapor phase onto the surface of a substrate (bulk material) and their characterization. Thin films have properties different from bulk materials, since they are essentially two dimensional (2D) structures, in which one dimension is nanometric and the other two macroscopic. Thin film thicknesses vary from a few angstroms (Å) to the sub-micrometer range. Growth conditions of thin films have a crucial impact on their structural, mechanical, electrical, magnetic and optical properties. Manipulating the growth conditions is thus necessary in order to achieve the rigorous control of the microstructure and surface morphology of thin films, in order to deposit films for specific technological applications [131,132]. Various techniques have been developed for the growth of thin films, based on either physical or chemical mechanisms.

Physical vapor deposition (PVD) is a film growth process based on physical procedures that involve evaporation and deposition of a material. The most common PVD mechanism is sputtering. Sputtering was first discovered in 1852 by the English physicist Grove [133], when he observed a metallic deposit in the inner wall of a glass cathode of a cold cathode glow discharge, but the wide implementation of sputtering started in the 1960's. Sputtering is a momentum and energy transfer process. During sputtering, positively charged ions of a gas, usually argon, accelerated by an applied electrical field, bombard the surface of a target (cathode), and dislodge its atoms which are finally deposited onto a substrate (anode).

The sputtering yield depends on target material, the binding energy of atoms on target's surface and the energy, mass and incident angle of ion [131,134,135]. The necessary and sufficient condition for the sputtering process is the energy of the incident particle to be higher than the binding energy of the atoms on the surface of target. Depending on the kinetic energy of the incident particle four different processes take place [134,136,137]. (i) When the energy of the incident particle is low (20-50eV), the sputtering yield is almost zero, since the incident particle can hardly remove a target atom. (ii) When the energy of incident particle is between 50eV and 1keV, a range known as knock-on sputtering regime, the incident ion transfers its momentum in an atom of the target, which is recoiled and strikes one or several atoms. The sputtering yield, here, depends on the mass and the kinetic energy of the incident particle and the target's surface topology. (iii) At energies between 1keV-50keV the projectile creates a cascade of atomic collisions, as it has and energy high enough to break the of target atoms' surface bonds, and produce an avalanche of secondary particles after the initial strike, leading to the removal of target atoms. (iv) Finally, at energies higher than 50keV the incident particle may be embedded in target or cause electron, X-ray and optical photon emissions.

Depending on the way that glow discharge for the formation of projectiles is created, the sputtering is divided into direct current (DC) and radio frequency (RF) [131,134,137,138]. Historically, the first sputtering source was the DC diode, due to the simplicity of the method. The glow discharge in DC sputtering is created between two parallel electrodes by applying a high voltage (1-5kV) with a gas pressure in the range 0.075 to 0.12Torr (figure 4.1(a)). DC sputtering however suffers from low deposition rates, high operating pressures and the targets are limited to conductive materials. Insulators and most semiconductors cannot be sputtered with a DC source, since the target becomes

progressively electrically positively charged by the incident ions, and the glow discharge is interrupted.

In contrast, in an RF diode the potential oscillates from positive to negative and therefore the potential developed on surface target is such that the flux of cation and electrons is equal regardless of the applied voltage. The time needed to charge the electrode is of the order of microseconds. Thus, for frequencies lower than MHz a series of short-term discharges to the two electrodes in alternating anode-cathode modes is produced. At high frequencies, the two electrodes acquire a negative potential, due to the greater mobility of electrons. If now the two electrodes have different size, the smaller will have larger current density and, by adding a capacitor between them, an electrical potential difference can be obtained. In practice, a capacitor system is used to match the impedance of the load to that the RF power supply (13.56MHz). This ensures that the full power is transferred to the glow discharge process minimizing the reflected power that could damage the circuit elements.

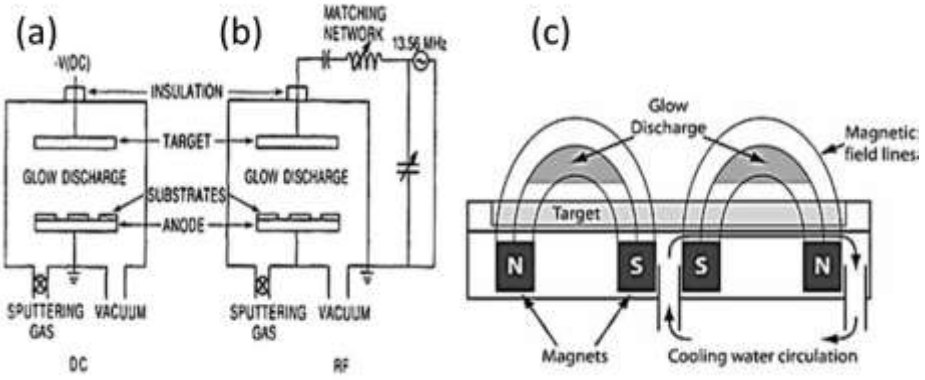

Figure 4.1: A schematic diagram shown sputtering options and electric glow discharge formed by (a) DC, (b) RF source. (c) Magnetron sputtering source.

Usually, DC and RF sputtering are magnetically assisted to enhance the sputtering yield [134,137,138]. The magnetic field traps the electrons in the geometric locus where it is perpendicular to the electric field, and effectively increases the electron path length to anode, increasing the number of collisions per electron in the plasma (figure 4.1(c)). The major disadvantage of magnetron sputtering is the limited area of the target which is eroded; during magnetron sputtering eroded ruts are created on the target.

4.2 Self-Assembly of Nanosphere Monolayer

Today, there is widespread interest in nanomaterials and their size dependent properties. Metal nanostructures have generated much of this interest, due to their wide applications in data storage and optoelectronics. One approach to creating auitable metal nanostructures is through nanosphere lithography [46,139]. Nanosphere lithography allows both control of the nanostructure's size and the shape. In this work, nanospheres were used either as a template for the deposition of nanocaps or as a mask for the formation of triangular-like islands.

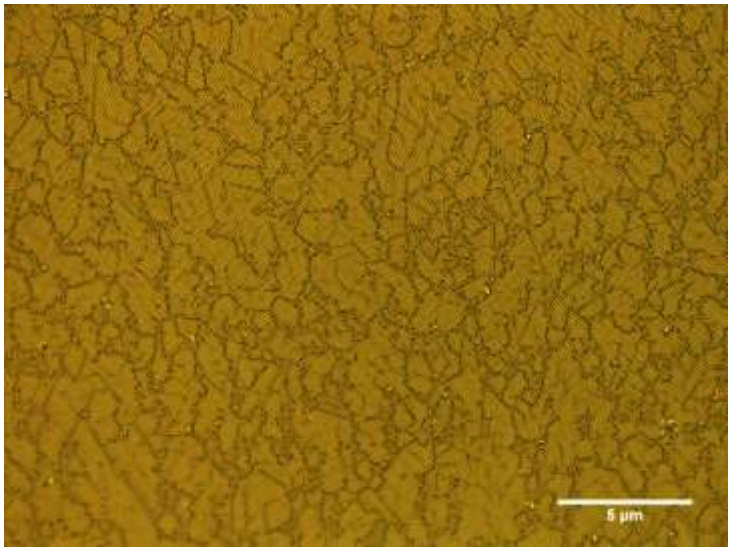

Figure 4.2: Optical microscope image of a monolayer of 970nm nanospheres.

Monodisperse polystyrene nanospheres with average sizes (970±23)nm and (173±6)nm were purchased from Gmbh Berlin (PS Research Particles aqueous suspensions 10% w/v LOT: PS-R-L2119 and 5% w/v LOT: PS-R-B1164, respectively). In order to form a nanosphere monolayer on Si/SiO_2 substrates (figure 4.2) dilute colloidal suspensions of these nanospheres were spread on appropriately prepared substrate surfaces according to the following process: First the substrates were sonicated for 2 hours in piranha solution (mixture 3:1 v/v concentrated 98% sulfuric acid to 30% hydrogen peroxide solution), rinsed with distilled water in order to remove the acids, sonicated in Isopropyl Alcohol for 15 minutes and finally dried in N_2 gas. Then 50μL of the nanosphere

colloidal suspension was deposited on the substrate surfaces which were then tilted vertically and left to dry for three hours at room temperature.

4.3 X-Ray Diffraction (XRD) and Four Circle XRD

Crystal structures consist of periodic arrangements of atoms or molecules. Generally, in these regular arrangements, atom containing planes lying along different directions, not only horizontally and vertically but also diagonally, so-called crystallographic planes, may be identified. X-rays can be diffracted by these crystallographic (or crystal, for short) planes, since the wavelengths of X-rays and the lattice constants of crystals are of the same order of magnitude. Let us assume a parallel monochromatic beam of X-rays, with a single wavelength λ, incident on a family of crystal planes with interplanar distance d, at an angle theta (θ) and the condition that each atom of crystal acts as a scattering center and creates a secondary wave. All secondary waves are then superimposed to create a reflected wave. All these reflected waves interfere with each other. If the condition "phase difference = integer multiple of wavelength" ($\Delta\varphi=n\lambda$) is not satisfied, then the interference is destructive. In the case that the waves are in phase then the interference is constructive. For a fixed wavelength and a fixed lattice planes separation this requirement is satisfied for a given angle, which is called Bragg angle. Constructive interference occurs, if the paths of two waves, which are scattered by the planes P and Q, are equal under the condition that the angle between the atomic plane and incident beam is equal to the angle between this atomic plane and the scattered beam [140,141,142]. From the above it is a necessary diffraction condition that the path difference of be an integral multiple n of wavelength λ:

$$n\lambda = \overline{SQ} + \overline{QT} \tag{4.1}$$

$$n\lambda = 2d_{hkl}\sin\theta \tag{4.2}$$

Equation 4.2 is known as Bragg's law (figure 4.2), where n is the order of reflection, λ is the wavelength of X-rays and d_{hkl} is the interplanar spacing.

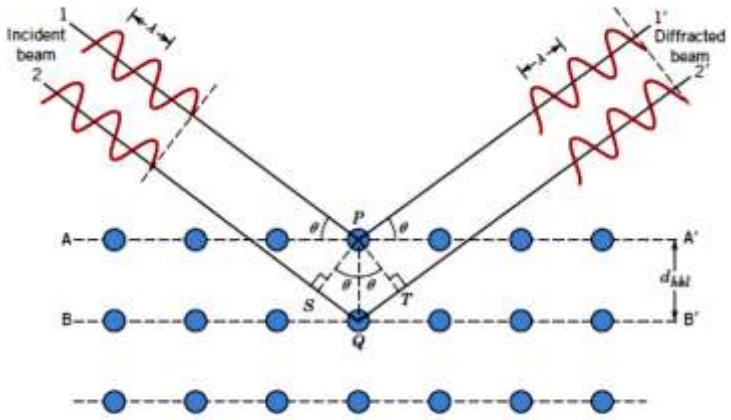

Figure 4.3: Geometrical illustration of Bragg's law [141].

Film texture is the non-random distribution of the crystallographic orientation of grains. One approach for depicting the texture of films is the construction of pole figures, where a specified crystallographic orientation from each of a representative number of crystallites is plotted in a stereographic projection as a function of the pole density distribution of the crystallographic directions of sample [143,144,145]. Pole figures can be obtained with a four circle X-ray diffractometer. The term "four-circle diffractometer" signifies that during data collection four different degrees of freedom are varied: 2θ, χ or ψ, φ and ω (figure 4.4(a)). During measurement the diffraction angle (2θ) is constant and the diffracted intensity is collected by varying two geometrical factors (φ and ψ) and combining them (figure 4.3(b)). The first is the tilt angle ψ (from 0^o to 90^o), which is the angle of the sample surface to the normal direction, i.e. the angle ψ specifies the tilting of the sample normal s_3 as a function of the scattering vector Q or the scattering plane. Usually, the tilt angle ψ can be replaced by χ where $\chi=90^o-\psi$. The other factor is the rotation angle φ (from 0^o to 360^o), which is the azimuth angle around the sample surface normal. Pole figure data provide information about the preferred orientation and texture analysis of films and the epitaxial relationship between a substrate and a film.

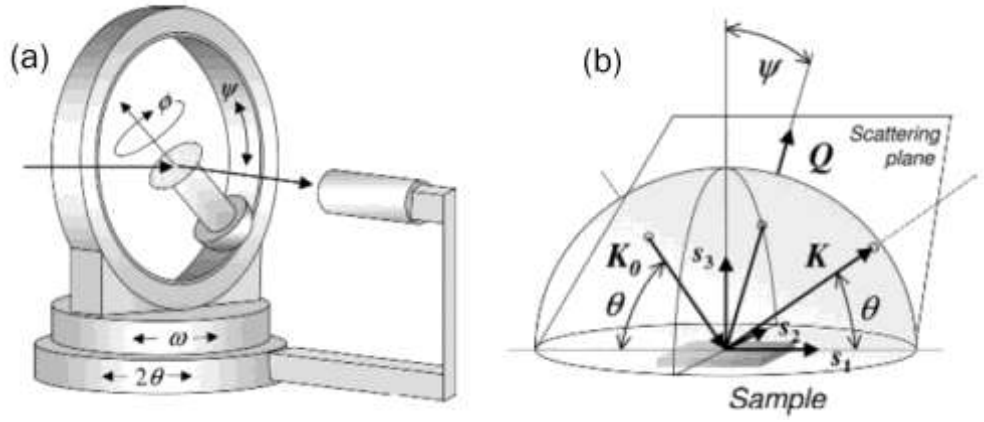

Figure 4.4: (a) Four-circle X-ray diffractometer and the 4 different variables angles: 2θ, χ or ψ, φ and ω, (b) the tilted ψ angle from the viewpoint of sample surface [143].

4.4 Grazing Incidence X-Ray Diffraction (GIXRD)

Grazing Incidence X-ray Diffraction (GIXRD) or Grazing Incidence Diffraction (GID) is a powerful characterization technique for polycrystalline thin films on single crystal or amorphous substrates, owing to the surface sensitivity of the method. Thin films have a low number of diffraction planes, due to their small volume, and their characterization with conventional Bragg-Brentano XRD is limited, since the diffracted intensity is low compared to the intense background and substrate signal. In contrast, GIXRD, usually combined with a parallel beam geometry, can overcome the above limitations; the angle of the incident beam and sample surface is very small (typically 1^o to 3^o) resulting in an increased X-ray path length within the film. Thus, the diffracted intensities from film are increased, while the diffracted intensities from the substrate and the substrate are reduced GIXRD diffraction is carried out at an incident angle α, between the incident beam and sample surface, which approaches the critical angle (the angle where total reflection occurs) of the film, and is kept constant.

Compared to the standard X-ray diffraction measurement which follows the geometry θ/2θ, in GIXRD configuration the geometry is α/2θ-α, where 2θ-α is the angle formed between the outgoing beam and sample surface. The scattering vector Q follows a route starting from a position close to sample normal s_3 ending at a position close to the

incoming beam K_0 (figure 4.5) Thus, GIXRD monitors the interplanar spacing of the inclined vertical crystal planes [143].

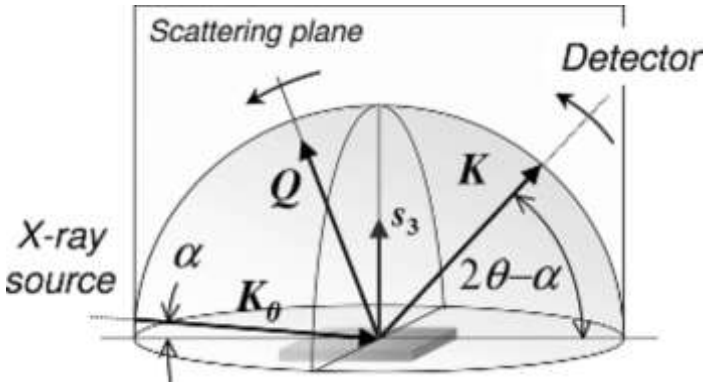

Figure 4.5: GIXRD geometry is characterized by small and constant incident angle α. The collected data arise mostly from the volume of the sample film [143].

GIXRD provides information about phase analysis on very thin films (10nm), surface sensitivity down to nm scale, depth profiling of the phase composition of layered samples and the crystallographic structure.

4.5 X-Ray Reflectivity (XRR)

X-ray reflectivity (XRR) is a powerful technique for the characterization of thin films and multilayers. XRR measurements allow the extraction of information on density, thickness and roughness of thin film surfaces and interfaces. A typical XRR specular curve of 245Å Co grown on Si is shown in figure 4.6. The XRR pattern contains the critical angle θ_c, whose position gives the electron density of film, the interference fringes, whose period gives the film thickness and finally the roughness.

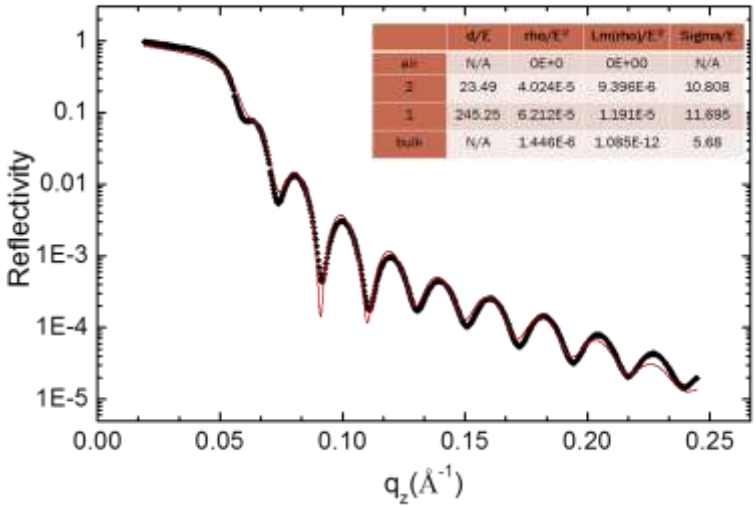

Figure 4.6: XRR pattern of a single layer of Co on Si substrate. (Inset: XRR pattern fitting parameters).

In the X-ray region, the condensed matter refractive index (n) is slightly less than unity and is given by:

$$n = 1 - \delta + i\beta \tag{4.3}$$

,where δ and β are the dispersion and absorption indices, respectively. The real part, 1-δ, is connected to the phase-lag of the propagating wave and the imaginary part, iβ, indicates the decrease of wave amplitude. XRR is one way to solve equation (4.3). The determination of the δ and β values reveals the density of a material.

For incident angles below a critical angle, $\theta_c = \sqrt{2\delta}$, total reflection occurs. For greater angles the incident beam penetrates inside the film. In this case, Kiessig oscillations or fringes are appeared (figure 4.6). Maximum intensities are observed when the interference Δ between refracted and reflected beam is a multiple of the wavelength λ, and the phase shift is given by:

$$\Delta = 2t \sin\theta_t \tag{4.4}$$

Equation (4.4) is related to the Bragg equation (4.2), with the film thickness t substituting for the interplanar spacing d [143]. The thickness of a single layer can be determined by the relation:

$$\theta_m^2 = \theta_C^2 + \left(\frac{\lambda}{2t}\right)^2 m^2 \tag{4.5}$$

,where m is an index for each oscillation. The θ_m^2 as a function of m^2 plot consists of points falling on a straight line, where the slope can be used for the determination of film thickness by:

$$t = \frac{\lambda}{2\sqrt{slope}} \tag{4.6}$$

For multilayers more information can be found in [143,146].

Surface and interface roughness increase the diffuse scattering, resulting in a reduction of the reflected intensity. According to Névot and Croce [147] the roughness can be determined by adding an error function to the average electron profile along the specimen normal.

4.6 Transmission Electron Microscopy (TEM) and High Resolution Transmission Electron Microscopy (HRTEM)

Transmission Electron Microscopy (TEM) is one of the most powerful techniques for the study of material's microstructure on a nanoscopic scale. Even though X-ray diffraction provides better quantitative information, electron diffraction has an advantage in that electrons can be focused using electromagnetic lenses. This advantage allows images with a resolution of a few nanometers to be obtained. The accelerated electrons, accelerated to energies of the order of hundreds of keV, are focused on ultra-thin specimens, yielding information on morphology, particle size, the structural properties and the crystalline state of the material, variations in the crystallinity and local stoichiometry [148]. An advantage of the technique is the easy switching from the imaging mode (figure 4.7(a)) to the diffraction mode, known as selected area electron diffraction (SAED) (figure 4.7(b)), enabling the crystallographic properties of a specific sample area to be studied. Energy dispersive X-ray spectroscopy (EDX) is often combined with TEM for the chemical characterization and elemental analysis.

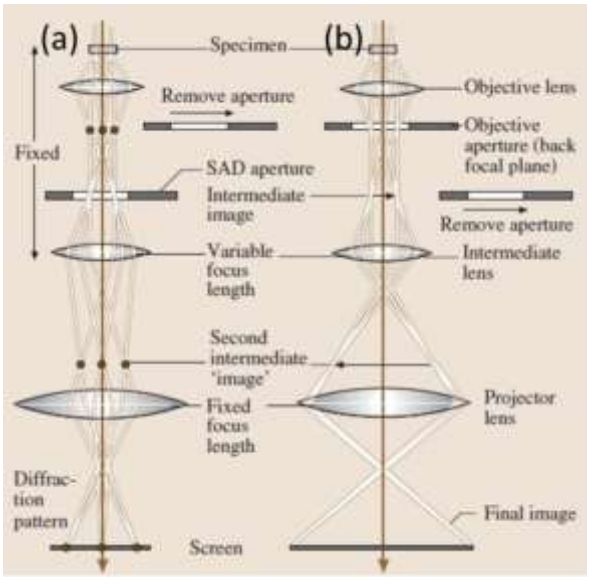

Figure 4.7: Transmission electron microscope in (a) diffraction and (b) imaging mode [149].

High resolution transmission electronic microscopy (HRTEM) is widely used for the analysis of crystal structure and lattice defects at the atomic scale. The HRTEM images depend on the visual imaging factors of the electron lenses and on the local electron scattering [149,150]. The HRTEM has become a standard addition to modern microscopes, due to the technological progress in improving the overall derogation of the nosepiece. Under defocus condition, called Scherzer defocus, HRTEM images show the atomic arrangement of individual atomic alignments along the electron beam. The HRTEM images depend on the defocus condition, the sample thickness and the depth of the object. The individual arrangements can be obtained by comparing the experimental images taken under different defocus conditions with theoretical images simulated for model structures using dynamic theory. HRTEM resolution is of the order of 0.2nm.

4.7 Atomic Force Microscopy (AFM)

Atomic force microscopy (AFM) was first introduced by Binning, Quate and Gerber in 1986 [151] and is a very powerful tool for topographical imaging on an atomic scale and dimensional metrology of surface features. AFM is carried out via a fine ceramic or semiconductor tip, usually Si or Si_3N_4, which raster scans over the surface. The AFM operates with the tip in either contact or in tapping mode, each mode having distinct

advantages. The tip radius is of the order of 20 nanometers and can achieve resolutions down to several Angstroms. The tip is positioned at the edge of an oscillating cantilever with the force applied between tip and surface being of the order of 10^{-11} to 10^{-6} N. The cantilever is the most important part of AFM, as it both determines the forces applied and the lateral resolution [152]. As the tip is drawn or pulled away from the surface, the cantilever deviates due to local forces. The size of the deviation is monitored by a laser beam, which is reflected at an obtuse angle from the end of the oscillating cantilever. The deviation of the laser beam is thus relative to the position of the tip over the sample surface and, being rastered over the entire surface, gives a map of the surface topography (figure 4.8).

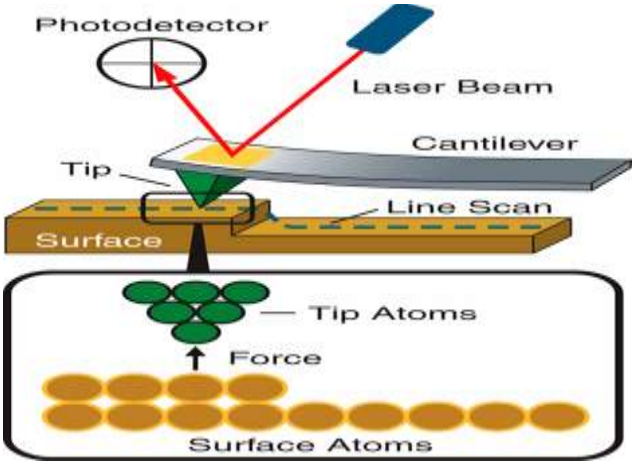

Figure 4.8: The operating principle of atomic force microscopy.

The AFM can be operated in several modes such as nanomechanical, nanoelectrical and peak-force modes, and magnetic force microscopy, described below.

4.8 Magnetic Force Microscopy (MFM)

Magnetic force microscopy (MFM) operates similarly to AFM, with the that the MFM probe is coated with a few nanometers thick layer of a ferromagnetic material, usually Co. During scanning the distance between tip and surface sample is at least 15nm. As a result the microscope senses the magnetic stray fields from the sample surface and the final image contains information on sample's magnetic state and topography (figure 4.9).

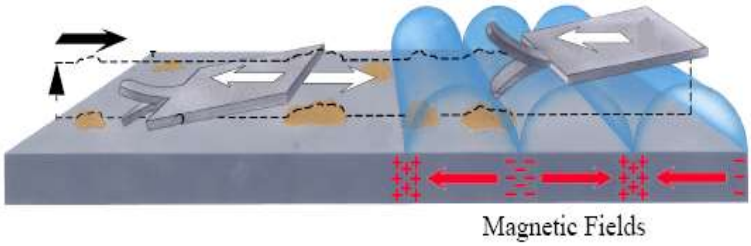

Figure 4.9: The operation principle of MFM.

MFM resolution is estimated better than 30nm, but it depends strongly on the shape of the tip, the thickness of ferromagnetic coating and the distance between sample surface and tip. Most applications of MFM are in magnetic recording in the study of magnetic nanostructures, signal-to-noise ratio, and transition jitter.

4.8 Vibrating Sample Magnetometer (VSM)

The Vibrating Sample Magnetometer (VSM) measures magnetic moments to better than $10^{-8}Am^2$ [1]. The VSM operating principle is based on Faraday's law, which states that a changing magnetic field generates an electromotive force in a coil [153]. When a sample is vibrated in a homogeneous magnetic field it can induce an electrical signal into suitably located fixed coils. The signal frequency matches that of the sample oscillation, while the signal's magnitude is proportional to the magnetic moment as well as to the vibration amplitude and oscillation frequency.

In its usual experimental set up, the sample is placed within the pole gap of an electromagnet at the end of a non-magnetic rod, while the other end is mounted on a transducer which imparts a vertical oscillation to the sample. Suitable pick-up coils are positioned on pole pieces of the electromagnet and these detect the induced signal (figure 4.10).

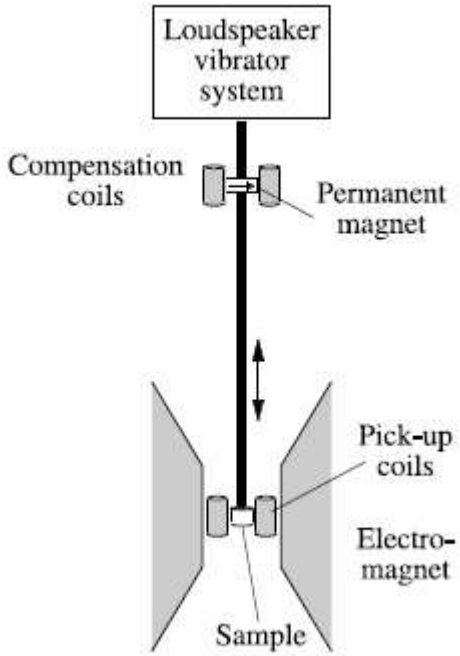

Figure 4.10: Schematic view of vibrating sample magnetometer.

The values of the magnetic moment is obtained simply by measuring the amplitude of the signal, calibrated using a known mass of a standard material (e.g. Nickel sphere) with corrections for errors arising from variations in the amplitude and frequency of oscillation being carried out using Lock-in amplification and other filters and compensation techniques [149].

4.9 Alternating Gradient Field Magnetometer (AGFM)

The Alternating Gradient Field Magnetometer (AGFM) is a useful technique for measuring the magnetic moment of films which have low mass and thus low total magnetization. The AGFM sensitivity is of the order of $10^{-10}Am^2$, better than VSM and similar to that of SQUID magnetometers. The AGFM determines the magnetic moment by measuring the external force produced by an alternating magnetic gradient field applied by an appropriate coil pair in addition to the DC magnetizing field. The sample is mounted at the end of a flexible fiber and both DC and AC fields are applied. The gradient field causes an alternating force, which oscillates and flexes the fiber. The sample is mounted on a

piezoelectric bimorph which detects the vibration amplitude, the magnitude of the deflection being proportional to the sample moment. With the vibration frequency tuned to the system's natural resonance the sensitivity is increased by a Q-factor, typically 100 [70,154].

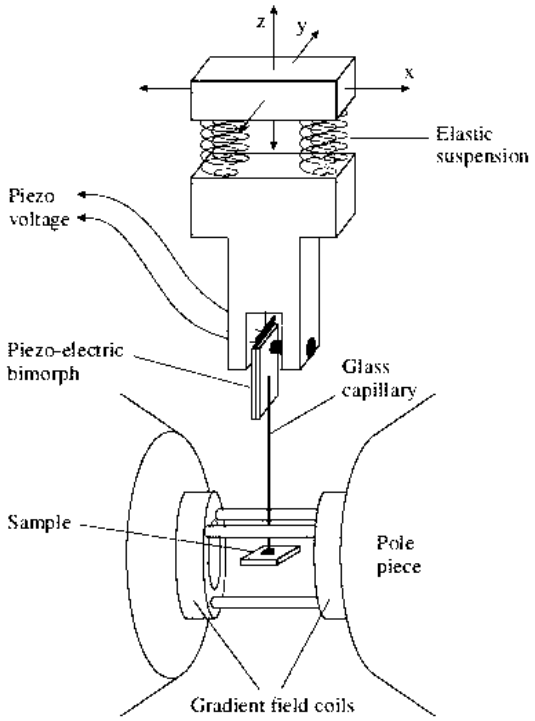

Figure 4.11: Schematic view of AGFM [149].

CHAPTER 5

5. Order-Disorder Study of $L1_0$-CoPt and $L1_2$-$CrPt_3$ Films

$L1_0$-CoPt and $L1_2$-$CrPt_3$ thin films have attracted considerable attention for ultra-high density magnetic recording and magneto-optical recording, respectively, due to their large magnetocrystalline anisotropy. The order-disorder transformation of the above alloys is affected by the thickness and layering of thin films. Thus, it is of great interest to study the structural transformation from the chemically disordered to chemically ordered phase with thermal annealing, in films with different thickness and layering, and correlate the structural and microstructural characterization to the observed magnetic properties.

This chapter is separated into two parts; the first part includes the magnetic and structural characterization of $CrPt_3$ films and the second the structural characterization of CoPt films. As for chemically ordered $CrPt_3$ films previous studies focused on the magnetic properties and polar Kerr rotation as a function of chemical long range ordering, crystal orientation [81,155], stoichiometry and film thickness [156,157]. In this chapter, we study the influence of layering and alloy composition on the structural and magnetic properties of magnetron sputtered $CrPt_3$ films. Apart from XRD and GID patterns, and magnetic hysteresis loops, we also study the angular dependence of the coercivity in order to probe the magnetization reversal processes. To the best of our knowledge, no reports have been made on the magnetization reversal of ordered $CrPt_3$ films to date. The second part contains the in-situ GID study of order-disorder transformation of CoPt single layers, bilayers and trilayers. Supplementary but crucial information on the effects of layering and thickness contain TEM images and XRR patterns.

5.1 Experimental Details

CoPt films (34nm), Co(17nm)/Pt(17nm) bilayers and Co(3nm)/CoPt(6nm)/Pt (3nm) trilayers have been deposited by magnetron sputtering on oxidized silicon wafers at RT using a MANTIS deposition system with Co (3") and Pt (2") sources in confocal geometry. The substrates are rotated during deposition. Prior to deposition the chamber is evacuated to a base pressure of 7×10^{-7}Torr with a process gas (Ar 5N) pressure of 2.5mTorr. The stoichiometry of the CoPt alloy films was determined by EDX to be $Co_{54}Pt_{46}$. The Co layers were deposited at a rate of 0.54Å/sec at an applied power of 76.5W DC and the Pt layers at a rate of 0.52 Å/sec at 120W RF. X-ray diffraction (XRD) data were collected with a Bruker D8 Advance Diffractometer using $CuKa_1$ (λ=1.5418Å) and a secondary graphite monochromator. The samples had first been placed inside a high temperature vacuum furnace and the XRD data were subsequently collected during cumulative annealing. TEM observations were carried out employing JEOL 3010 TEM analytical electron microscopes. Plane view samples were prepared by single side polishing and ion milling, and the cross-section samples consist of a sandwich structure prepared by conventional lapping and polishing techniques followed by ion milling.

CrPt (64nm) formed by simultaneous Cr and Pt co-deposition with appropriate deposition rates and trilayers Cr(10.5nm)/CrPt(32nm)/Pt(21.5nm) were grown on thermally oxidized Si(100) substrates with 500nm thick SiO_2 layer at room temperature (RT). For the deposition we used the aforementioned Mantis UHV magnetron sputtering system with Cr (3") and Pt (2") sources in a confocal geometry. The substrates were rotated at a rate of 22 rpm during deposition, in order to ensure homogenous growth of the films. Prior to the deposition the chamber is evacuated to a base pressure of 8×10^{-7} Torr. During deposition the process gas (Ar 5N) pressure is 4mTorr. $CrPt_3$ films with controlled composition were obtained by adjusting the Cr layer deposition rates (0.09-0.14Å/sec) and by keeping the Pt layer deposition rate (0.54Å/sec) constant via application of 120W RF. The Cr_xPt_{1-x} (x=0.21-0.24) film composition was determined by EDX. After deposition the samples were sealed in quartz tubes under a vacuum (< 9mTorr) and then annealed at temperatures of 750, 850 and 850 ^oC for 6h.

X-ray diffraction data were collected as before with a D8 Advance Bruker Diffractometer. Magnetic measurements were carried out using a Lakeshore 7300 Vibrating Sample Magnetometer (VSM) at RT.

5.2 Structural and Magnetic Characterization of Cr_xPt_{1-x} films

XRD patterns are illustrated in figure 1 for the as-sputtered $Cr_{26}Pt_{74}$ trilayer (figure 5.1(a)), $Cr_{26}Pt_{74}$ co-deposited (figure 5.1(b)) and $Cr_{26}Pt_{74}$ trilayer (figure 5.1(c)) both annealed at 800 ^oC for 6 h. All films show (111) preferred orientation. Only the fundamental (111) and (200) peaks are observed indicating that the as-sputtered film is in the chemically disordered fcc A1 structure. On the contrary, the annealed films are possess the chemically ordered $L1_2$ structure, as evidenced by the appearance of the (001), (110), (210) and (211) superstructure peaks.

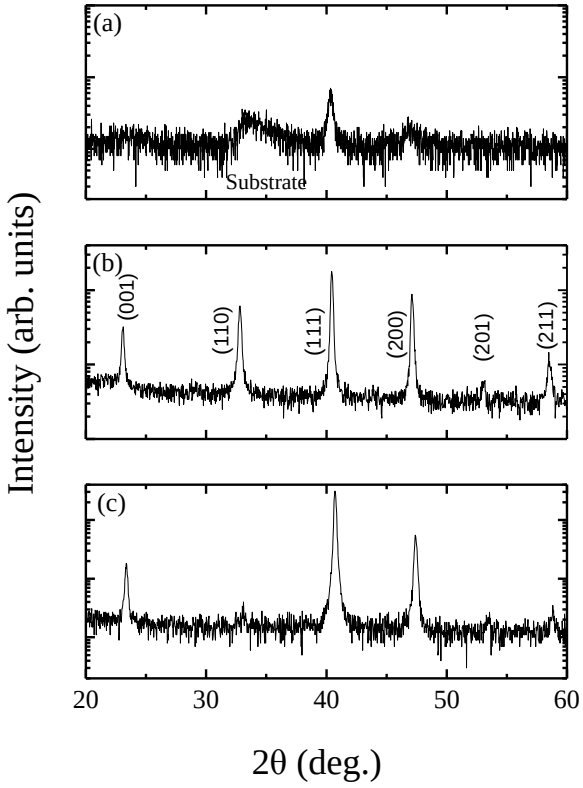

Figure 5.1: XRD patterns for (a) as sputtered $Cr_{26}Pt_{74}$ trilayer, (b) $Cr_{26}Pt_{74}$ co-deposited film annealed at 850 ^oC, (c) $Cr_{26}Pt_{74}$ trilayer annealed at 800 ^oC.

The chemical long range order parameter S is a valuable tool for determining the extent of A1 to $L1_2$ transformation. This is estimated using the function $S^2 = \frac{\left(I_{001}/I_{200}\right)_{exp}}{\left(I_{001}/I_{200}\right)_{calc}}$ [59,158], where I_{001} and I_{200} are the integrated intensities of the $CrPt_3$ superstructure (001) and fundamental (200) diffraction peaks, respectively. Figure 5.2 shows the temperature dependence of the chemical long range order parameter. For both co-deposited and trilayer films the order parameter increases with temperature and shows maximal values at a temperature of 850 ^{o}C. In our samples the maximum order parameter S=0.95 is achieved for the co- $Cr_{24}Pt_{76}$ film deposited at 750 ^{o}C. In reference to atomic composition the order parameter, as expected, shows larger values for films with stoichiometry x=0.23-0.26 i.e. close to 1:3 (Cr:Pt) atomic ratio. On the contrary, when the atomic composition differs from the ideal 1:3 ratio the maximum achievable order parameter is stoichiometry limited. As regards the influence of layering, in the trilayers higher a degree of ordering can be achieved compared to co-deposited films.

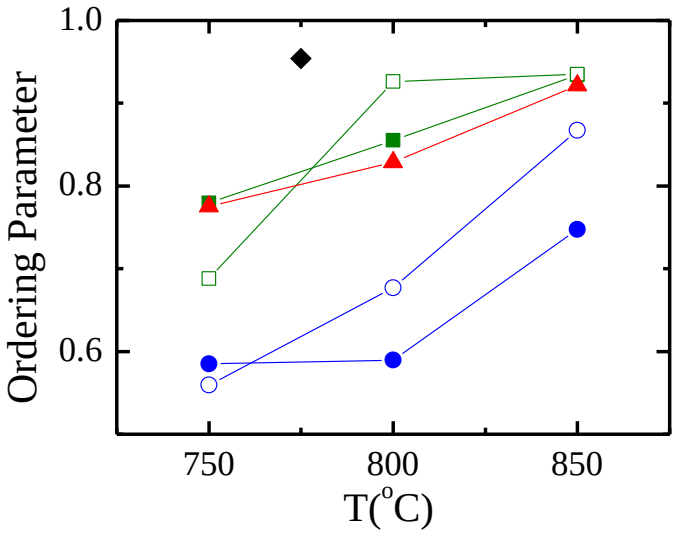

Figure 5.2: Chemical long range order parameter S as a function of annealing temperature for $Cr_{26}Pt_{74}$ co-deposited film (solid squares), $Cr_{26}Pt_{74}$ trilayer (open squares), $Cr_{24}Pt_{76}$ co-deposited film (solid diamond), $Cr_{23}Pt_{77}$ co-deposited film (solid triangle), $Cr_{21}Pt_{79}$ co-deposited film (solid circles) and $Cr_{21}Pt_{79}$ trilayer (open circles).

Figure 5.3 shows the in-plane and out-of-plane magnetization hysteresis loops of $Cr_{26}Pt_{74}$ monolayer and trilayer samples annealed at 800 ^{o}C for 6 h. It is clear that both films show strong perpendicular magnetic anisotropy. The coercivities (H_C) are 3.4 and 4.1 kOe for the monolayer and trilayer, respectively.

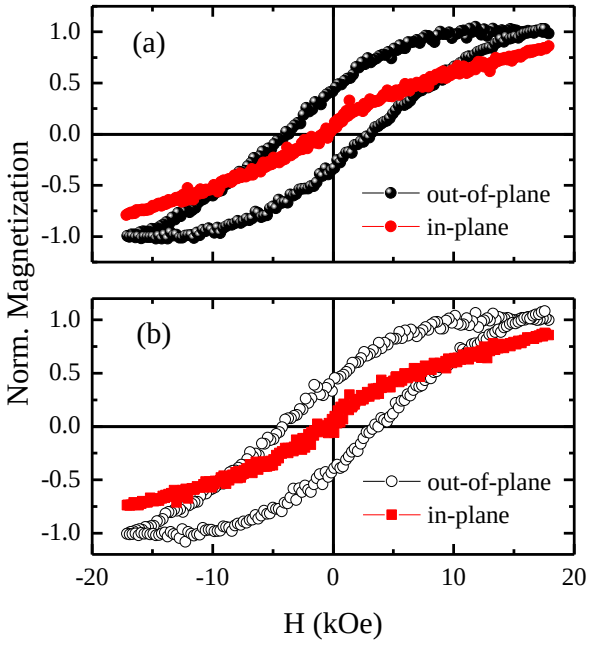

Figure 5.3: In-plane and out-of-plane magnetization hysteresis loops for (a) $Cr_{26}Pt_{74}$ co-deposited film (b) $Cr_{26}Pt_{74}$ trilayer both annealed at 800 ^{o}C for 6h.

The out-of-plane H_c as a function of annealing temperature for all films is shown in figure 5.4(a). Even though the chemical order parameter increases with temperature, the coercivity field follows an inverse trend and decreases with the temperature, as a result of the degradation of texture at high temperatures (5.4(b)). In the atomic composition range x=0.23-0.26 both co-deposited and trilayers films show larger values of coercivity and for $Cr_{26}Pt_{74}$ trilayer the coercivity field becomes 5.8kOe at 750 ^{o}C. Increasing the Pt atomic composition of the out-of-plane coercivity decreases and approaches the value of 1.4kOe ($Cr_{21}Pt_{79}$ co-deposited film) at 750 ^{o}C. With regard to the effect of layering it is observed that trilayers have larger coercivity fields than co-deposited films at all temperatures. For

example at 750 ^{o}C $Cr_{26}Pt_{74}$ trilayer coercivity is 5.8kOe while that of co-deposited film is 5.2kOe.

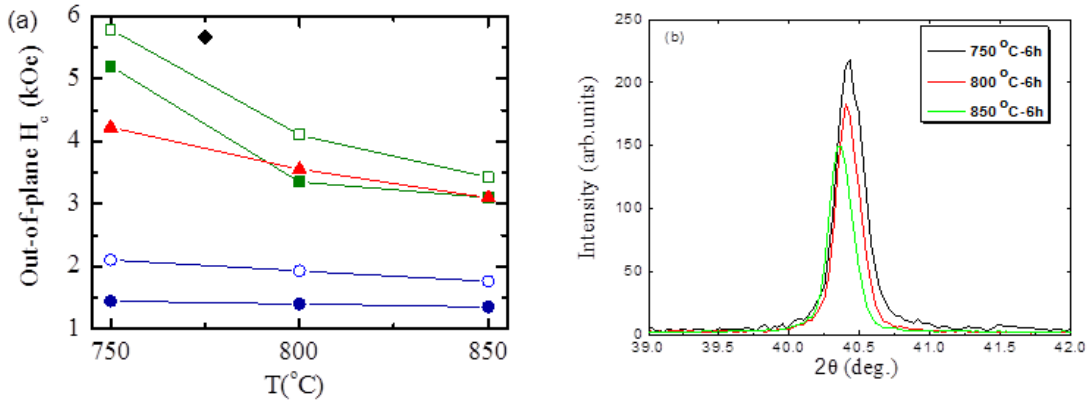

Figure 5.4: (a) Coercivity H_c as a function of annealing temperature for $Cr_{26}Pt_{74}$ co-deposited film (solid squares), $Cr_{26}Pt_{74}$ trilayer (open squares), $Cr_{24}Pt_{76}$ co-deposited film (solid diamond), $Cr_{23}Pt_{77}$ co-deposited film (solid triangle), $Cr_{21}Pt_{79}$ co-deposited film (solid circles) and $Cr_{21}Pt_{79}$ trilayer (open circles). (b) XRD pattern of $Cr_{26}Pt_{74}$ trilayer showing degradation of texture with annealing temperature.

The angular dependence of the remanence coercivity H_{RC} (defined as a reverse field which gives zero remanence) is shown in figure 5.5(a) for co-deposited and trilayers films with composition $Cr_{26}Pt_{74}$ at different annealing temperatures (750 ^{o}C, 800 ^{o}C and 850 ^{o}C). It seems that the angular dependence of remanence coercivity does not exhibit the characteristics expected for either nucleation (Stoner Wohlfarth model) or pinning controlled reversal (1/cosθ law). For co-deposited films the H_R increases with the angle ψ between the alignment axis and the applied field. This means that the reversal mechanism for the co-deposited films is that of domain wall pinning, although the expected angular dependence would be more drastic in this case. On the contrary, the trilayers have a different behavior; at 750 ^{o}C there is no evidence of pinning. Although the coercivity field values do not indicate the dominance of one of the two reversibility mechanisms of, it seems that for the trilayers there is a lesser decrease of the coercivity field upon annealing at high temperatures. Figure 5.5(b) shows the coercivity ratio H_{RC}/H_C as a function of the angle to the easy axis. This ratio can be used as a criterion of reversibility of the hysteresis curve demagnetization quadrant. The data presented include different heat-treatment temperatures (750 ^{o}C, 800 ^{o}C and 850 ^{o}C) for both co-deposited and trilayer films with

composition $Cr_{26}Pt_{74}$. As a general remark for both co-deposited films and trilayers the reversibility is reduced with increasing annealing temperature.

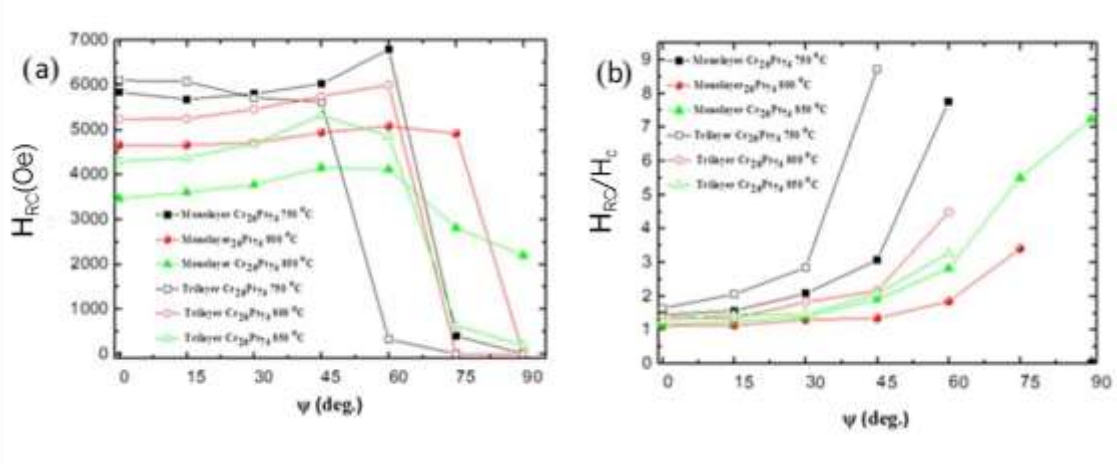

Figure 5.5: (a) Angular dependence of remanence coercivity H_{RC} of monolayers and trilayers at different annealing temperatures, (b) reversibility of monolayers and trilayers at different annealing temperatures.

5.3 In-situ GIXRD Study of CoPt Single Layer, Bilayers and Trilayers

Figure 5.6 shows the grazing incidence X-ray diffraction patterns of CoPt (36nm) single layers with cumulative annealing at different temperatures. At all annealing temperatures, the intense fundamental peak (111) indicates that the film is oriented along the [111] direction. Between 100 ^{o}C and 500 ^{o}C the fcc CoPt phase is dominant. The superstructure peaks (001), (110) and the incomplete splitting of (200) to (200) and (002) from 550 ^{o}C to 700 ^{o}C indicate the formation of the fct CoPt phase. The incomplete splitting of the (200) peak to (200) and (002) reveals the chemical ordering to be partial. Finally, at 750 ^{o}C, the superstructure peaks disappear and only the fundamental is observed, indicating that the film reforms in the fcc structure.

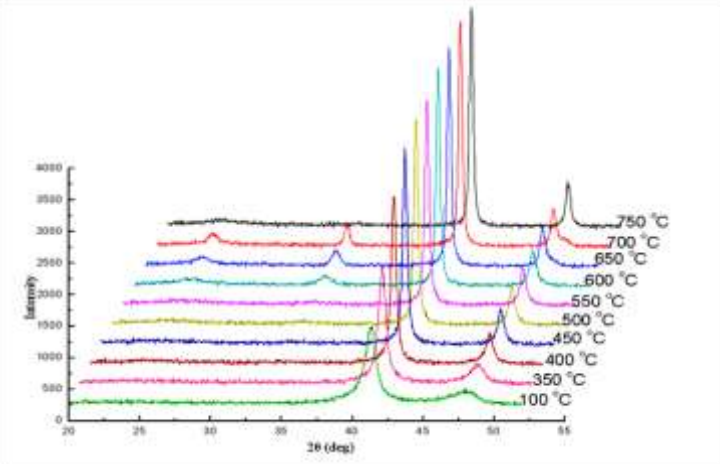

Figure 5.6: In-situ high temperature GIXRD patterns of CoPt(36nm) single layer.

The change of lattice constants a and c, in CoPt single layer unit cell, as a function of annealing temperature are shown in figure 5.7. The lattice constants a_{cub}, a_{tetr} and c_{tetr} are derived from the Bragg peaks of figure 5.6. During the A1 to $L1_0$ transformation the unit cell is deformed, resulting in an increase of a_{tetr} by approximately 2%, while the lattice parameter c_{tetr} is reduced by approximately 2.5%. In agreement with this expectation, figure 5.7 shows the increase of a_{tetr}, while at the same time the c_{tetr} is reduced. The lattice parameter a_{cub} is given over the entire range of annealing temperatures, as the A1 → $L1_0$ transformation is never fully accomplished and thus the fcc phase coexists with the fct between 550 °C to 700 °C. At 800 °C, the $L1_0$ phase disappears and only the fcc exists.

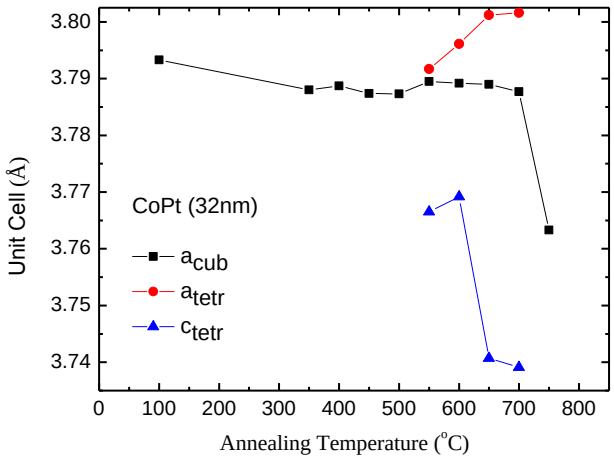

Figure 5.7: The lattice constants variation of CoPt(36nm) unit cell with annealing temperature.

Figure 5.8 shows the c/a ratio variation as a function of annealing temperature. The c/a ratio is reduced, i.e. increased tetragonality, with the annealing temperature.

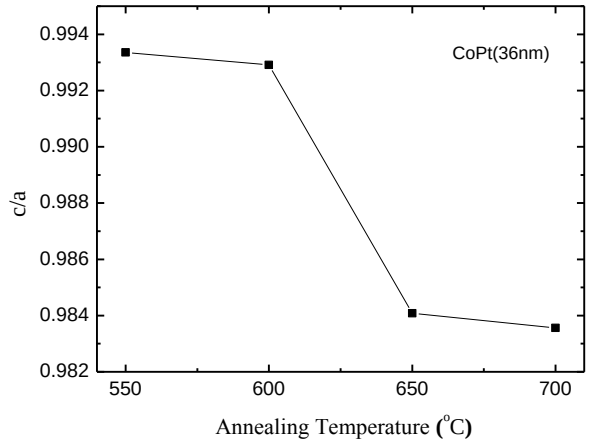

Figure 5.8: c/a ratio values of CoPt(36nm) single layer.

Figure 5.9 shows the grazing incidence X-ray diffraction patterns of Co(17nm)/Pt(17nm) bilayer with cumulative annealing at different temperatures. The fcc phase dominates at 500 °C. Between 550 °C and 700 °C the presence of superstructure peaks (001), (110) and the incomplete splitting of (220) to (200) and (002) indicates that the fct structure is formed. The complete splitting of (200) to (200) and (002) at 700 °C and 750 °C testifies that the fct structure dominates. Again, upon annealing at higher temperatures the sample returns to the fcc structure (not shown in figure 5.9).

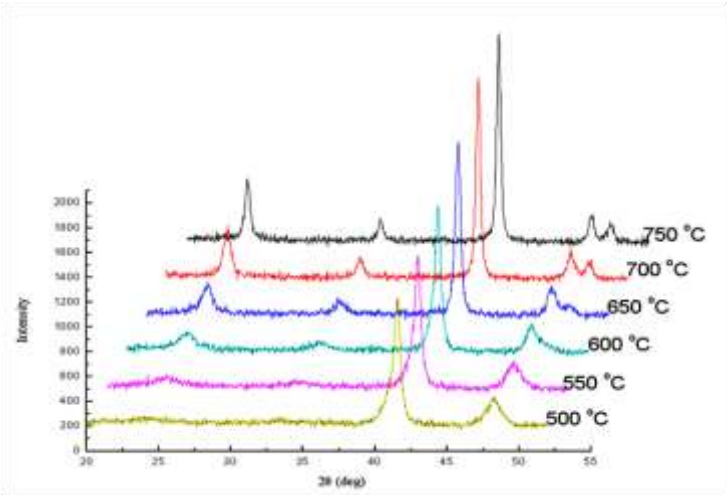

Figure 5.9: In-situ high temperature GIXRD patterns of Co(17nm)/Pt(17nm) bilayer.

The variation of lattice constants a and c in the Co/Pt bilayer unit cell as a function of annealing temperature are shown in figure 5.10(a). The lattice constants a_{cub}, a_{tetr} and c_{tetr} are obtained from the Bragg peaks of figure 5.9. Between 550 ^{o}C and 650 ^{o}C the two phases coexist. The fcc disappears above 650 ^{o}C and the fct structure is observed. The c_{tetr} decreases with temperature, while a_{tetr} increases until 650 ^{o}C and then decreases slightly up to 650 ^{o}C. Figure 5.10(b) shows the variation of c/a ratio values as a function of annealing temperature. A decrease of c/a ratio values is observed until the temperature of 650 ^{o}C, then a slight increase at 700 ^{o}C and finally a decrement again at 750 ^{o}C.

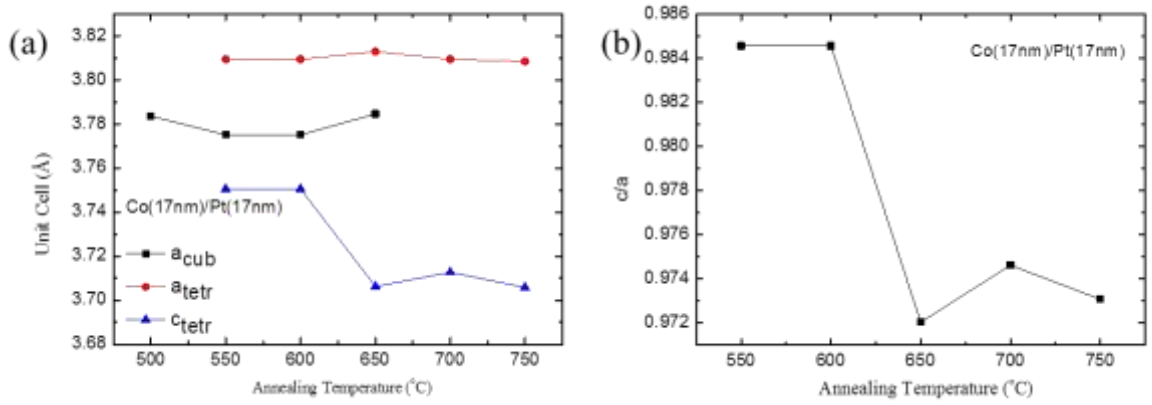

Figure 5.10: (a) Lattice constants variation of Co(17nm)/Pt(17nm) unit cell with annealing temperature, (b) c/a ratio values of bilayer.

Figure 5.11 shows the grazing incidence X-ray diffraction patterns of the Co(3nm)/CoPt(6nm)/Pt(3nm) trilayer with cumulative annealing at different temperatures. At all annealing temperatures, the strong fundamental peak (111) indicates that the film is oriented along [111] direction. Between 100 ^{o}C and 500 ^{o}C only the fundamental reflections (111) and (200) are observed, revealing that the structure is dominated by the fcc phase. Both fcc and fct phases coexist from 550 ^{o}C to 650 ^{o}C, evidenced by the appearance of superstructure peaks (001) and (110), but the (200)/(002) splitting is only partial. Annealing at higher temperatures results in complete (200) /(002) splitting and the fct phase dominates.

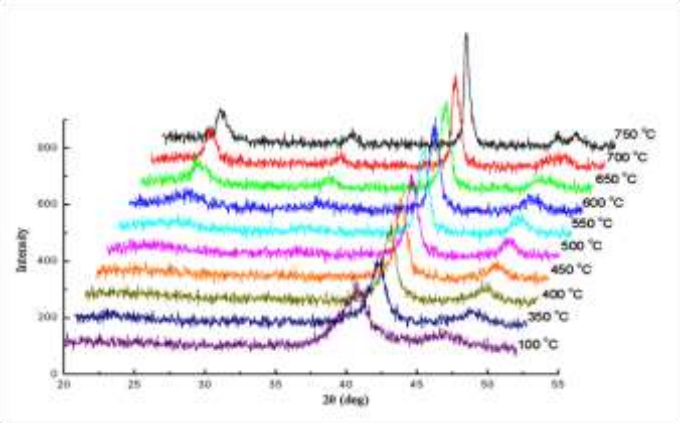

Figure 5.11: In-situ high temperature GIXRD patterns of Co(3nm)/CoPt(6nm)/Pt(17nm) trilayer.

The variation of lattice constants a and c, in unit cell of Co/CoPt/Pt trilayer, as a function of annealing temperature are shown in figure 5.12(a). The lattice constants a_{cub}, a_{tetr} and c_{tetr} are calculated from the Bragg peaks of figure 5.11. The sample has (111) texture for all annealing temperatures. The two phases coexist between 100 ^{o}C and 700 ^{o}C. The A1 to $L1_0$ transformation starts at 550 ^{o}C, above which the lattice parameters a_{tetr} and c_{tetr} are given. The lattice parameter a_{cub} decreases with temperature and at the temperature of 750 ^{o}C disappears, revealing that the fct structure predominates. Figure 5.12(b) shows the variation of the c/a ratio values as function of temperature. A decrease of c/a ratio is observed up to a temperature of 650 ^{o}C, followed by a slight increase at higher temperatures. Thus, the highest degree of chemical ordering is obtained at 650 ^{o}C.

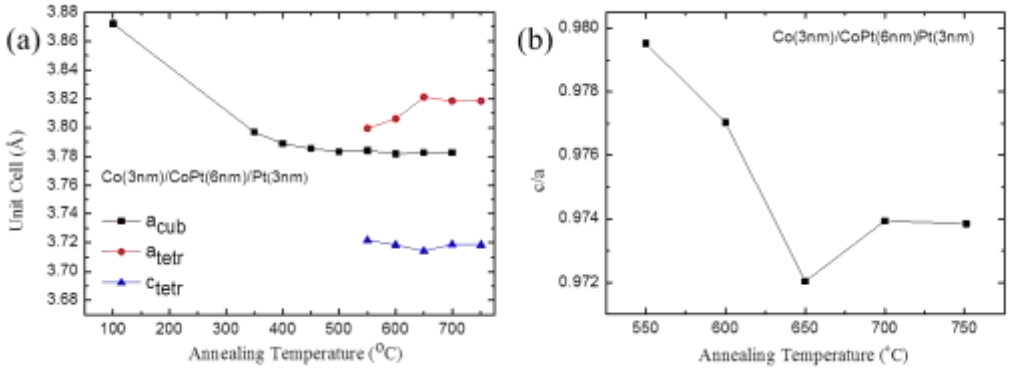

Figure 5.12: (a) Lattice constants variation of Co(3nm)/CoPt(3nm)/Pt(3nm) unit cell with annealing temperature, (b) c/a ratio values of bilayer.

Figure 5.13 summarizes the variation of c/a ratio values as function of annealing temperature for the single layer, bilayer and trilayers. A drastic reduction of the c/a ratio is observed at 650 ^{o}C for all samples. As smaller values of the c/a ratio indicate a higher degree of fct ordering, we can see that the ordering in CoPt single layer is lower in comparison to the Co/Pt bilayer and Co/CoPt/Pt trilayer. According to Vlasova and coworkers the lowest c/a ratio found is 0.972 for the CoPt alloy [159]. In our case both Co/Pt and Co/CoPt /Pt films have c/a=0.972, indicating that the chemical ordering is fully restored. In contrast, the lowest c/a ratio for the single layer is c/a=0.984. Thus, we may conclude that layering helps towards the achievement of a higher degree of chemical ordering.

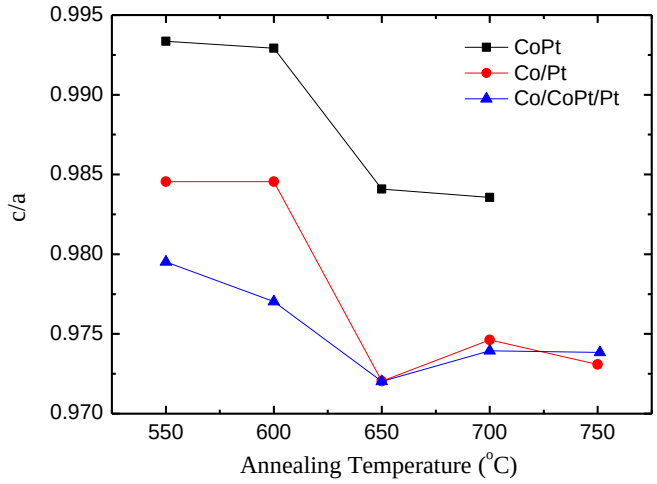

Figure 5.13: Variation of c/a values with annealing temperatures for the CoPt single layer, Co/Pt bilayer, Co/CoPt/Pt trilayer.

The variation of lattice constants a and c, in unit cells of CoPt single layer and Co/Pt bilayer, as a function of annealing temperature are shown in figure 5.14(a). The a_{cub} parameter of the CoPt single layer maintains in all annealing temperatures, pinpointing that the single layer is partially transformed in the tetragonal $L1_0$ structure. At annealing temperatures above 750 ^{o}C the fcc structure is reformed. In contrast, the bilayer is fully transformed to the tetragonal $L1_0$ structure at temperatures higher than 650 ^{o}C. The variation of the lattice constants a and c, in the Co/Pt bilayer and Co/CoPt/Pt trilayer samples, as a function of annealing temperature, are shown in figure 5.14(b). The

Co/CoPt/Pt a_{cub} parameter is constant up to 700 ^{o}C with annealing at higher temperatures resulting in full transformation to the $L1_0$ structure. The thicker Co/Pt bilayer is fully transformed to the fct phase at temperatures higher than 650 ^{o}C. It seems thin trilayer chemical ordering requires higher temperatures compared with the thicker bilayer. Toney and his coworkers have suggested that the chemical ordering is closely related with the film thickness as thin films suffer from an absence of nucleation sites; with a given concentration of nucleation sites a thinner layer will have fewer [160].

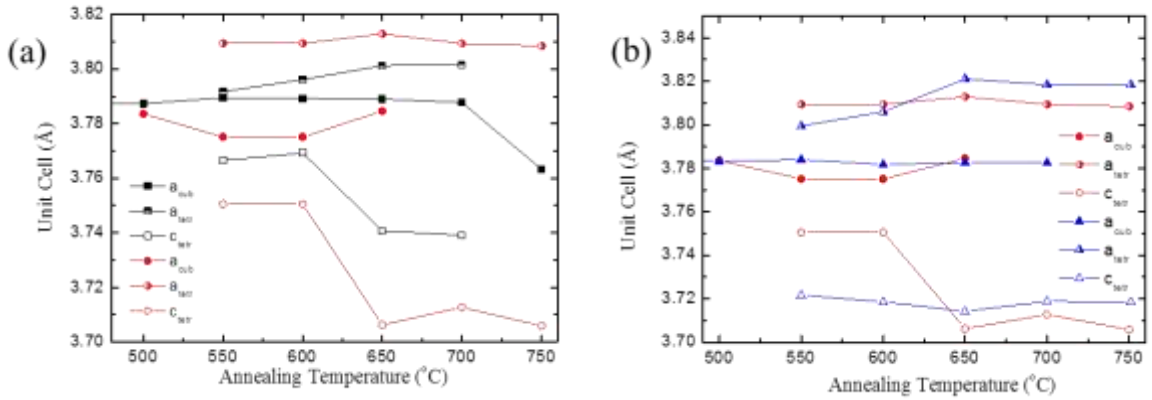

Figure 5.14: Comparison of lattice parameters variation between (a) CoPt single layer and Co/Pt bilayer, (b) Co/Pt bilayer and Co(3nm)/CoPt(3nm)/Pt(3nm) trilayer.

5.4 Structural and Morphological Study of CoPt Single Layer and Co//CoPt/Pt Trilayer with TEM

Structural information on the effect of layering can be obtained from the TEM images. A CoPt(39nm) single layer and a Co(9.5nm)/CoPt(19nm)/Pt(9.5nm) trilayer, heat treated at 750 ^{o}C for 30 minutes so as to form the tetragonal $L1_0$ structure, have been studied by TEM microscopy. In addition to the TEM images, selected area electron diffraction (SAED) data were also collected.

Figure 5.15 shows the SAED patterns of CoPt and Co/CoPt/Pt after annealing at 750 ^{o}C for 30 minutes. It is clear that the diffraction patterns of both samples show the fundamental (111) rings, as well as the superstructure (110) rings arising from the sample's tetragonality.

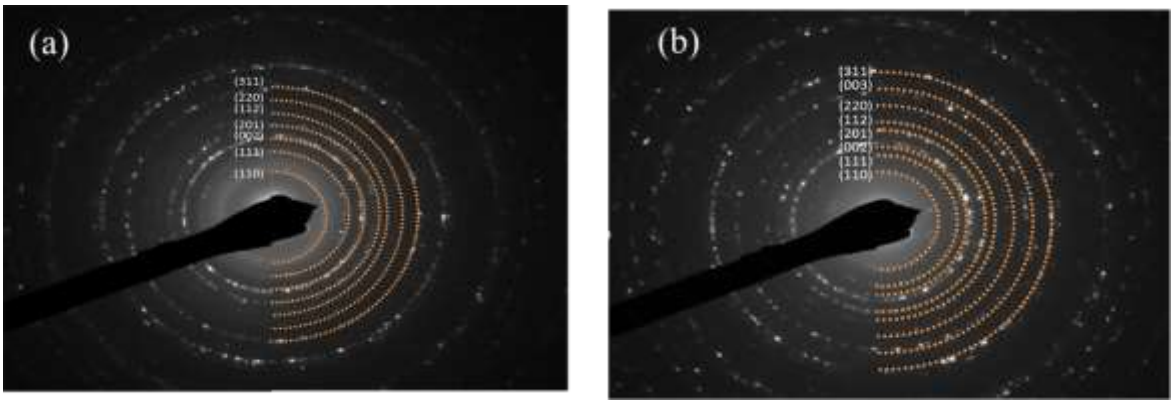

Figure 5.15: Selected area diffraction patterns of (a) CoPt (39nm) single layer and (b) Co(9nm)/CoPt(19nm)/Pt(9nm) trilayer.

The average CoPt grain sizes of are revealed in the bright field TEM image shown in figure 5.16 (a). The planar bright field image indicates random orientations of the grains. Many show parallel plates with differing contrast, indicating that a polytwinned microstructure is formed. The polytwinned microstructure is commonly found in chemically ordered alloys where a structural transformation takes place. The polytwinned microstructure was observed first by Kurmakov et al [161] in the chemically ordered CuAu alloy. Pashley and Presland [162] studied CuAu alloy with electron diffraction and found that these plates are twins and their crystal planes belong to the {101} family. Hibayashi and Weissman [163] confirmed the above and suggested that the twins are formed from strains that are developed during chemical ordering. By analyzing one hundred particles of figure 5.16(a) we found that the average grain size of is D_{CoPt}=32±12 nm. The bright field TEM image and the average size of CoPt grains in the Co/CoPt/Pt trilayer sample are shown in figure 5.16(b). The planar bright field image again shows grains with random orientation. The twin density here is larger compared to the CoPt single layer. By analyzing one hundrded particles the average grain size of was found to be $D_{Co/CoP/Ptt}$=42±12 nm.

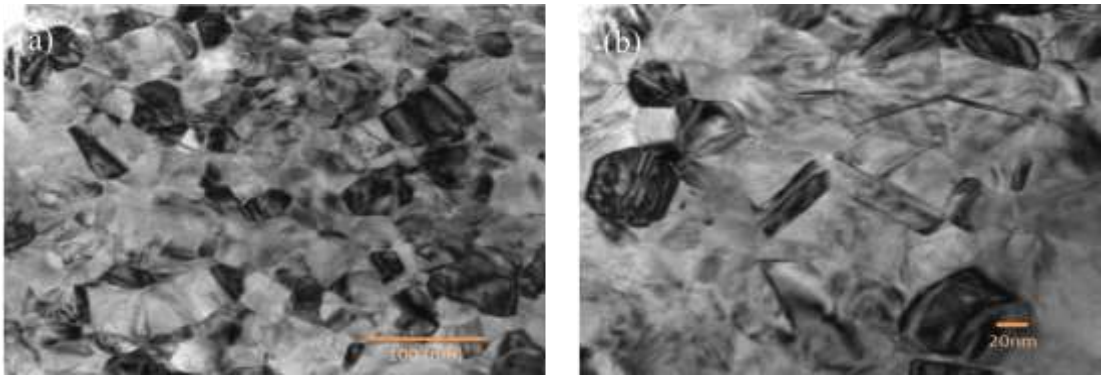

Figure 5.16: Planar bright field images of (a) CoPt single layer and Co/CoPt/Pt trilayer.

5.5 Conclusions

In summary, the effects of layering and thickness were studied in $CrPt_3$ and CoPt films. Trilayer $CrPt_3$ films show (111) texture and achieve a higher degree of ordering compared with co-deposited films. Furthermore, trilayers have larger coercivities than films co-deposited at all temperatures

The TEM study of Co-Pt films reveals that the twin density in trilayers is larger compared with the CoPt single layer. The average size of grains in CoPt single layers are 32nm, while the average size of Co/CoPt/Pt trilayers is 42nm. The larger grain size and density twins can be attributed to faster nucleation (lower annealing temperature), but from fewer nucleation sites in the case of trilayer, which may correspond to the point, where the composition is more favorable. In CoPt film the fcc phase is present at all annealing temperatures, suggesting the partially transformation from A1 to $L1_0$ structure. The Co/Pt bilayer is fully transformed to the $L1_0$ structure at 700 ^oC while the thin trilayer is fully transformed at 750 ^oC.

CHAPTER 6

6. The Effect of Magnetic Annealing in the Magnetic and Structural Properties of $L1_0$-Co/Pt Multilayers

As noted earlier, in the chemically ordered equiatomic CoPt phases, Co and Pt occupy alternating atomic planes along the c axis of the tetragonal $L1_0$ unit cell which is the magnetic easy axis. $L1_0$ is thermodynamically the low temperature phase, but due to kinetic limitations it is obtained by annealing of the disordered A1 (fcc) phase. During this annealing it has been found that a magnetic field (5 to 100 kOe) is effective, especially in the early stages of the A1→$L1_0$ ordering process, for the selective formation of a particular c-axis orientation [164]. Textural anisotropy with the c-axis alignment normal to the film plane, can be achieved in films epitaxially grown on MgO [165]. Sputtered polycrystalline CoPt films tend to grow with a (111) texture i.e. having the easy axis distributed on a cone with an angle of 54.70^o to the film normal. Different degrees of (001) texture have been achieved with the use of Ag [166,167,168], Au [169], B_2O_3 [170] and ZrO_2 [171] layers, under specific heat-treatment conditions and within thickness limitations, on which the texture shows very sensitive dependence. Similarly for FePt high magnetic fields can enhance crystallographic texture of cold-deformed nanostructured magnets made by cyclic sheath cold rolling and subsequent magnetic annealing [172]. These results are of interest as most applications require a specific crystallographic texture. In nanostructured FePt/B_2O_3 films the texture is found to depend mainly on the cooling rate and can be achieved both in zero and 100kOe field [173]. Hard magnetic film applications range from information storage media (where the challenge is to satisfy the conflicting requirements of high density, thermal stability and writability) to magnetic microelectromechanical systems where the aim is to provide high power at reduced dimensions [174]. The required film thickness depends on the application at hand. For instance magnetic recording media require thickness of the order of 10nm, while in contrast permanent magnets for micro-electromechanical systems require micron thick films.

In thin films surface energy anisotropy and elastic strain are very important factors determining texture. Thus even lower magnetic fields may be effective if they act in synergy with the former factors while on the other hand may be inefficient if they contradict them. Magnetic annealing was also found to introduce finer, less angular and more homogeneously distributed grains in soft and hard nanocomposites [172].

In this chapter a systematic X-ray diffraction (XRD) and Transmission Electron Microscopy (TEM) investigation on $L1_0$ CoPt films of different total thickness (17-68 nm) shall be presented. The films are obtained by annealing samples with different types of layering; from $(Co/Pt)_2$ bilayers to $(Co/Pt)_{16}$ multilayers. In order to study the underlying texture formation mechanisms, the thickness values explored here are both below and above the critical value (relaxation of film) for a plane-stress condition to hold.

6.1 Experimental Details

CoPt films with thickness $t = 17$nm, 34nm and 68nm have been prepared by heat treating $[\mathrm{Co}(\frac{t}{2n}nm)/\mathrm{Pt}(\frac{t}{2n}nm)]_n$ multilayer films. These have been deposited by magnetron sputtering on oxidized silicon wafers at RT using a MANTIS deposition system with the Co(3") and Pt(2") sources in confocal geometry. The substrates are rotated during the deposition. Prior to deposition the chamber is evacuated to a base pressure of 7×10^{-7}Torr. The process gas (Ar 5N) pressure was 2.5mTorr. The stoichiometry of the CoPt alloy films was found to be $Co_{54}Pt_{46}$ by EDX. The Co layers have been deposited at a rate of 0.46Å/sec applying 65W DC, and the Pt layers at a rate of 0.47Å/sec applying 120W RF. The samples were sealed in evacuated quartz tubes and heat-treated in a magnetic field of 1 kOe following a two stage heat treatment at 450 ^{o}C for 120 minutes followed by 750 ^{o}C for 30 minutes. Each profile was tried both with the applied field in-plane (//) and perpendicular to the film plane (⊥). The samples have also been heat-treated in zero field (ZF) as a reference. X-ray diffraction (XRD) θ-2θ diagrams were collected with a Bruker D8 Advance Diffractometer using $CuKa_1$ (λ=1.5418Å) and a secondary graphite monochromator. TEM observation was carried out by employing JEOL 3010 TEM and Philips CM20 200kV analytical electron microscopes. Plane view samples were prepared by single side polishing and ion milling, and the cross-section samples consist of a

sandwich structure were prepared by conventional lapping and polishing techniques followed by ion milling.

6.2 Magnetic Characterization of $L1_0$-CoPt Films

Typical in-plane and out-of-plane magnetic hysteresis curves for the Co/Pt bilayers two-stage annealed under a perpendicularly applied field are shown in figure 6.1. Comparison between the loops measured with the applied field perpendicular (⊥) and in the film plane (//) show a clear perpendicular anisotropy, as the loops are hard to saturate in the film plane. The increased in-plane coercivity can be attributed to pinning mechanisms. However, the exact angular dependence matches neither the Kondorsky $1/\cos\theta$ law nor its generalizations [175].

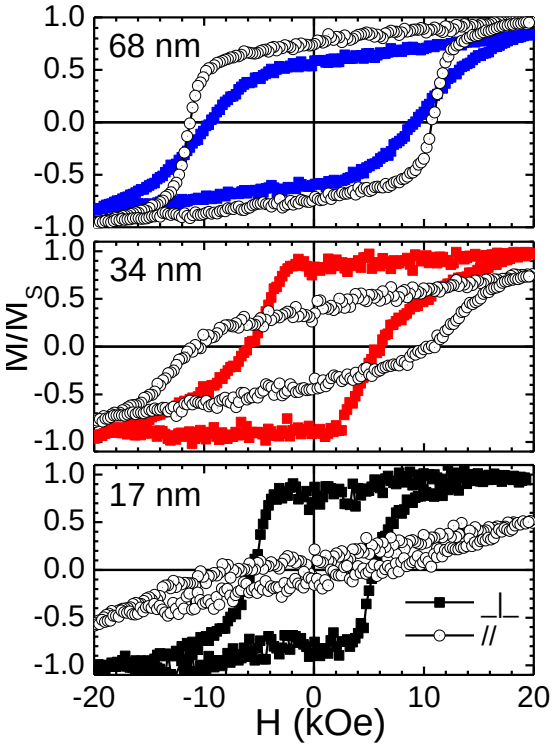

Figure 6.1: Normalized magnetization hysteresis loops obtained by heat-treatment of Co/Pt bilayers under a perpendicularly applied field H=1kOe. Solid squares: measuring field perpendicular (⊥) to the film plane. Open circles: in the film plane (//).

6.3 Structural Characterization of $L1_0$-Co/Pt Multilayers with XRD, 4-Circle XRD and TEM

XRD patterns for the 17nm, 34nm and 68nm bilayer films heat-treated under a perpendicular field are compared with the ZF heat-treated in figure 6.2. In all cases the magnetic field improves the (001) texture, but for 68nm thick films (111) texture predominates and the (001) enhancement is only marginal. The 17 nm samples show an appreciable (001) texture even without magnetic field, whereas in 34nm samples (001) texture is obtained only as a result of magnetic field annealing, but for both samples. The (001) texture is greatly improved in comparison to the ZF annealed samples. These observations show that the magnetic field is not sufficient to promote the (001) texture if other contradicting factors are present.

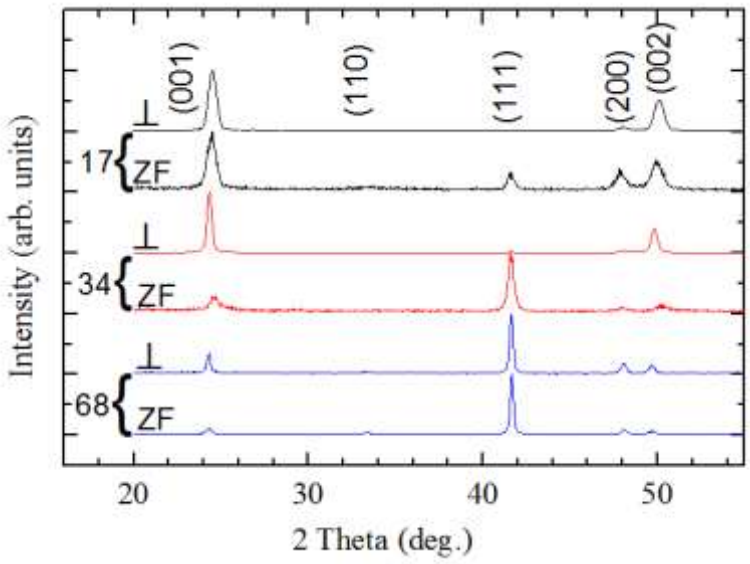

Figure 6.2: XRD patterns for the 17nm, 34nm and 68nm bilayer films heat-treated under a perpendicular field (⊥) compared to those heat-treated under zero field (ZF).

The XRD pattern analysis was done using three components with texture along the (001), (100) and (111) directions according to Ref [176]. Weak or non-existing (110) reflections, even in films with mixed texture, show that the texture cannot be described by

a continuous distribution around the preferred orientation (as in powder samples) but rather by the co-existence of different components. Other indications are provided by the fact of the a and c lattice constants calculated for the (001), (002) and (200) reflections do not match the d spacing of the (111) reflection and by the narrow angular distributions found in pole figures of all textures (dominant and secondary). The pole figures showing the distribution of the (001) and (111) grains for the two limiting cases of the 17nm and 68nm films are shown in figure 6.3. For the 17nm film the halfwidth of the distribution is 2.7deg. for both (001) and (111) textures. The ring (111) of poles at 55deg. is consistent with the angle between (111) the dominant (001) texture. For the 68nm sample the halfwidths of the main components are about 7 deg.

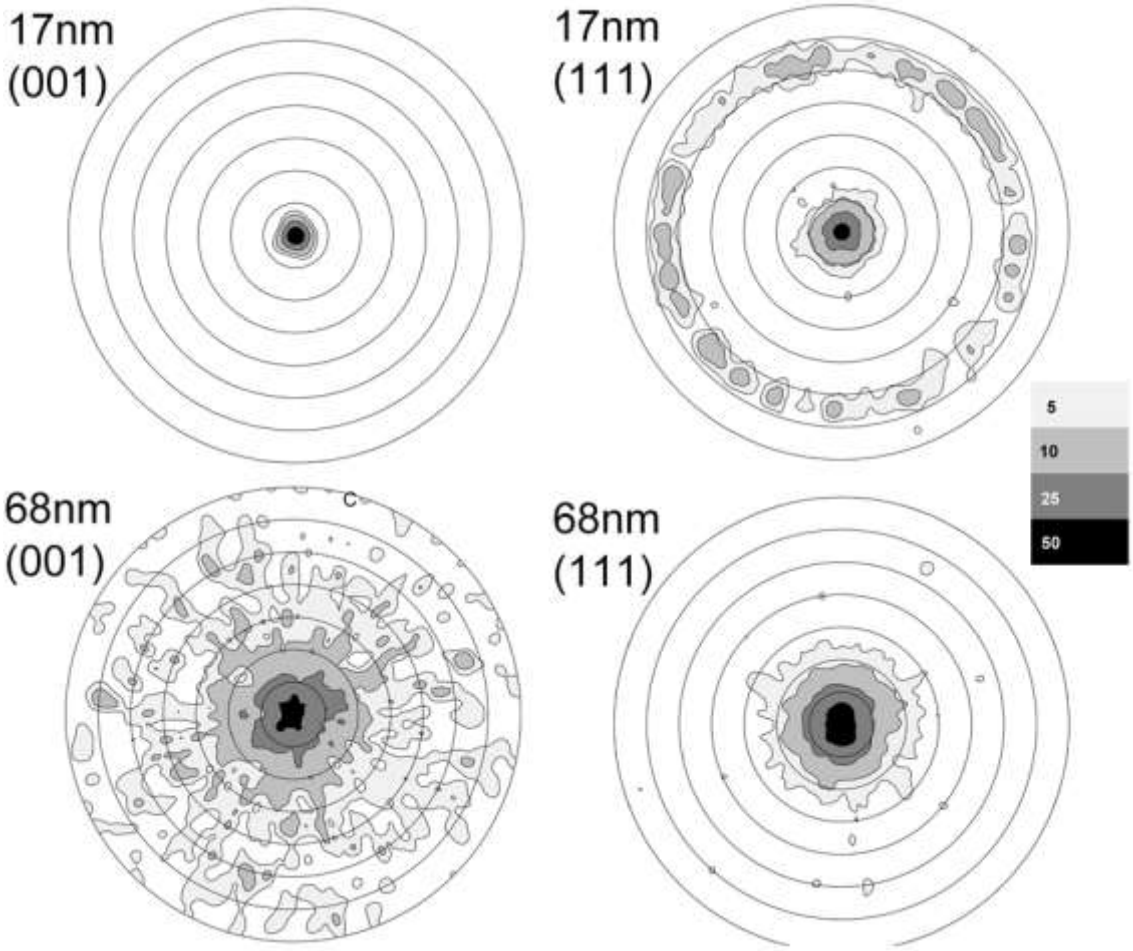

Figure 6.3: Pole figures of the (001) (left panels) and (111) reflections (right panels) for the 17nm (top panels) and 68nm (bottom panels) bilayer films heat-treated under a perpendicular field. The scale bar colors indicate percentage of maximum intensity.

The fraction of the (001) texture for samples with different initial layering annealed under different applied-field directions is summarized in figure 6.4. A perpendicular field promotes (001) texture. However an in-plane field cannot promote the (100) texture by the same token. Instead the fraction of (100) texture is always below 25% and (001) and (111) remains the main components in all cases. A (001) texture is obtained for the 34nm films even under an in-plane field.

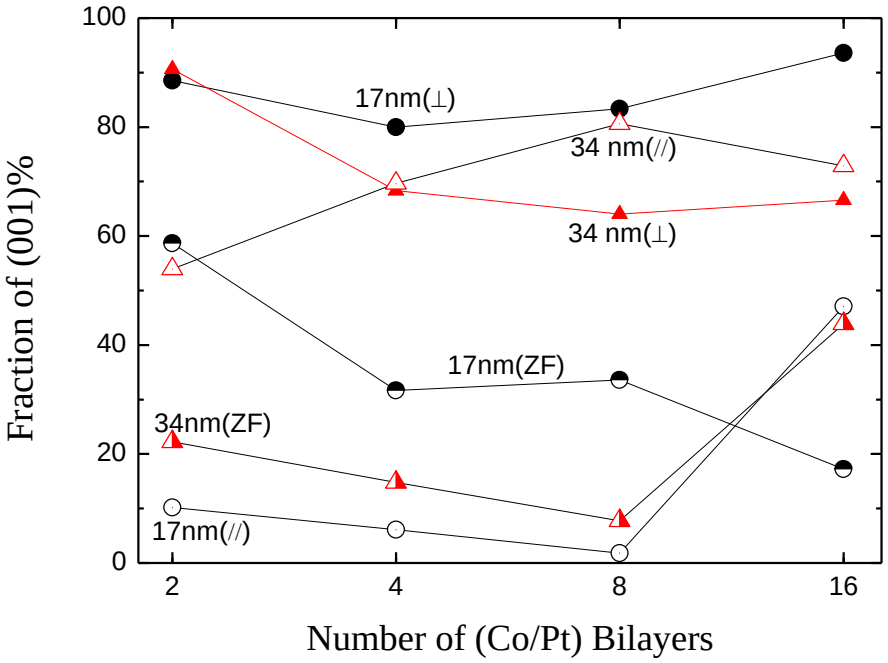

Figure 6.4: Fraction of the (001) texture in CoPt samples with different total thickness (17nm: circles, 34nm: triangles) obtained by heat-treating under different applied-field directions multilayers (solid symbols: perpendicular field ⊥, open symbols: in plane field, half symbols: zero field) consisting of different number of (Co/Pt) bilayers.

TEM microscopy was performed on selected samples to elucidate several crucial points. In figure 6.5 plane view bright field TEM images of magnetically heat treated samples of different thickness are compared. From these images the lateral grain size is obtained. The 17 nm sample is discontinuous in some areas and consists of large grains, some of which are close to 400nm. Smaller grains 50-100nm also exist, but represent a small volume fraction of the sample. This bimodal grain size distribution is typical of thin films [131]. The average size is 160nm with a 90nm standard deviation (SD). According to

cross sectional TEM, there is layer thickness variation, as plate-like and globular grains are present simultaneously. The 34nm sample also consists mainly of large grains, some very large (~400nm) and a smaller volume fraction of small grains with average garin size 140nm (SD=90nm). In contrast the thickest (68nm) sample is continuous and consists of a more homogeneous microstructure with 90nm average grain size (SD=35nm). In comparison the conventionally annealed sample does not contain grains larger than 250nm and has a larger fraction of small grains, 90nm with SD=45nm.

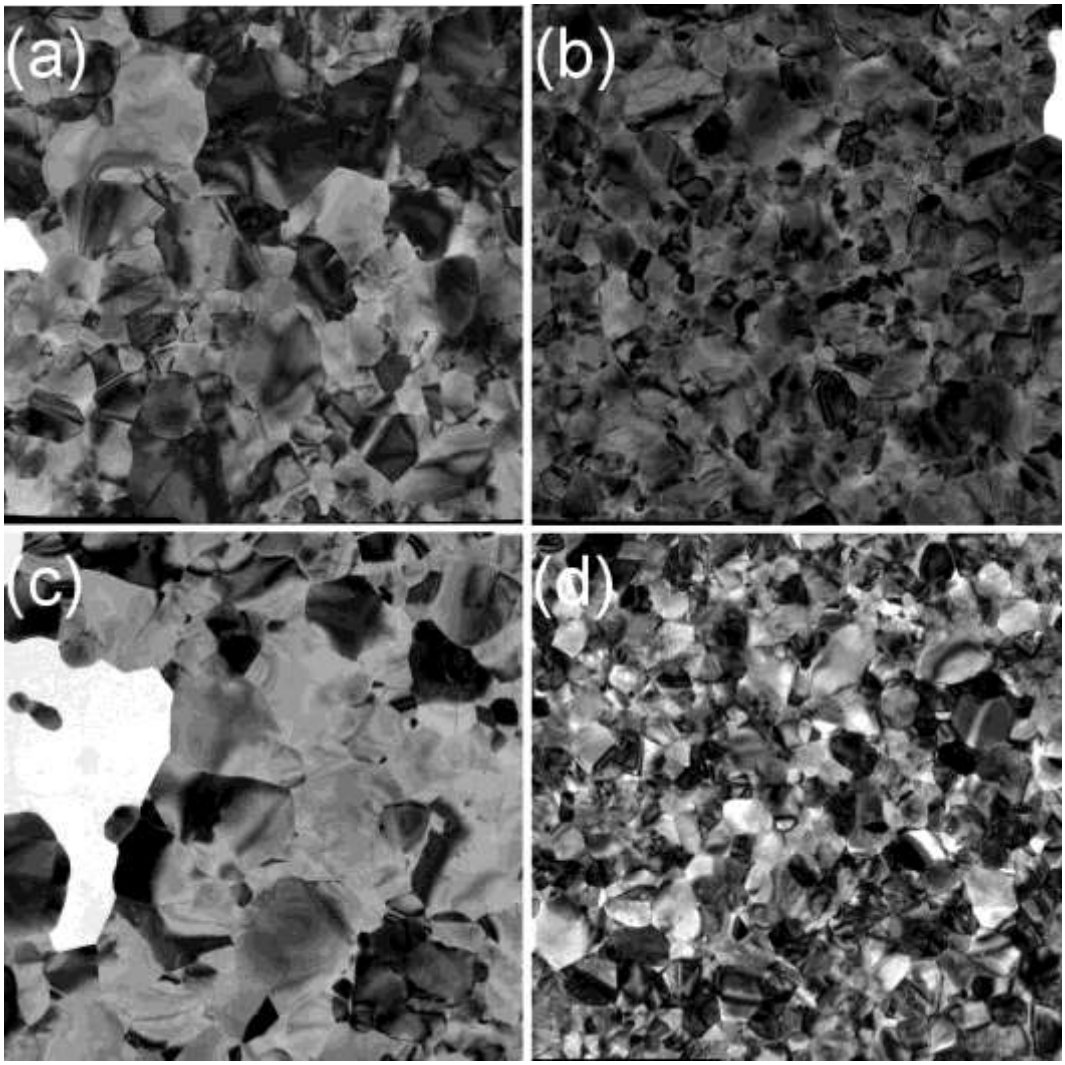

Figure 6.5: Plane view bright field TEM images of CoPt film samples. The square areas are $1500\times1500nm^2$. Magnetically heat treated: (a) 34nm thick, (c) 17nm thick, (d) 68nm thick. Zero field heat-treated (b) 34nm thick.

The observed microstructures are columnar and in most cases the grains span the whole film thickness even for the 68nm films (figure 6.6).

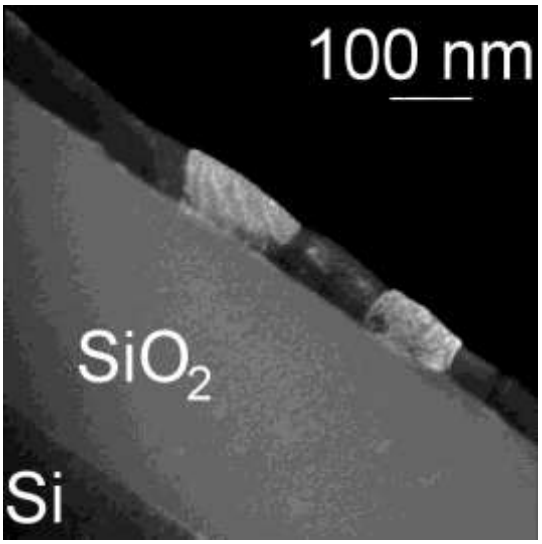

Figure 6.6: Cross-sectional dark field TEM image of a 68nm thick CoPt film sample.

EDX shows that all the samples have the same slightly Pt-rich stoichiometry and exhibit the tetragonal CoPt L10 phase. The tetragonality c/a ratios are in general agreement with the value of 0.9732 given in the JCPDS database. The fact that the experimental values appear a little lower may be related to strains (discussed in the next section). Texture analysis of the selected area electron diffraction (SAED) radial intensity distribution was carried out using Process Diffraction software. The area percentages of [001] and [111] texture are given in Table 6.1; the remaining percentage corresponding to [100] texture is in agreement with the XRD results in the following section.

Table 6.1: Summary of TEM analysis.

Thickness (nm)	Magnetic Annealing	Lateral Size $(\bar{d} \pm \sigma)$nm	Stoichiometry Pt/Co (at%)	Tetragonality c/a	[001] %	[111] %
17	Yes	175±60	57/43	0.963	98.6	-
34	Yes	160±75	56/44	0.969	73.0	22.7
34	No	95±30	56/44	0.966	44.6	38.3
68	Yes	95±25	57/43	0.971	39.9	39.9

Another interesting question concerns the effect of the first magnetic annealing step at (450 ^{o}C for 120 minutes) and why it promotes (001) texture even if the field is applied along the plane for the 34nm films. The TEM images and diffraction patterns of a 34nm film heat-treated at 450 ^{o}C with the applied field in the film plane are shown in figures 6.7(a) and 6.7(b). Let us note that in the XRD patterns of these samples only very broad {111} and {200} peaks appear and it is impossible to discern any sign of $L1_0$ formation. Similarly, the main characteristics of the (SAED) patterns show that the sample remains in the fcc phase with several crystal orientations coexisting (figure 6.7(a)). However, on close examination a few spots corresponding to superlattice {110} reflection can be found indicating that at least some grains are ordered. Furthermore if the differences between the radii of spots in the {311} ring are attributed to {311}-{113} splitting, a c/a ratio of 0.983 can be estimated. Similar conclusions can be drawn from the high resolution TEM (HRTEM) images of a 34nm thick CoPt film sample magnetically heat treated with an in-plane field shown in figure 6.7.

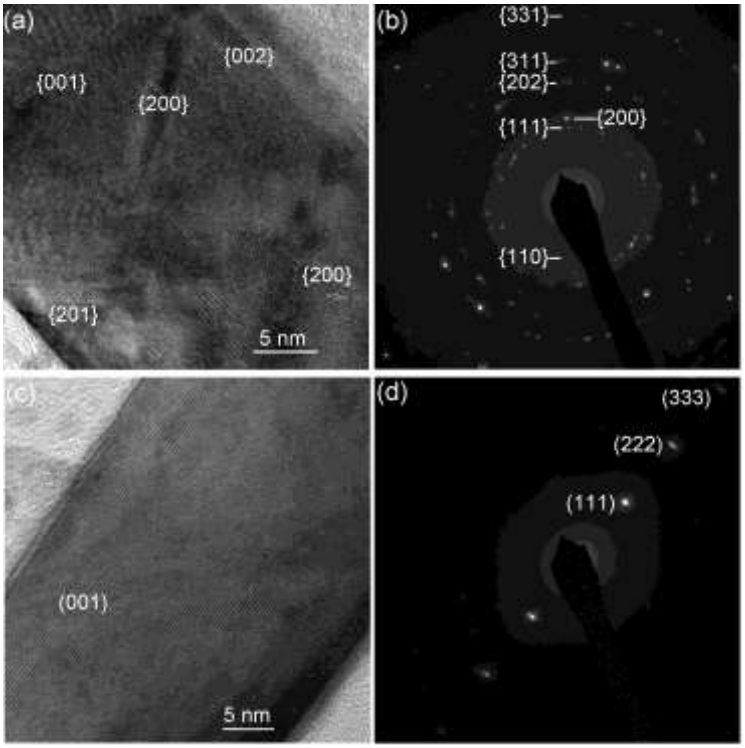

Figure 6.7: Cross-sectional TEM images (a,c) and Selected Area Diffraction Patterns (b,d) of a 34nm thick CoPt film sample magnetically heat treated with an in-plane field: Top panels (a,b) after the first annealing stage 450 ^{o}C for 120 minutes. Bottom panels: Additional 750 ^{o}C for 30 minutes.

Small grains with different crystallographic orientations coexist but no grains with a (111) orientation, favored by surface energy anisotropy, are observed. After the full heat-treatment (additional 750 ^{o}C for 30 minutes, see figure 6.7(c,d)), the grain size is greatly increased and the bigger grains show a preferred orientation. Thus it seems that $L1_0$ formation proceeds mainly in grains with the (001) texture at the expense of smaller grains of different orientations. The role of the magnetic field during this first stage is to hinder the growth of (111) grains which cannot be eliminated by a similar process. Since in the as-deposited films (with the A1 fcc structure) a large number of small grains are present the (001) grains are relatively rare. Thus the final (001) texture is characterized by a bimodal distribution with large (001) grains and smaller grains of different texture.

These results are in agreement with the model of strain energy driven selective grain growth for the (001) texture. In this case the texture does not originate from a specific crystallographic relationship but from the preferable (001) orientation during post-annealing [177]. The substrate's amorphous oxide layer minimizes the effect of the substrate lattice matching strains and allows for a biaxial in-plane strain. This model provides an explanation for the thickness limitations in obtaining the (001) texture i.e. in FePt thin films grown on amorphous substrates (001) texture is obtained when the film thickness does not exceed the grain height [178]. In this case the grain strain states are constrained by the substrate in the direction parallel to the film while ensuring minimal interaction in the direction perpendicular to the film plane. In view of these considerations it is interesting to analyze the strain states of the films. Unfortunately due to the high degree of texturing (of each component) it was not possible to estimate the residual stress state by the usual methods such as $\sin^2\psi$ plots [179].

The existence of different strain components is indicated by the fact that the a, c lattice constants calculated from the (001), (002) and (200) reflections are not consistent with the d-spacing of the (111) reflection. One cause of this may be that for typical θ-2θ diffractograms the scattering vector is always perpendicular to the film plane and thus different crystallographic axes are calculated based on different grains: the c-axis is derived from the (001) textured grains, the a-axis from the (100) textured ones and the d_{111} from the (111) textured. Interestingly this mismatch is larger for samples with a higher degree of (001) texture. This correlation of strain with texture can be quantified within the biaxial strain model using a stress free condition along the film normal as is widely used in stress/strain analysis of thin films [180]. Assuming a biaxial in-plane strain ε, using the

stiffness matrix independent elements $C_{11}, C_{12}, C_{13}, C_{33}, C_{44}, C_{66}$ appropriate for the tetragonal symmetry and following the methodology used in Ref. [179] we can express the strain $\varepsilon_{\perp}$ perpendicular to the film plane for different textures with the expressions given in Table 6.2.

Table 6.2: Perpendicular to in-plane strain ratios for films with tetragonal structure and (hkl) texture under biaxial in plane-stress. Numerical values for CoPt according to the data of Ref.[179].

hkl	$-\varepsilon_{\perp}/\varepsilon$
001	$\frac{2C_{13}}{C_{33}}$
100	$\frac{C_{12}+C_{13}}{C_{11}}$
111	$\frac{2C_{33}(C_{11}+C_{12}-C_{44})+4C_{13}(C_{44}+C_{66}-C_{13})-4C_{44}C_{66}}{C_{33}(C_{11}+C_{12}+C_{44}+2C_{66})+2C_{44}(C_{11}+C_{12}-2C_{13}+2C_{66})-2C_{13}^2}$

The values are calculated by substituting the elastic constants given in Ref. [181], in compliance matrix formulation. The difference between the values given in Table 6.2 shows that if the same biaxial in-plane strain ε is assumed, crystallites with different textures will be strained in the direction perpendicular to the film plane to a different degree with respect to their equilibrium values (indicated by the zero subscripts):

$$\begin{aligned} a &= a_0(1-1.15\cdot\varepsilon) \\ c &= c_0(1-1.13\cdot\varepsilon) \\ d &= d_0(1-0.65\cdot\varepsilon) \end{aligned} \tag{6.1}$$

,where we have denoted the d-spacing of (111) with d for simplicity. Thus the observed d-spacing values s from θ-2θ diffraction patterns seem inconsistent. If we assume that for the equilibrium values the correct relationship $1/d_0^2 = 2/a_0^2 + 1/c_0^2$ holds and use $(1+x)^{-2} \approx 1-2x$ we can see that the mismatch is proportional to the biaxial strain.

$$\frac{1}{d^2}-\frac{2}{a^2}-\frac{1}{c^2}=-\varepsilon\left(\frac{3.296}{a_0^2}+\frac{0.954}{c_0^2}\right) \tag{6.2}$$

The values of ε calculated by equation 6.2 are plotted against the degree of (001) texture in figure 6.8. The left side of equation 6.2 turns out to be negative, yielding positive (tensile) biaxial in-plane strain values. The data indicate a correlation between the biaxial strain and (001) texture only for the samples annealed in a field while for the films annealed in zero fields the data appear scattered. We note that the correlation between the lattice constant inconsistency and the degree of texture is independent of the assumptions used to derive equation 6.2, which is used merely to quantify the data. However, biaxial strain states are usual in thin films, especially in heat-treated ones due to the different thermal expansion coefficients of the film and the substrate. In particular for $L1_0$ it has been proven that tensile biaxial strain favors (001) texture [177], since it is consistent with the change of the unit cell during the cubic to tetragonal transformation only if the c-axis is perpendicular to the substrate.

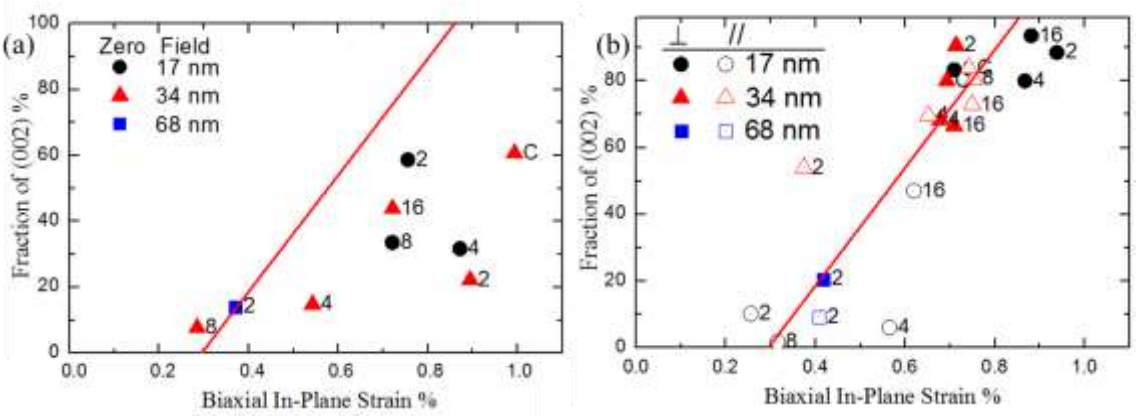

Figure 6.8: Correlation between the fraction of (001) texture as a function of biaxial-in plane strain. (a) Zero field heat-treated samples and (b) films heat-treated under a perpendicular (solid symbols) and in-plane (open symbols) fields. Different thicknesses are symbolized as follows: 17nm circles, 34nm triangles and 68nm squares. The line (exactly the same in both panels) is a guide to the eye

.

6.4 Conclusions

In summary the effect of magnetic annealing on the texture was investigated in a series of CoPt films of different thicknesses obtained by annealing Co/Pt multilayers. An applied magnetic field is found to promote the (001) texture in synergy with existing biaxial strain. The fact that (111) texture appears in thicker films is inconsistent with a surface anisotropy mechanism, which would favor (111) for thinner films. Thus it seems the transformation strain may be the main factor determining texture. A plausible reason is that the $L1_0$ ordering transformation from the fcc A1 structure to a tetragonal one is consistent with a tensile in-plane strain in crystals with c-axis perpendicular to the film plane. Thus, the occurrence of anisotropic strain, due to an ordering transformation, favors (001) texture [177]. In accordance with this model, (001) texture cannot be obtained for the 68 nm samples, since these films are not sufficiently thin for a plane-stress condition to hold. The (100), (010), and (001) variants of the A1 structure are easily amenable to (001) of $L1_0$. Thus in some cases even an in-plane field can lead finally to a (001) texture. One the other hand surface energy anisotropy favors (111) growth in the fcc as-deposited state and the initial (111) seeds cannot recrystallize to (001). In short the (001) texture proceeds by transformation-driven selective grain growth of (001) at expense of the other possible textures. The correlation between strain and texture is clear only for magnetically annealed samples. Thus we may conclude that during the selective (001) grain growth the effect of the field is, apart from driving the formation of easy axis (001) along its application direction, mainly to correlate local strains at a macroscopic level thus increasing their effect.

CHAPTER 7

7. $L1_0$-FePt Nanoislands Obtained by Polystyrene Sphere Array Masks

In this chapter a study of triangular FePt nano-islands prepared by sputtering using regular single-layer arrays of nanospheres (173nm) and microspheres (978nm), as deposition masks is presented. Their morphological, structural, and magnetic characterization, focused on the assessment of magnetic switching processes and interparticle interactions is presented, and the results are compared using micromagnetic simulations.

7.1 Experimental Details

The self-assembly of a nanosphere polystyrene monolayer has been described in paragraph 4.2 (figure 7.1(a)). Fe/Pt bilayer films with a total thickness of 36 nm were deposited on the above nanosphere covered SiO_2 substrates by magnetron sputtering at room temperature using a MANTIS deposition system (figure 7.1(b)). The two layers were sequentially deposited by Fe(3") and Pt(2") sources. Prior to the deposition the chamber is evacuated to a base pressure of $7x10^{-7}$Torr and the process gas (Ar 5N) pressure was 2.5mTorr. The Fe layers were deposited at a rate of 0.1 Å/sec applying 100W RF and the Pt layers at a rate of 0.47Å/sec with 120W RF. After the deposition, the nanosphere layers are taped-off leaving arrays of triangular-like Fe/Pt islands (figure 7.1(c)). Apart from these nanoisland arrays continuous films were deposited as reference samples. The samples were sealed in evacuated quartz tubes and heat-treated at 500-650 ^oC for 15 minutes. The typical θ-2θ X-ray diffraction (XRD) and grazing incidence x-ray diffraction diagrams were collected with a Bruker D8 Advance Diffractometers using $CuKa_1$ (λ=1.5418Å). Film thicknesses were determined by X-ray reflectivity measurements. The magnetic measurements at room temperature were performed with a Lake Shore vibrating sample magnetometer (VSM). Low temperature hysteresis loops as well as the First Order

Reversal Curves (FORC) have been produced using data obtained on a MPMS-XL-7AC SQUID magnetometer (Quantum Design) for selected samples. Atomic Force (AFM) and Magnetic Force (MFM) images were obtained with an AutoProbe CP using hard magnetic Co alloy coated MFM probes (Bruker, High Peformance, MESP-RC).

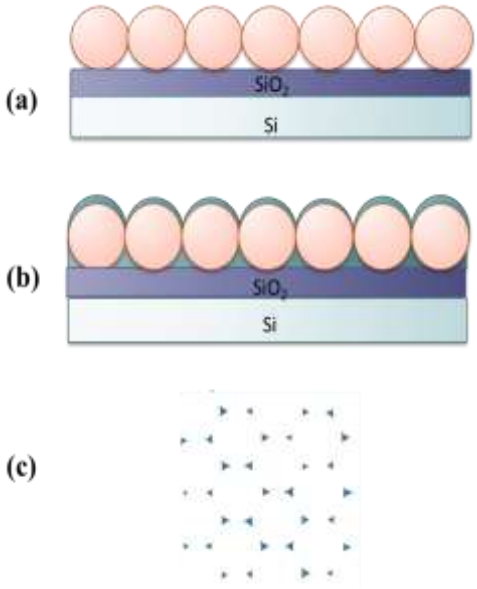

Figure 7.1: Schematic view of nanoislands deposition: (a) Monolayer of polystyrene nanospheres, (b) deposition of Fe/Pt bilayer onto nanospheres and (c) trianglular-like nanoislands after lift-off of nanospheres.

The measurements were done in non-contact mode after adjusting the height to the point where the topography signal disappears. Prior to the MFM studies the sample were brought to DC demagnetized state in an electromagnet. The images have been processed and analyzed with the Gwyddion 2.26 [182] and ImageJ 1.44p [183] programs.

7.2 Morphological Characterization of $L1_0$-FePt Nanoislands

Following the method described above, polystyrene sphere colloidal suspensions applied on appropriately prepared silicon wafer surface we yielded hexagonal 2D lattices of nanospheres with a long range structural coherence of the order of 10-20 sphere

diameters. At the edges of these structurally coherent areas imperfect close packing creates lines analogous to crystal grain boundaries [184,185]. After the sputter deposition of FePt and the removal of the polystyrene spheres we are left with regular arrays of islands (figure 7.2). These islands are triangular-like and, ideally would correspond to the curvilinear equilateral triangles that are defined by the empty areas left by a hexagonal 2D-array of close packed circles. Assuming a line-of-sight coverage with the atom flux perpendicular to the substrate, the area left between spheres of diameter D is $\left(\frac{\sqrt{3}}{4}-\frac{\pi}{8}\right)D^2$, which corresponds to an equilateral triangle of side $\sqrt{1-\frac{\pi}{2\sqrt{3}}}D \approx 0.305D$. In comparison, the largest inscribed equilateral triangle has a side of $\left(2-\sqrt{3}\right)D \approx 0.268D$ [46]. Accordingly, the size of the islands has been calculated as the side of the equilateral triangle that gives the same area, as determined from the images using the ImageJ software [183]. The values are very close to those obtained by the Feret size [186]. For the microspheres (978nm) the size of islands are (326±47) nm. This is equal to 0.34D of the microsphere diameter (figure 1(a),(c)). In the case of the nanospheres (173nm) the islands are (73±19)nm which is 0.42D of the nanosphere (figure 1.(b),(d)). Imperfect matching at the sphere array "grain boundaries" results in additional lines of deposited material. For brevity hereinafter we refer to them as the 330nm and 70nm island arrays.

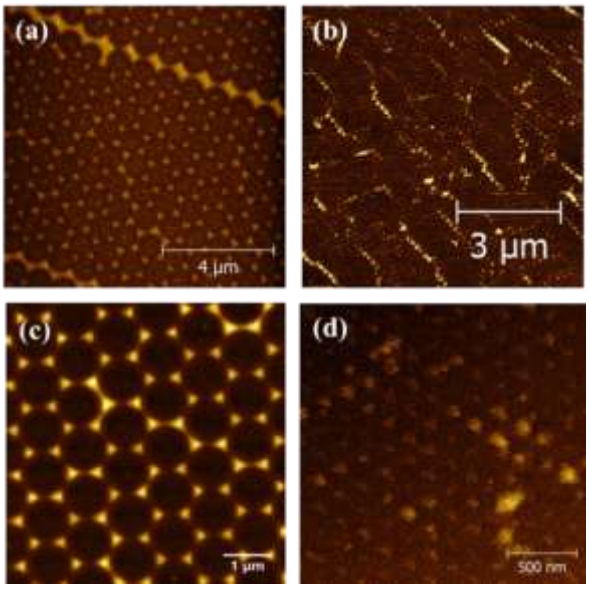

Figure 7.2: AFM images showing the (a), (c) 330nm and (b), (d)70 nm island arrays.

7.3 Structural Characterization of $L1_0$-FePt Nanoislands

The as-deposited films have the A1-fcc structure and are magnetically soft. Annealing at high temperatures is needed to obtain the high anisotropy tetragonal $L1_0$ phase. Figure 7.3 shows the grazing incidence X-ray diffraction pattern of a continuous film as well as the 70nm and 330nm samples annealed at 650 ^{o}C for 15 minutes. The background has been subtracted using the Bruker-AXS EVA software in order to facilitate the comparison. The GIXRD pattern of the continuous film clearly shows the formation of the $L1_0$, since the superstructure reflections (001) and (110) appear and the the A1 (200) splits into (002) and (200) peaks. In contrast, in the GIXRD patterns of the nanoislands (002) and (200) splitting is not clearly observed but the $L1_0$formation is evidenced by the (001) and (110) reflections. The conventional Bragg-Brentano scans (not shown here) indicate that the films are polycrystalline and randomly textured with a weak (111) preferential direction of crystallite growth, but in the case of the islands the count rate is extremely low, due to their low surface coverage (~10%).

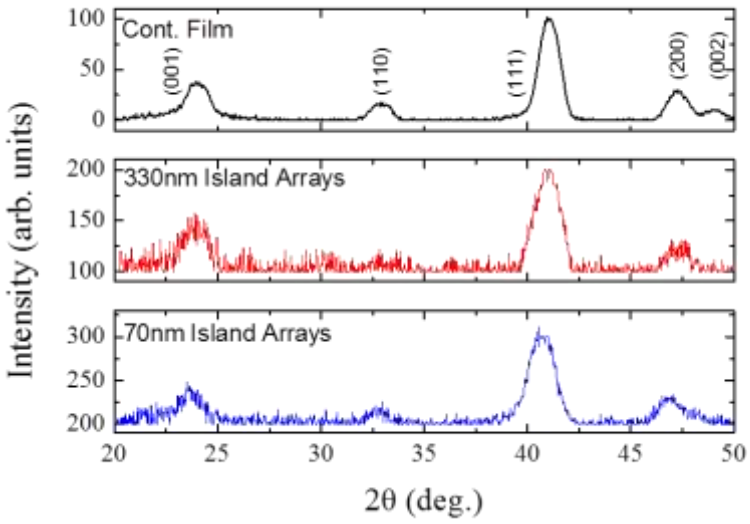

Figure 7.3: GIXRD patterns of FePt film and nanoisland arrays after heat-treatment at 650 ^{o}C for 15 minutes.

Figure 7.4 shows the c/a ratio values of all samples after heat treatment at different temperatures for 15 minutes. In all cases the c/a ratio is reduced (i.e. the tetragonality increases) with the annealing temperature. The minimal values of c/a ratio for the

continuous film, 330nm and 70nm island arrays is achieved at 650 ^{o}C and they are 0.960(±1), 0.969(±1), and 0.971(±1), respectively. For the bulk material the room temperature c/a value is 0.9636 while at higher temperatures values as low as 0.954 are reported, mainly due to shrinking of the Fe atomic volume [187]. The c/a ratio values are comparable to those reported for chemically synthesized FePt nanoparticles [188]. In continuous films lower c/a values than those of the bulk have been reported at room temperature [189]. This probably occurs as a result of the different degrees of strain between differently textured components [190].

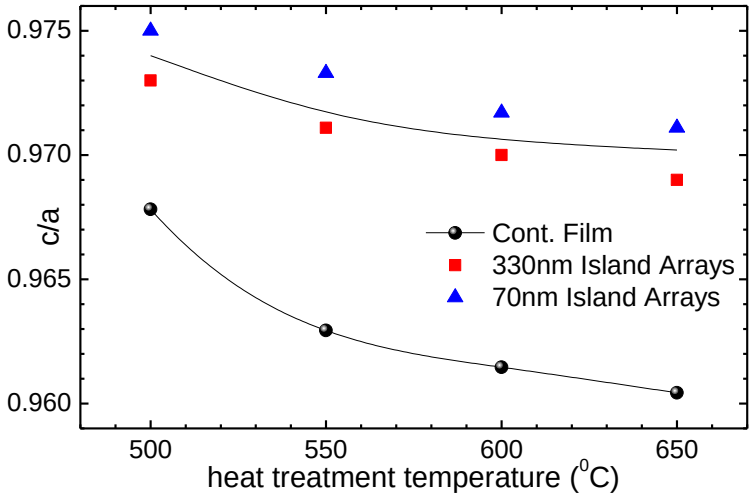

Figure 7.4: c/a ratio values of continuous films, 330nm and 70nm island arrays at different annealing temperatures.

7.4 Magnetic Characterization and FORC study of $L1_0$-FePt Nanoislands

The formation of the hard phase in nanoislands is also evident in the hysteresis loops. Typical in-plane hysteresis loops of samples annealed at 550 ^{o}C for 15 minutes are shown in figures 7.5(a) (measured at room temperature) and 7.5(b) (measured at10K). All samples are magnetically hard. At room temperature the coercivity of 330 nm island arrays is close to that of the continuous film (H_c=11kOe). In contrast, the 70nm island arrays show a shoulder in the demagnetization quadrant of the loop, a typical sign of the co-existence of a soft phase with the hard phase (H_c=8.5kOe). At 10K the H_c values are

14.8kOe and 12.2kOe for the continuous film and 70nm island arrays, respectively, comparable to reported values Ref. [188]. The ratio of room temperature values to those at 10K does not differ, indicating that the hard phase anisotropy is strong enough to suppress size effects.

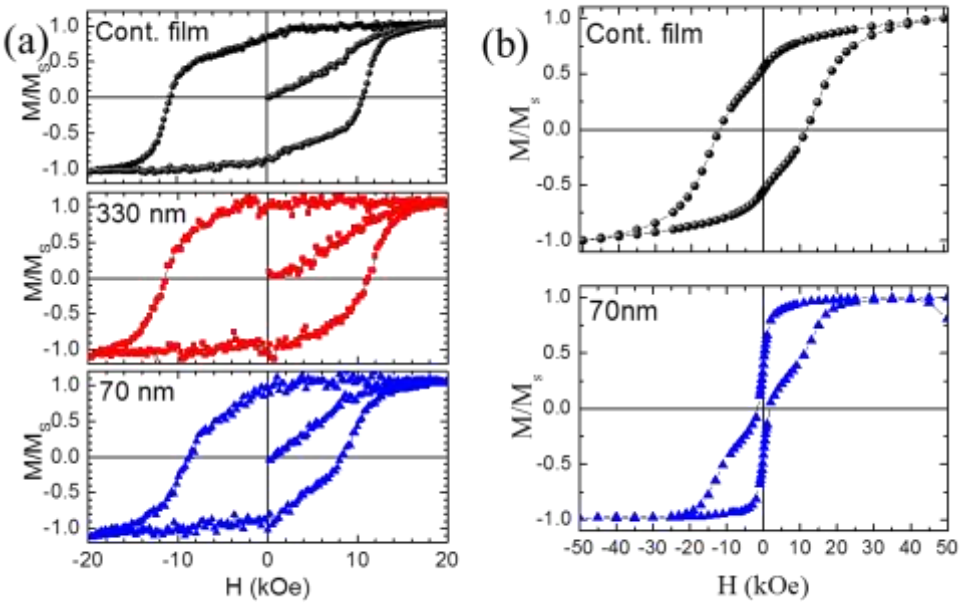

Figure 7.5: Magnetization hysteresis loops of continuous film, 330nm and 70nm island arrays annealed at 550 ^{o}C for 15 minutes at (a) room temperature and (b) 10K.

The co-existence of hard and soft phases could be simply attributed to the existence of nanoislands having low coercivity due to incomplete ordering. However, the multidomain structure of some of the islands in the MFM images (discussed below) and the strong deviation of the δM parameter (figure 7.6) from independent single domain particle behavior show that more complex mechanisms may be also involved. An assembly of non-interacting single domain particles should in principle result in zero δM [191]. The appearance of non-zero δM curves is a result of inter-element coupling and/or a multidomain state within elements [192]. Due to the presence of the soft phase, the nanoisland sample shows non-zero δM values even around zero field. In reality, this is a result of an incompletely demagnetized state, caused by the presence of the soft phase.

However, overall the interaction is weaker with maximum deviation ~40% compared to 60% of the continuous film.

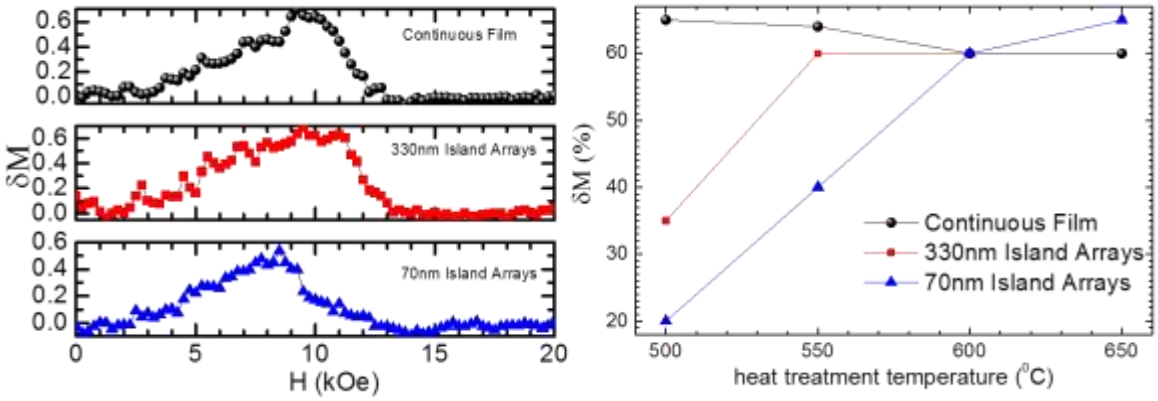

Figure 7.6: (a) Delta-M plots of continuous film, 330nm and 70nm island arrays annealed at 550 ^{o}C for 15 minutes and (b) delta-M values of all samples annealed at different temperatures.

First-order Reversal Curve (FORC) diagrams can be used to acquire a more thorough picture of the hysteretic behavior [116,193,194]. The results of the continuous film and 70nm island arrays after heat-treatment at 550 ^{o}C for 15 minutes are shown in figure 7.7. Figures 7.7(a) and 7.7(c) show typical families of magnetization curves used for the construction of the FORC plots; the magnetization axis is in arbitrary units. In brief, the FORC method analyzes families of magnetization curves in order to depict the irreversible switching processes on the coercivity-interaction plane (H_c, H_i). Strictly speaking this pair of parameters, originating from a Preisach model interpretation [195], is more meaningful when the reversal process can be described within the framework of an assembly of interacting magnetic entities, as localized reversal mechanisms such as nucleation and domain propagation complicate the interpretation of the interaction field. However, some clear differences can be observed. The continuous film FORC plot is characterized by a single peak corresponding to a hard phase with negligible average interaction. The H_c distribution is centered along the coercivity axis at H_c=10kOe with a halfwidth of ΔH_c=6kOe, and along the interaction axis at H_i=-0.06kOe with ΔH_i=8kOe. In contrast, the FORC diagram of the 70nm island arrays shows a strong contribution near the axes' origin (at H_c=0.49kOe, H_i=0.11kOe) which, being well separated from the hard phase distribution

centered at H_c=9.2kOe, ΔH_c=5kOe and H_i=-0.63kOe, ΔH_i =2.5kOe, is a clear sign of an uncoupled soft phase. Comparing the parameters, the most striking difference appears in the interaction fields: the hard phase of the continuous film has a much broader distribution of interaction fields but smaller average interaction field. In the case of the 70nm island arrays the limited size and the increased surface contribution make the existence of defects that may lead to a loss of coercivity more probable. The island's limited size reduces the probability of intergrain interactions and permits inhomogeneities to act as decoupled nucleation centers that can lead to magnetization reversal at low fields. Thus, the 70nm island arrays appear two phase, but with reduced interactions.

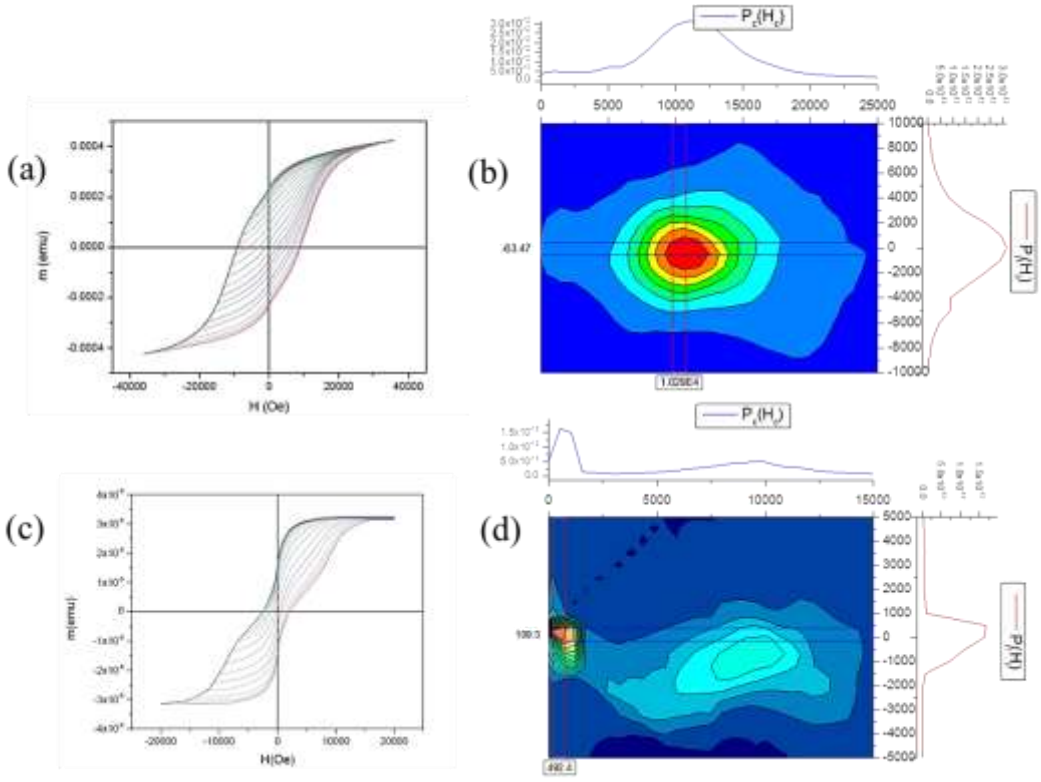

Figure 7.7: Typical families of magnetization curves used for the construction of FORC plots of the (a) continuous film and (c) 70nm island arrays. First Order Reversal Curve (FORC) distributions (b) top: a continuous film, (d) bottom: 70nm island arrays. The distributions shown above and to the left of the FORC diagrams represent the distributions $p(H_c)$ and $p(H_b)$ obtained by integrating out the Hb and Hc dependence within the width defined by the lines.

The coercivity and maximum δM value (figure 7.6(b)) for samples prepared under different heat-treatment are summarized in Table 7.1. The lowest δM is obtained for the 70nm island arrays annealed at 500 ^{o}C for 15minutes, but the δM values increase for higher heat-treatment temperatures. In general, the switching behavior deviates from the zero δM-plots expected for non-interacting single domain particles. Collective behavior of elements has been reported for lower anisotropy elements [196].

Table 7.1: Coercivity H_c (kOe) and maximum δM (%) values for $L1_0$-FePt continuous films, 330nm and 70nm island arrays annealed under different temperatures. In the case of 'two-phase' loops the H_c of the hard phase is given.

Annealing Temperature (^{o}C)	Property	Continuous Film (15min)	330nm islands (15min)	70nm islands (15min)
500	δM(%)	65	35	20
	H_C(kOe)	10.5	10.6	8.5
550	δM(%)	65	60	40
	H_C(kOe)	11.2	11.4	8.5
600	δM(%)	60	60	60
	H_C(kOe)	8.7	12.3	6.7
650	δM(%)	60	65	65
	H_C(kOe)	8.5	7.5	6.4

A simple calculation of the critical single domain size can be done by equating the expected gain in stray field energy $(1-a)\frac{1}{2}N\mu_0 M_S^2 V$ to the cost of domain wall energy γS formed [103]. In these formulas α is the reduction of stray field energy by the formation of a two-domain state (compared to that of a homogeneously magnetized one), N is the demagnetization factor, M_S the saturation magnetization, V the volume of the particle, γ the domain wall surface energy and S the area of a the wall that separates the particle into two domains. Assuming spherical particles (N=1/3, and α=0.4725) and the bulk parameters of FePt ($\mu_0 M_S = 1.43\text{T}, K = 6.6\times10^6\,\text{J/m}^3$) this gives a size of 340nm. A similar value of 310nm can be calculated for CoPt. Thus, it is not surprising that a slightly higher coercivity was obtained for the 330nm island arrays (Table 7.1). However, the geometrical factors that are involved in these calculations will differ for particles of different shapes.

Especially in the case of triangular elements a homogeneously magnetized state is difficult to attain as strong demagnetizing fields occur at the corners, which may also influence the magnetization reversal. Experimentally, high resolution magnetic force microscopy of patterned $L1_0$-FePt triangular dot arrays by nanosphere lithography showed a mixture of single domain and double domain states, which indicates that the critical single domain size is about 90nm [52]. In perpendicular anisotropy CoPt dot-arrays with diameters ranging 80 to 1000nm fabricated using electron beam lithography and reactive ion etching, the 80 nm diameter dots were characterized as single domain by MFM. Lower anisotropy $(Co/Pt)_{25}$ multilayer dots show a transition from multidomain to single domain behavior as the size is reduced from 220nm to 100nm [197]. On the other hand, in a comparative study of the magnetization reversal behavior of nanostructured $L1_0$-FePt, Co/Pt multilayer (ML), and CoPt/Ru dots [198], the critical size for the bi-stability of $L1_0$-FePt was found to be 60 nm. It was reported that the magnetization reversal proceeds via domain wall displacement even for such a small dot size while in the other materials, the bi-stable state is maintained over a very wide size range up to several hundred nm, and the magnetization reversal is dominated by theucleation. This difference in reversal behavior has been attributed to the difference in structural inhomogeneity, such as defects.

MFM images are shown in figure 7.8. The images have been obtained in the DC demagnetized state (i.e. saturation and application of a reversed field that yields zero remanence). In accordance with the δM-plots the MFM images do not indicate a single domain state, but many of the triangles show contrast patterns more complex than that of a simple dipole field [52].

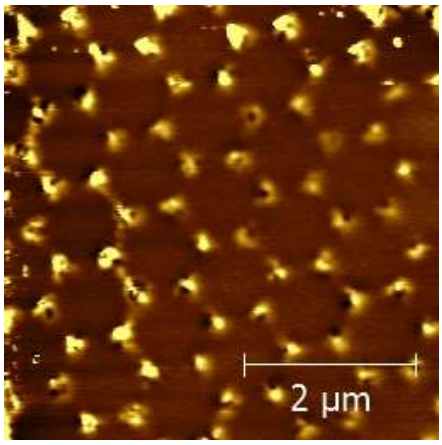

Figure 7.8: MFM image of 330nm island arrays.

In order to clarify this we have performed micromagnetic calculations using the Magpar open source micromagnetic finite element package [199]. The sample was described as two prisms of 36nm in height with equilateral triangles bases of 330nm, with 5 nm distance between their closest points. The finite element mesh considered had a 5nm maximum distance between nodes, a value which is close enough to the 3.5 nm value of the exchange length so we can assume that the discretization artifacts are negligible. The material parameters were chosen similar to those of bulk FePt with a saturation polarization of $\mu_o M_s$=1.43T and an exchange constant A=11pJ/m, which has been found to be independent of the degree of ordering [200]. In order to match the experimentally observed coercivity, a magnetocrystalline anisotropy constant of $K=1.4x10^6$ J/m^3 had to be assumed, while the easy axis direction was considered to lie along one of the diagonals of the coordinate system, tilted at 45° with respect to the sample plane (figure 7.9(a)). In a first approach, we aconsidered each prism as a single crystal, with homogenous easy axis orientation throughout the island, but oriented along different diagonals from one island to another. The external magnetic field was applied in the sample'plane. In order to study the effect of the field orientation relative to the easy axes we have chosen two different directions for the external field, marked as H_1 and H_2 in figure 7.9(a). Firstly, the field H_1 was applied on a symmetry axis, making the same angle of 54.7° with all the possible easy axes orientation while in the second case the direction of the field was at a 45° angle toH_1, making angles of 45° with two of the possible easy axes directions and 90° with the other two directions. We observed that in single-grain islands the reversal is collective, taking place by propagation of a domain wall starting from one corner. The magnetostatic interactions between islands are not strong enough to produce interaction domain effects at the K value used, but only for lower values that correspond to a soft phase. Only significantly lower values close to $K=10^5$ J/m^3, can give rise to vortex equilibrium states.

On a second approach, we have employed the same geometry but divided each island in four crystalline grains, assuming different easy axes direction within the same island. The grains inside the each island were coupled by exchange interactions. In this case we have observed that different switching patterns occur (figure 7.9(a)) and induce an important decrease of the total coercive field even if the field makes the same angle with all the easy axes directions (figure 7.9(b)). Moreover, when the field is not on a symmetry axis with respect to the easy axes directions, the grains oriented at higher angle values switch first and, by coupling, induce switching of the other grains lowering the coercive

field even further. Thus the existence of multidomain patterns as well as non-zero δM values hascan to be attributed to inhomogeneities due to either misaligned or soft grains within each island.

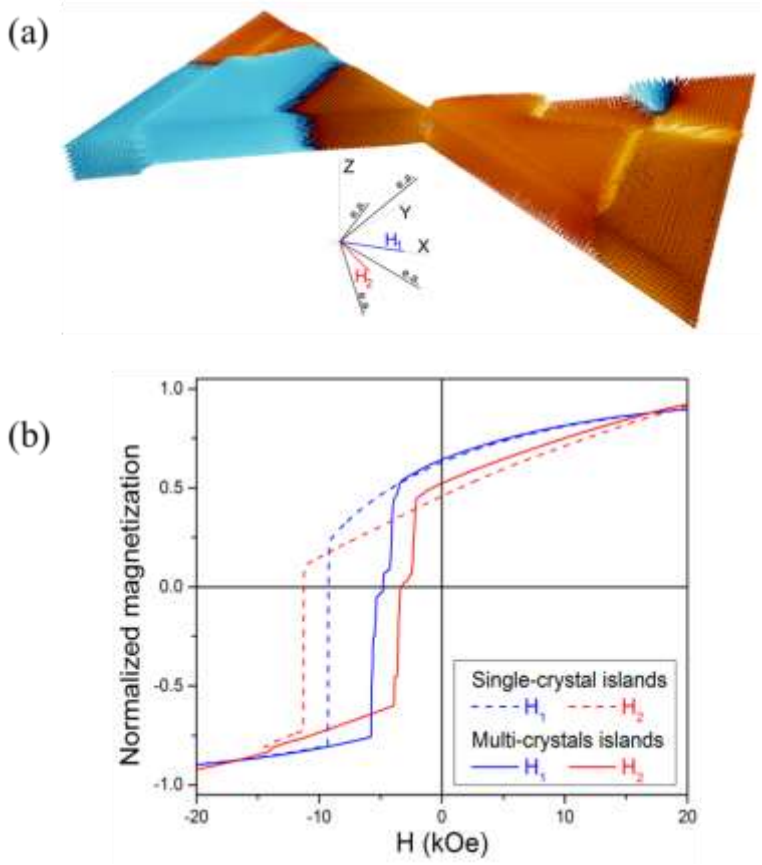

Figure 7.9: (a) Snapshot of magnetic state of two trianglular prism islands. In inset, the relative orientation of easy axes and external field. (b) Major hysteresis loop branches for two structural cases and two directions of the applied field.

7.5 Conclusions

Triangular nano-islands with an average size of 70 and 330nm have been obtained using nanosphere (173nm) and microsphere (978nm) 2D arrays as deposition masks, respectively. The nanoisland arrays have been annealed (at 500-6500 ^{o}C) in order to obtain the tetragonal structure. The highest coercivity (12.3kOe) has been obtained for the 330nm island arrays, which is a little higher than the maximum obtained for the continuous film (11. kOe). The 70nm island arrays have lower coercivity and show the existence of a de-

coupled soft magnetic phase. The switching behavior is characterized by non-zero δM-plots. The lower δM is obtained for the 70nm sample heat-treated at 500 ^{o}C for 15 minutes and increases for longer times and higher heat-treatment temperatures. According to micromagnetic calculations this can be explained by multi-domain states, which may be due to the existence of either a softer region or different anisotropy direction region within each particle. The decoupled soft phase must be attributed to a soft phase that occupies the whole nanoisland. For the 70nm island arrays, due to the increased surface area there is a higher probability of having defects but a lower probability of two-phase coexistence within each nanoisland. Thus, the soft phase appears decoupled and the interaction distribution narrower.

CHAPTER 8

8. Magnetization Reversal in Graded Anisotropy Continuous and Nanostructured Co/Pt Multilayers

The reversal mechanism of soft/hard bilayers originates in domain nucleation at the soft layer and propagation of an interfacial domain wall (IDW) into the hard phase. Since the IDW pinning field is proportional to the gradient of the magnetic anisotropy profile along the interface normal, it can be reduced by creating a graded interface. However, in order to achieve optimal performance both pinning and nucleation fields have to be simultaneously minimized [201].

Graded anisotropy films of hard magnetic phases have been produced by varying the substrate temperature during the sputter growth [33], post-annealing [202],through taking advantage of compositional gradients [203] or the different heat-treatment temperatures required [204]. Despite the practical applicability of materials incorporating magnetocrystalline anisotropy gradients, there exist some obvious limitations on accurately producing and resolving those gradients, since they are based on crystallization and chemical synthesis profiles that are created through the combined processes of diffusion, grain growth etc. In contrast, magnetic multilayer systems offer the possibility of controllably adjusting the anisotropy gradient by tuning the layer thicknesses. Kirby and coworkers [205] have used Co/Pd perpendicular anisotropy multilayers with depth-dependent Co layer thickness as a model graded anisotropy system and have proven by polarized neutron reflectometry that the thickness grading results in a corresponding magnetic anisotropy gradient. Here, we present a study of the magnetization reversal of graded Co/Pt multilayers.

The study of the effect of graded anisotropy on the magnetization reversal in perpendicular anisotropy systems presents the following complication: If the thickness (or number of repetitions equivalently [89]) exceeds a certain limit then the formation of stripe domains becomes favorable as predicted by the Kooy-Enz model [206,207] and the loops appear “slanted”. Thus deviation from a rectangular loop shape is a clear sign of a stripe domain dominated magnetization reversal [89]. In this case, the loop shape depends

strongly on how the film thickness relates to a characteristic length that scales with the ratio of domain wall energy to the demagnetizing energy $\gamma / 4\pi M_s^2$ [206,208], obscuring the straightforward interpretation of nucleation field. Furthermore, the reversal, apart from the nucleation/IDW propagation mechanisms that are related to the interface characteristics, will also include lateral domain wall (LDW) propagation that may mask the effects of the anisotropy gradient.

In order to suppress LDW mechanisms in the following study we have employed two different approaches: (i) Limitation of bilayer repetitions to eight to ensure absence of stripe domains. This strict thickness limitation brings us within the limits of a nucleation controlled reversal. (ii) Limitation of the lateral dimensions by creating multilayered nanostructures. We have nanostructured the multilayers by depositing the same sequence stack not only from continuous multilayers but as hexagonal monolayer arrays of nanospheres which act as a topographic pattern for the formation of "nanocaps". This method, introduced by M. Albrecht and coworkers [42], leads to magnetic isolation, since each nanocap has only six small contact areas with neighboring spheres, and, furthermore, the surface curvature reduces the deposited film thickness at the contact points. For a multilayer system this thickness reduction may even lead to non-magnetic behavior. A smaller faction (~9 %) of the material is deposited into isolated "triangular" islands between the spheres.

8.1 Experimental Details

Co/Pt multilayered films have been magnetron sputter deposited on silicon wafers at room temperature using a MANTIS deposition system with the Co (3") and Pt (2") sources. Prior to the deposition the chamber is evacuated to a base pressure of 7×10^{-7} Torr and the process gas (Ar 5N) pressure was 2.5mTorr. The target to substrate distance is 6". The Co layers have been deposited at a rate of 0.426Å/sec by applying 48W DC and the Pt layers at a rate of 0.523Å/sec by applying 120W RF. Layer thicknesses were determined by X-ray reflectivity measurements with a D8 Advance Bruker Diffractometer by using Cu-Kα_1 radiation (λ=1.5406Å) and a parallel beam created with a Göbel-mirror. The hysteresis loops have been performed with a Lake Shore vibrating sample magnetometer (VSM). First Order Reversal Curve (FORC) diagrams have been constructed based on

families of curves acquired by a Dual AGM/VSM Magnetometer of Princeton Measurements Corp. The Atomic Force (AFM) images have been obtained with the use of an AutoProbe CP microscope.

All the samples have been deposited on 76Å Pt ((111)-textured) underlayer, since the magnetic anisotropy of Co/Pt multilayers depends on the crystallographic orientation. In order to choose the appropriate layer thicknesses a series of multilayers $[Co(x\ nm)/Pt(2nm)]_8$ with x=0.4, 0.6, 0.8, 1.0, 1.6 were prepared and the effective uniaxial anisotropy (K_u) was estimated by the area enclosed between the parallel and perpendicular magnetization curves of VSM magnetization measurements [209]. K_u follows a linear dependence on the Co layer thickness [90,209], which corresponds to an interfacial anisotropy of K_S=3erg/cm^2 and a slope K_V=-3×10^{6}erg/cm^3. These values mean that it turns to in-plane anisotropy above x=1nm. At x=0.4nm a deviation from linear behavior occurs, since x becomes comparable with the layer roughness of the sputtering process. Thus, we have used $[Co(0.6nm)/Pt(2nm)]_8$ and $[Co(1nm)/Pt(2nm)]_8$ as end members corresponding to the perpendicular and in-plane anisotropy respectively.

In thin enough multilayers i.e. when the number of repetitions on each stack is limited to 8, the appearance of "slanted" loops due to the formation of stripe domains is avoided [206]. We term these samples as "thin" in contrast to the "thick" ones with double number of layers that exceed the critical thickness for stripe domain formation. More explicitly we have studied the following samples:

i. Thin uniform with strong K_u: $[Co(0.6nm)/Pt(2nm)]_8$.

ii. Thin uniform with vanishing K_u: $[Co(1nm)/Pt(2nm)]_8$.

iii. Thin sharp composite: $[Co(0.\ nm)/Pt(2nm)]_4/[Co(1nm)/Pt(2nm)]_4$.

iv. Thin graded composite: $[Co(x_i)/Pt]_8\ with\ x_i = 1+\frac{i-1}{7}(0.6-1)$.

v. Thin uniform with average K_u and effective anisotropy comparable to iii and iv: $[Co(0.8nm)/Pt(2nm)]_8$.

vi. Thick sharp composite: $[Co(0.6nm)/Pt(2\ nm)]_8/\ [Co(1nm)/Pt(2nm)]_8$.

vii. Thick graded composite: $[Co(x_i)/Pt]_{16}\ with\ x_i = 1+\frac{i-1}{15}(0.6-1)$.

The "thick" samples have been simultaneously deposited on monodisperse polystyrene nanosphere arrays to form nanocaps (figure 8.1). Two different nanosphere

sizes have been employed termed “micron” (970±23)nm and “nano” (173±6)nm hereinafter. The self-assembly of nanosphere polystyrene monolayer has been described in paragraph 4.2.

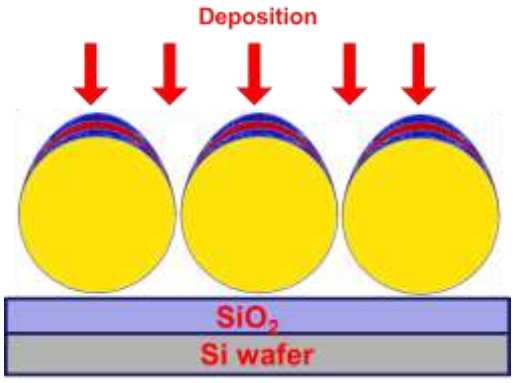

Figure 8.1: Cross-sectional schematic of the principle of “nanocap” formation by deposition on regular polystyrene sphere arrays.

8.2 Structural Characterization of Co/Pt Multilayers by GIXRD and XRD

Figure 8.2 shows a typical GIXRD pattern of $[Co(0.6nm)/Pt(2nm)]_8$. The multilayer has strong (111) texture and only Pt peaks are observed. The peak at 35^o is a satellite of the artificial superlattice. The (111) and n_{-1} peak values can be used for the calculation of total thickness of sample, which is Λ=20.8Å.

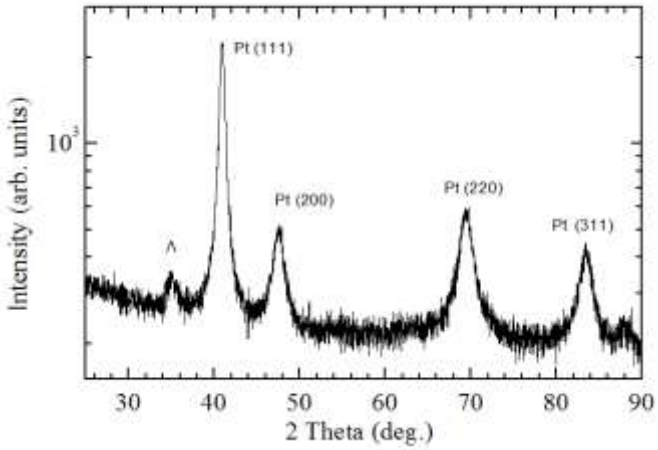

Figure 8.2: GIXRD pattern of $[Co(0.6\ nm)/Pt(2\ nm)]_8$.

Figure 8.3 shows the XRD pattern of $[Co(1.6nm)/Pt(2nm)]_8$. The main Pt (111), the Co/Pt (111) and the satellite peaks n=-1 and n=+1 for the artificial superlattice are observed. The (111) texture of multilayers is enhanced by the presence of Pt underlayer. The (111) and n_{-1} peak values yield a total sample thickness of 30.1Å.

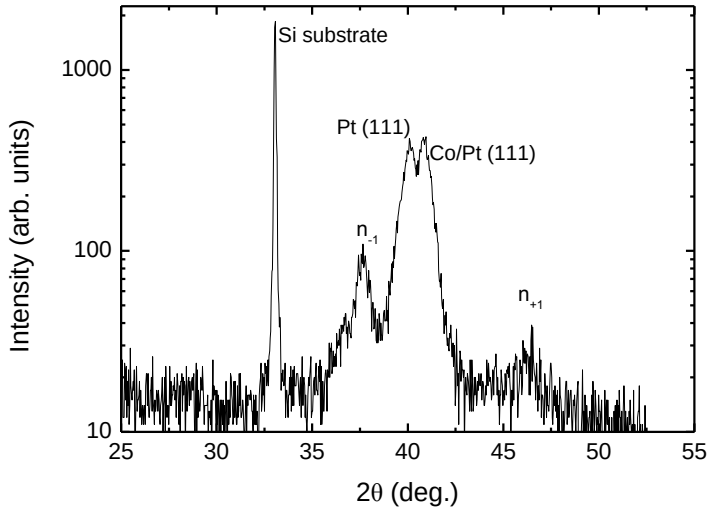

Figure 8.3: XRD pattern of $[Co(1.6nm)/Pt(2nm)]_8$.

8.3 Magnetic Properties of Continuous Co/Pt Multilayers

Figures 8.4(a) and 8.4(b) show the effective uniaxial anisotropy as a function of Co thickness and the out-of-plane magnetization hysteresis loops of $[Co(0.6nm)/Pt(2nm)]_8$ and $[Co(1nm)/Pt(2nm)]_8$, respectively. The former has a strong perpendicular anisotropy, whereas the latter's is negligible as the opposite interface and bulk (including demagnetization) contributions cancel. Their loops are characterized by totally different reversal characteristics. The reversal of the x=0.6nm (figure 8.4(b) solid circles) sample exhibits nucleation at H_N=-0.23kOe, followed by easy domain propagation resulting in a coercivity of H_c=0.28kOe. The anisotropy field, in comparison, is 2.8kOe. A "tail" around H=0.38kOe may be attributed to some domain pinning and annihilation mechanisms as we approach negative saturation. In contrast for the x=1 sample (figure 8.4(b) open squares),

nucleation starts from a positive field, H_N=0.44kOe, due to the absence of perpendicular anisotropy and strong demagnetizing effects. The slanted loop shape shows that the reversal is dominated by existence of domains with the average pinning field equal to the coercive field 0.53kOe. As already mentioned in the experimental section, these two types of layers have been combined into stacks with either four layers of each kind ("thin sharp composite") or a linearly gradual evolution from one type to the other as we move from the bottom to the top of the stack ("thin graded composite"). Both types of sample have an average anisotropy close to that of the $[Co(0.8nm)/Pt(2nm)]_8$ sample as verified by the data shown in figure 8.4(a).

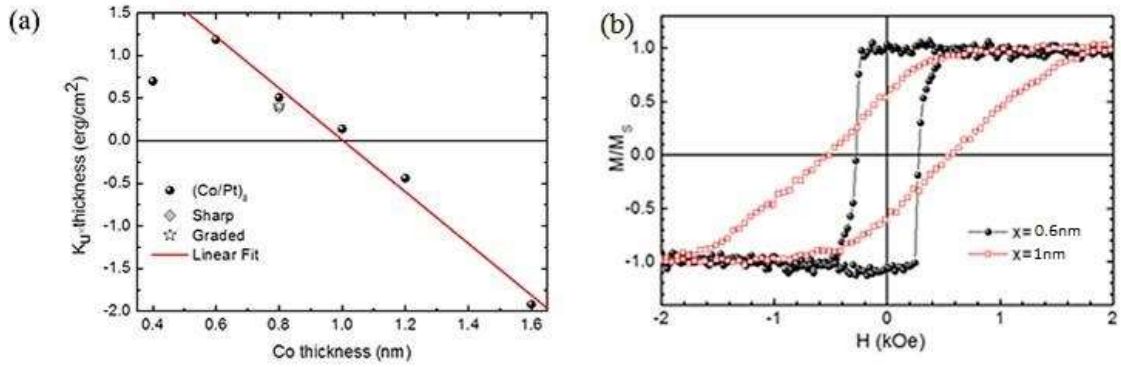

Figure 8.4: (a) The product of the effective uniaxial anisotropy K_u times the cobalt layer thickness x as a function of x and (b) the out-of-plane normalized magnetization hysteresis loops of $[Co(0.6nm)/Pt(2nm)]_8$ and $[Co(1nm)/Pt\ (2nm)]_8$.

Figure 8.5 shows the out-of-plane normalized magnetization hysteresis loops of the "thin sharp" and "thin graded" composite samples, which are compared with those of the "thin average" uniform $[Co(0.8nm)/Pt(2nm)]_8$. Some systematic differences are observed in the nucleation fields. The average structure (solid circles) has H_N=-0.45kOe, which drops to H_N=-0.34kOe and H_N=-0.28kOe for the graded (stars) and sharp (diamonds) profile stacks, respectively. This observation is in agreement with the theoretical predictions of Skomksi et al. [28]. Unlik, the clear differences in the nucleation fields, the coercivity and the "tail" of the loop are little affected by the anisotropy profile of the stack. This could be explained if nucleation is followed by LDW propagation of domains that extend through the whole stack thickness, a process that is influenced mainly by local of anisotropy variations along the film plane as opposed to the profile along the film normal.

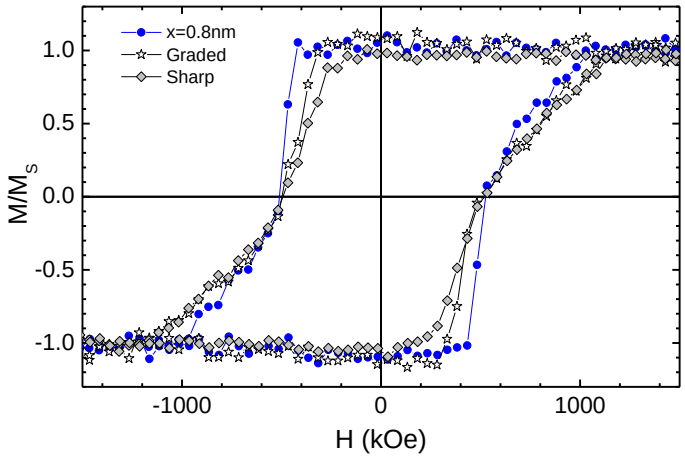

Figure 8.5: Normalized out-of-plane hysteresis loops of the [Co(0.8 nm)/Pt(2nm)]$_8$, "thin sharp" [Co(0.6nm)/Pt(2nm)]$_4$/[Co(1nm)/Pt(2nm)]$_4$ and "thin graded" $\mathbf{[Co(}\boldsymbol{x_i}\mathbf{)/Pt]_8}$ with $\boldsymbol{x_i} = \mathbf{1} + \frac{\boldsymbol{i}-\mathbf{1}}{\mathbf{7}}(\mathbf{0.6}-\mathbf{1})$ multilayers.

The dependence of reversibility on the angle ψ between the applied field and the domain wall pinning dominated. However, the exact angular dependence matches neither the Kondorsky 1/cosθ law nor its generalizations.

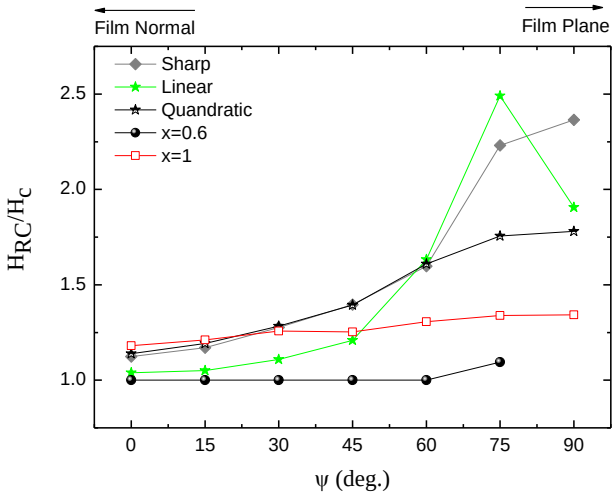

Figure 8.6: Reversibility dependence of angle theta between the applied field and film normal.

A more thorough picture of the hysteretic behavior of these systems can be obtained by the First-order Reversal Curve (FORC) diagram method. A systematic study of the FORC features of Co/Pt multilayers with perpendicular anisotropy, and their correlation with the typical maze-like stripe domain patterns observed in these systems can be found in [116,193]. Two features are observed: (i) one associated with the onset of magnetization reversal by nucleation of bubble domains followed by an avalanche-like evolution to stripe domain propagation and (ii) one corresponding to the annihilation of domains close to negative saturation. Between these the overall domain topology is preserved and only the relative width of "up" and "down" domains change, without significant pinning effects. Thus the magnetization changes are mostly reversible and do not give FORC features on the (H_R,H) plane.

FORC distributions for the thin samples are summarized in figure 8.7. For the "uniform strong K_u" x=0.6nm sample (figure 8.7(a)) a narrow feature centered at the coercive field dominates the FORC distribution indicating that the main contribution to non-reversible processes is nucleation. Two additional features of opposite polarity correspond to the tail of the loop and must be attributed to domain pinning annihilation following the main nucleation process. The existence of this combined negative valley and a positive peak stretching along the H_R axis direction has been reported for "single-phase" Co/Pt multilayers [210]. However, these twin features are more pronounced in hard/soft systems when hard and soft layers are coupled and switch together [211]. In contrast, the "uniform vanishing K_u" x=1nm sample (figure 8.7(b)) shows a characteristic FORC distribution with two positive peaks in symmetric positions both having H_c=0.6kOe and opposite interaction fields H_U=±0.6kOe. No other distinct features can be observed between these two peaks. This is indicative of domains whose shape is defined mainly by the strong demagnetizing energy associated with the thin film geometry [206-208]. In this case irreversible processes occur mainly when reducing/approaching the field from/to saturation i.e. changing the balance between Zeeman and demagnetizing energy thus leading to domain creation/annihilation events. These two peaks are superimposed on a smooth smeared out background arising from irreversible domain wall depinning events. The "sharp" and "graded" exchange spring samples (figure 8.7(c) and (d), respectively) have FORC distributions that resemble that of x=0.6nm but with broadened features. The top feature corresponds to nucleation but it is broadened along the H-axis as the nucleated reversed domains are only eliminated as we approach the saturation field. Two additional

features of opposite polarity again must be assigned to domain annihilation events as we move back to positive saturation from the "tail" of the loops. The negative part is much more extended in the case of the "sharp" sample since the softer x=1nm stack is less coupled than is the case in the higher anisotropy x=0.6nm.

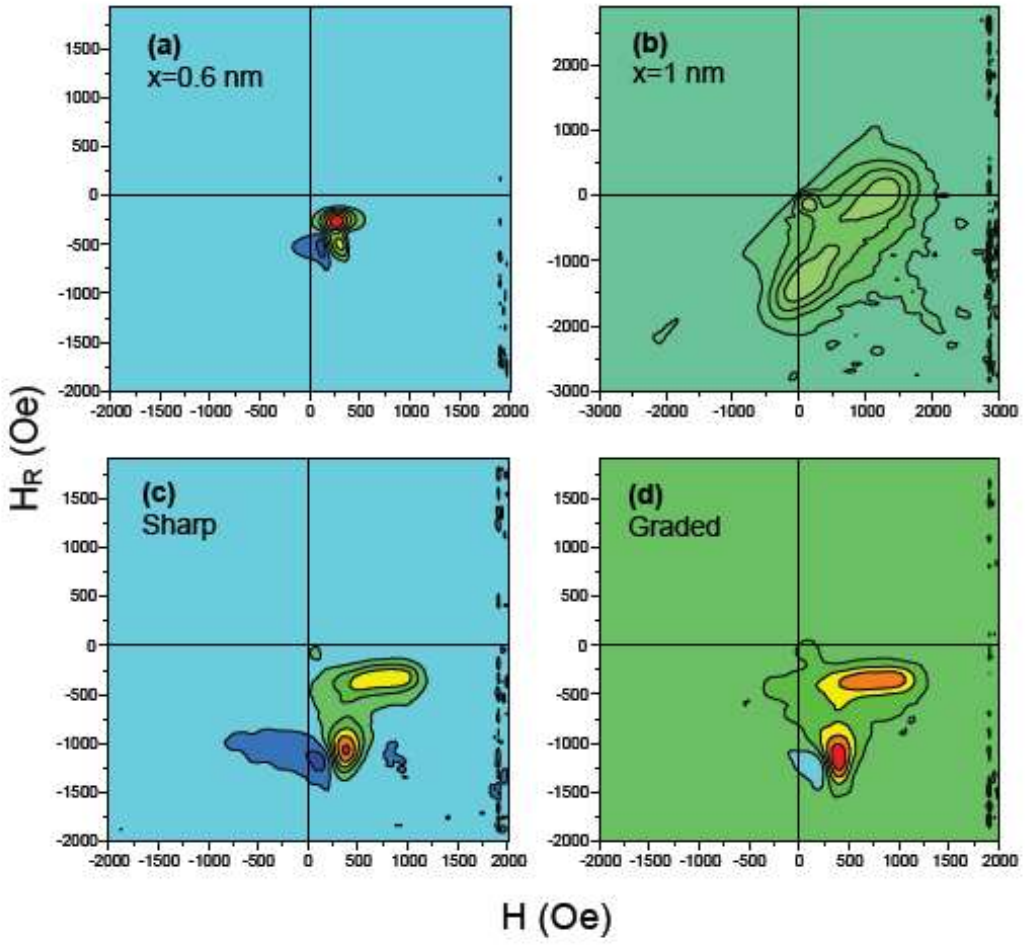

Figure 8.7: FORC distributions for the (a) $[Co(0.6nm)/Pt(2nm)]_8$, (b) $[Co(1nm)/Pt(2nm)]_8$, (c) "thin sharp", $[Co(0.6nm)/Pt(2nm)]_4/[Co(1nm)/Pt(2nm)]_4$ and (d) "thin graded" $[Co(x_i)/Pt]_8$ with $x_i = 1 + \frac{i-1}{7}(0.6 - 1)$ multilayers. The measurements were done with the applied field perpendicular to the film plane.

8.4 Magnetic Properties of Thick Continuous and Nanostructured Co/Pt Multilayers

In the case of continuous multilayered films deposited on silicon wafers, the thicker 16-period samples exceed the critical thickness for the formation of stripe domains. It is therefore of interest to compare these films with their counterparts deposited on nanostructures (figure 8.8) that suppress the domain formation.

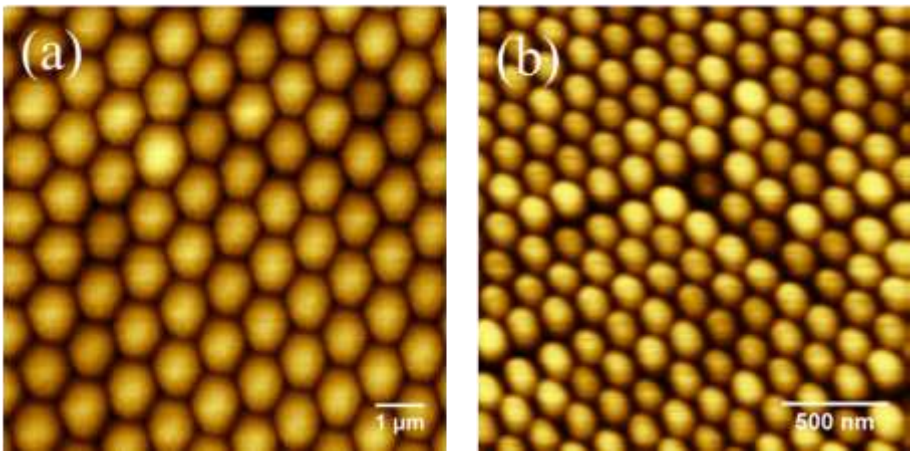

Figure 8.8: AFM image of thick $[Co(0.6\ nm)/Pt(2nm)]_8/[Co(1\ nm)/Pt(2nm)]_8$ multilayers on (a) 970 nm and (b) 173 nm nanosphere monolayer.

In figure 8.9 typical examples of the families of recoil curves used to construct the FORC diagrams are shown. The suppression of domains in the nanostructured sample (figure 8.9(a)) is indicated by the lack of a constriction in the major hysteresis loop, as is observed in the continuous sample (figure 8.9(b)). It was recently reported that the deposition of Co/Pd multilayers onto self-assembled spherical particles creates a single-domain, exchange decoupled system, but with electrically connected magnetic entities [50]. Furthermore, similar suppression of domain motion has been reported in 1.4μm circular dot arrays of graded Co/Pd multilayers [212]. Interestingly it was shown that domains continue to exist within each Co/Pd dot. These domains retain similar dimensions and topography to that of the continuous film. Thus, the change of the magnetic properties is due to the limited lateral contiguity at the edge of each dot. As a consequence the peaks

of the switching field distribution corresponding to the creation and annihilation of domains are less pronounced.

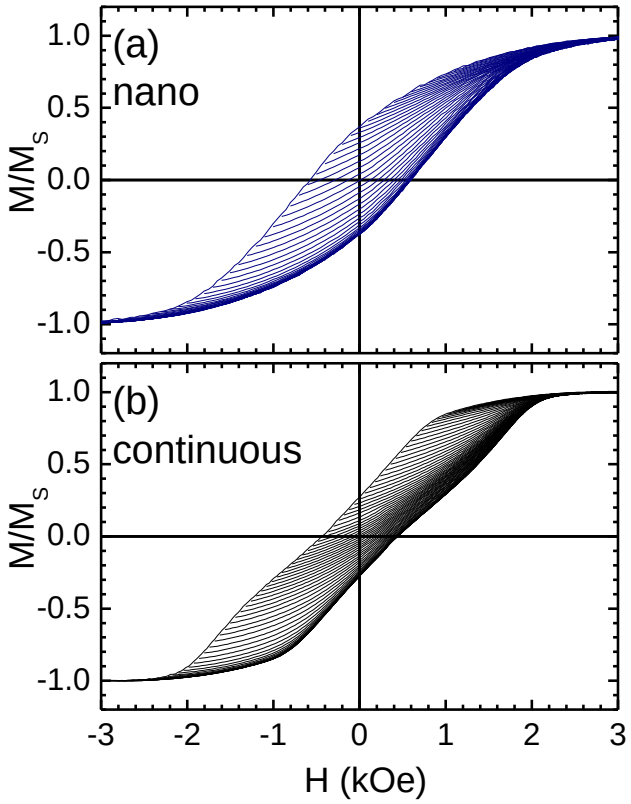

Figure 8.9: Comparison of families of FORC curves of (a) nanostructured graded anisotropy multilayers $[\mathbf{Co}(\boldsymbol{x_i})/\mathbf{Pt}]_{\mathbf{16}}$ and (b) continuous ones.

In order to fully access the reversal mechanism information that lies in the shape of the recoil curve families, FORC distributions have been obtained. FORC diagrams often reveal striking differences between samples that show only subtle changes in their major hysteresis loops [213]. For the "sharp" or "graded" continuous thick exchange spring films (figures 8.10(a) and (b), respectively) the FORC diagrams show two positive features in symmetric positions implying similar coercivities (H_c=0.6kOe) and opposite interaction fields H_i=±1.4kOe and H_i=±1.1kOe, respectively. This is in accordance with the established observation that graded interfaces give more effective coupling. The less effective coupling in the "sharp" is further supported by the small uncoupled fraction with H_c=0.28kOe that is

observed close the origin. These features are completely suppressed for the samples that have been deposited on micro or nano-structured templates (figures 8.10(c) to (f)). In nanostructured samples the FORC distributions are characterized by one central feature at zero interaction field. In Ref. [213] a similar transition from the "twin-feature" FORC diagrams (such as those of figure 6(a) and (b)) to the "single-ridge" (as in figures 8.10(c) to (f)) has been monitored in Fe dots by simply changing the size from 52nm to 67nm. The twin features can be attributed to the nucleation and annihilation of vortices and this is confirmed by micromagnetic simulations.

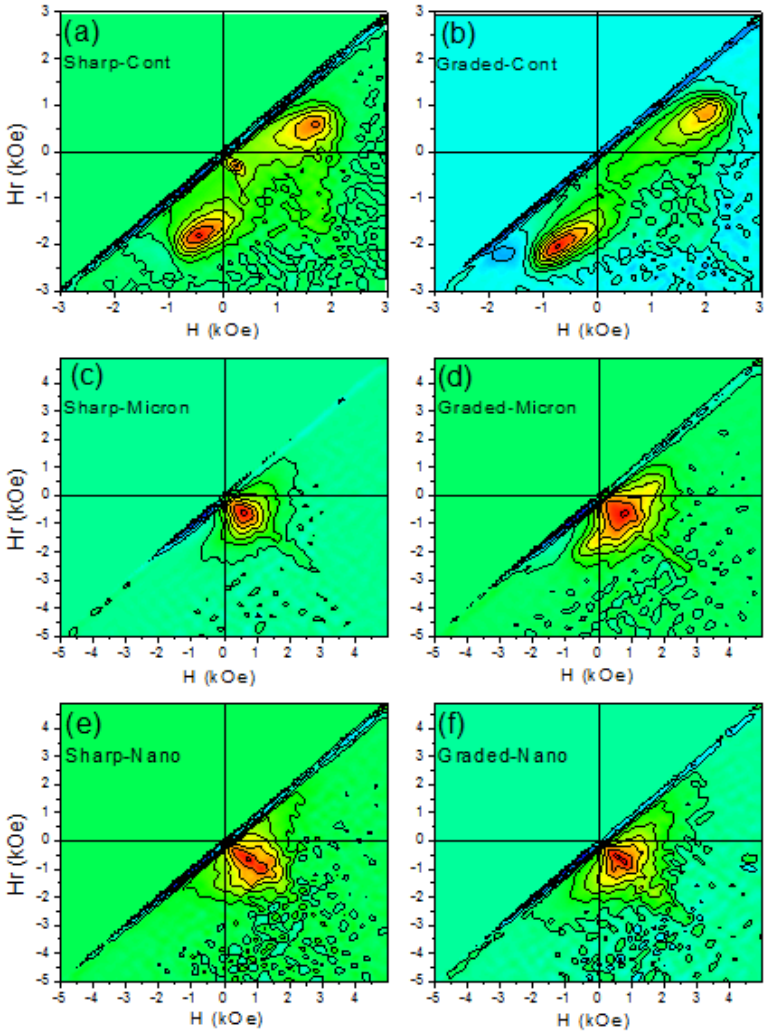

Figure 8.10: FORC distributions for "thick sharp" $[Co(0.6nm)/Pt(2nm)]_8/[Co(1nm)/Pt(2nm)]_8$ (left column) and "thick graded" $[Co(x_i)/Pt]_{16}$ (right column) with x_i=1+((i-1)/15)(0.6-1) multilayers. Top row (a-b) continuous films, middle row (c-d) films deposited as caps on micron sized polystyrene sphere arrays, bottom row (e-f) "nanocaps" deposited on nano-sized polystyrene sphere arrays.

For samples deposited on micron-sized spheres the "sharp" distribution is centered at a slightly lower H_c=0.6kOe (figure 8.10(c)) with respect to the "graded" H_c=0.7kOe (figure 8.10 (d)). This again verifies the observation that sharp interfaces lead to lower nucleation fields. For the samples deposited on nanospheres (figure 8.10(e) and (f)) there are no appreciable differences between "graded" and "sharp" anisotropy profiles. In general their FORC distributions resemble those deposited on the microspheres. Estimations of the critical diameter D_{sd} for single-domain Co/Pt multilayer dots, investigated by anomalous Hall effect, show that in the low anisotropy limit D_{sd} is below 150nm [214]. This may explain why nanosphere and microsphere samples share similar characteristics in their FORC distributions.

8.5 Conclusions

In conclusion, a FORC study of the magnetization reversal of graded Co/Pt multilayers was based on comparing: (i) Samples with total thicknesses below and above the critical thickness for stripe domain formation (ii) continuous films to films deposited on micro and nanosphere arrays and (iii) films with graded anisotropy profiles to films with sharp profiles.

The FORC distributions fall under three different types:

(a) Twin distributions with two broad symmetric positive features having opposite interaction fields $\pm H_U$ e.g. figures 8.7(b), 8.10(a) and 8.10(b). These correspond to the creation and annihilation of domains. The lack of features in-between these twin characteristics is related to the lack of irreversible processes since the dimensions and relative fractions of opposite domains are reversibly defined in the intermediate field region mainly by the demagnetizing effects.

(b) Continuous samples with nucleation controlled reversal show a central feature at the nucleation field, which also defines the coercive field, accompanied by two features of opposite polarity due to domain effects at fields between the coercive and the saturation. This type of FORC is observed in the thin continuous samples with perpendicular anisotropy.

(c) In samples deposited on nanostructured templates the domain effects are suppressed and the FORC distributions show only one central feature broadened mainly along the interaction axis.

The graded profile is found to influence nucleation in thin films. This effect is masked by the strong dependence of loop shape on thickness and demagnetizing energy in thicker films. Since current applications require features of limited thickness the most relevant feature of anisotropy graded structures is their nucleation fields.

CHAPTER 9

9. Summary and Outlook

The main aspect of this work was to provide a comprehensive morphological, structural and magnetic characterization of nanostructured high magnetic anisotropy Pt-TM (TM=Co, Fe, Cr) films. The study was focused on four main subject areas:

i. The effect of layering and thickness in $L1_2$-$CrPt_3$ and $L1_0$-CoPt co-deposited films, bilayers and trilayers.
ii. Perpendicular anisotropy in magnetically annealed $L1_0$-Co/Pt multilayers.
iii. Morphological, structural and magnetic characterization of $L1_0$-FePt nanostructures obtained by polystyrene sphere array masks.
iv. Magnetization reversal in graded anisotropy Co/Pt multilayers deposited on Si substrates and nanospheres.

The effect of layering and thickness were studied in $CrPt_3$ and CoPt films. Trilayers achieve higher degrees of ordering and coercivity compared to co-deposited films. In CoPt films the fcc phase is present at all annealing temperatures, suggesting the partial transformation from the A1 to $L1_0$ structure. In contrast Co/Pt bilayers are fully transformed to the $L1_0$ structure at 700 ^oC. Thin trilayers are fully transformed to $L1_0$ at 750 ^oC, but the degree of chemical ordering is lower compared to that of a thicker bilayer annealed under the same conditions. The TEM analysis of Co-Pt films reveals that the twin density in trilayers is larger compared with the CoPt single layer. The average size of grains in CoPt single layers are 32nm, while the average size of Co/CoPt/Pt trilayers is 42nm.

The effect of magnetic annealing on the texture was investigated in a series of CoPt films of different thickness obtained by annealing Co/Pt multilayers. We have seen that by annealing under a even weak magnetic field (1kOe) magnetron sputtered CoPt alloy and Co/Pt bilayers can achieve (001) crystallographic texture and that an even higher degree of (001) texture can be obtained by magnetically annealing Co/Pt bilayers. The origin of this

texture was not clear as in some cases it can be obtained even appling an in-plane field. We present a systematic X-ray diffraction (XRD) and Transmission Electron Microscopy (TEM) investigation of $L1_0$ CoPt film samples of different total thickness (17-68nm) each one obtained by annealing samples with different types of layering from $(Co/Pt)_2$ bilayers to $(Co/Pt)_{16}$ multilayers. The 17nm samples show (001) texture even without an applied magnetic field, whereas in 34nm samples (001) texture is obtained only after magnetic field annealing. This can be correlated with their microstuctures: The 17nm samples are polycrystalline, and in some areas discontinuous. The grain sizes (200~250nm) are remarkably larger than that of thicker samples while the 68nm sample is continuous and has the smallest grain size (25-200nm). A strong correlation of the (001) texture with the c axis strain has been observed showing that it is related to chemical order. The effect of the field may be to correlate local strains at a macroscopic level. In 68nm samples, (001) texture cannot be obtained in accordance with the analysis of Ref. [177] indicating that the films should be sufficiently thin so that a plane-stress condition for the relaxation along the surface normal applies.

Triangular FePt nano-islands with sizes ~70 and ~330nm have been prepared by using regular single-layer arrays of nanospheres (173nm) and microspheres (970nm), as deposition masks. The coercivity of the 330nm islands is close to that of the continuous film (11kOe) whereas the 70nm samples has a coercivity close to 9kOe with a hysteresis consistent with the coexistence of an uncoupled soft phase. The switching behavior is characterized by non-zero dM-plots. The lower dM is obtained for the 70nm sample heat-treated at 500^0C for 15 minutes and increases for longer times and higher heat-treatment temperatures. 10% of the islands are in a multi-domain state. These findings were compared with micromagnetic modeling studies which shows that for anisotropy values high enough to match the observed coercivity, multidomain islands can result due to the existence of either a soft regions or different anisotropy direction regions within the magnetic entities.

Finally, the magnetization reversal in graded anisotropy Co/Pt multilayers was studied by First Order Reversal Curve diagrams (FORC). The graded profile clearly influences the nucleation field in thin films but this effect is masked by the strong demagnetizing field dependence in thicker films. For samples with total thicknesses above the threshold value for stripe domain formation, the FORC distribution shows two positive features that correspond to domain nucleation and annihilation. Between these two peaks

no other distinct features are visible, due the high reversibility of domain pattern characteristics. In thin continuous films a marked feature corresponding to nucleation is accompanied by two features of opposite polarity characteristic of two-phase interactions. In nanostructured samples the domain effects are suppressed and the FORC is dominated by a single feature elongated along the interaction axis.

Even though in the framework of this thesis a systematic study of magnetic, structural and morphological characterization of nanostructured and continuous films was done many interesting points for further study arose. It would be interesting to study the formation of (001) textured CoPt films with magnetic annealing using higher fields (>0.5 T) and controlling the cooling rates as the latter may play a decisive role in transformation strains that determine the texture. The use of nanospheres as a mask for the formation of triangular-like nanoislands can be extended to the formation of nanoring and nano-crescent arrays by appropriate shadowing techniques under oblique incidence deposition. These nanopattens are very interesting for the study and control of vortex chirality. Finally, some open questions remain as to the shape and size change of FORC-diagram twin interaction features whose origin and characteristics could be elucidated by varying the film coupling and thickness parameters.

Bibliography

[1] J.M.D. Coey, *Magnetism and Magnetic Materials*, Cambridge: Cambridge University Press (2010).

[2] H.N. Bertram, M. Williams, "SNR and density limit estimates: A comparison of longitudinal and perpendicular recording", IEEE Trans. Magn. **36 (1)**, 4 (2000).

[3] D. Niarchos, E. Manios and I. Panagiotopoulos, "Towards terabit/in^2 magnetic storage media", Mater. Res. Soc. Symp. Proc. Vol. **1106**, 62-80 (2008).

[4] B.D. Terris, "Fabrication challenges for patterned recording media", J. Magn. Magn. Mater. **321(6)**, 512-517 (2009).

[5] H.J. Richter, "The transition from longitudinal to perpendicular recording", J. Phys. D: Appl. Phys. **40**, R149-R177 (2007).

[6] Ι. Παναγιωτόπουλος, *Μαγνητικά Υλικά και Υπεραγωγοί,* Εκδόσεις Πνευματικός (2010).

[7] C.P. Bean and J.D. Livingston, "Superparamagnetism", J. Appl. Phys. **30**, S120 (1959).

[8] D. Weller and A. Moser, "Thermal effect limits in ultra-high density magnetic rcording", IEEE Trans. Magn. **35**, 4423-4439 (1999).

[9] Y. Yu, Y. Liu and D.J. Sellmyer, "Nanostructure and magnetic properties of composite CoPt:C films for extremely high-density recording", J. Appl. Phys. **87**, 6959 (2000).

[10] K.Z. Gao, O. Heinonen, and Y. Chen, "Read and write processes, and head technology for perpendicular recording", J. Magn. Magn. Mater. **321**, 495 (2009).

[11] S. Iwasaki and K. Takemura, "An analysis for the circular mode of magnetization in short wavelength recording", IEEE Trans. Magn. **11**, 1173 (1975).

[12] R.L. White, "The physical boundaries to high-density magnetic recording", J. Magn. Magn. Mater. **209**, 1-5 (2000).

[13] S.N. Piramanayagam and K. Srinivasan, "Recording media research for future hard disk drives", J. Magn. Magn. Mater. **321**, 485-494 (2009).

[14] S.N. Piramayanagam, "Perpendicular recording media for hard disk drives", J. Appl. Phys. **102**, 011301 (2007).

[15] Y. Inaba, T. Shimatsu, T. Oikawa, H. Sato, H. Aoi, H. Muraoka and Y. Nakamura, "Optimization of the SiO_2 content in CoPtCr-SiO_2 perpendicular recording media for high-density recording", IEEE Trans. Magn. **40**, 2486 (2004).

[16] Y. Yamane, S. Watanable, J. Ariake, N. Honda, K. Ouchi and S. Iwasaki, "Effect of oxygen on magnetic properties of $CoPtCrSiO_2$ thin films for perpendicular recording media", J. Magn. Magn. Mater. **287**, 153 (2005).

[17] A. Moser, K. Takano, D.T. Margulies, M. Albrecht, Y. Sonobe, Y. Ikeda, S. Sun and E.E. Fullerton, "Magnetic recording: advancing into future", J. Phys. D : Appl. Phys. **35**, R157-R167 (2002).

[18] W. Peng, R.H. Victora and J.H. Judy, "Co/Pd and Co/Pt multilayers with indium tin oxide seed layers and NiFe soft underlayers for perpendicular magnetic recording media", IEEE Trans. Magn. **37**, 1537-1579 (2001).

[19] T.D. Leonhardt, Y. Chen, M. Rao, D.E. Laughlin, D.N. Lambeth and M.H. Kryder, "$CrPt_3$ thin film media for perpendicular or magneto-optical recording", J. Appl. Phys. **85**, 4307 (1999).

[20] M. R. Visokay and R. Sinclair, "Direct formation of ordered CoPt and FePt compound thin films by sputtering", Appl. Phys. Lett. **66**, 1692 (1995).

[21] D. E. Laughlin, N. T. Nuhfer, S. Park, H. Yuan and J. G. Zhu, "Topology and elemental distribution in Co alloy: oxide perpendicular media", J. Appl. Phys. **105**, 07B739 (2009).

[22] J.P. Wang, W.K. Shen, J.M. Bai, R.H. Victora, J.H. Judy and W.L. Song, "Composite media (dynamic tilted media) for magnetic recording", Appl. Phys. Lett. **86**, 142504 (2005).

[23] D. Suess, "Multilayer exchange spring media for magnetic recording", Appl. Phys. Lett. **89,** 113105 (2006).

[24] E. E. Fullerton, J.S. Jiang and S.D. Bader, "Hard/soft magnetic heterosructures: Model exchange spring magnets", J. Magn. Magn. Mat. **200**, 392-404 (1999).

[25] J.S. Jiang, J.E. Pearson, Z.Y. Liu, B. Kabius, S. Trasobares, D.J. Miller, S.D. Bader, D.R. Lee, D. Haskel, G. Srajer and J.P. Liu, "A new approach for improving exchange-spring magnets", J. Appl. Phys. **97**, 10K311 (2005).

[26] D. Suess, T. Schrefl, S. Fähler, M. Kirschner, G. Hrkac, F. Dorfbauer and J. Fidler, "Exchange spring media for perpendicular recording", Appl. Phys. Lett. **87**, 012504 (2005).

[27] A. Goncharov, T. Schrefl, G. Hrkac, J. Dean, S. Bance, D. Suess, O. Ertl, F. Dorfbauer and J. Fidler, "Recording simulations on graded media for area densities of up to 1 Tbit/in^2", Appl. Phys. Lett. **91**, 222502 (2007).

[28] R. Skomski, T.A. George and D.J. Sellmyer, "Nucleation and wall motion in graded media", J. Appl. Phys. **103**, 07F531 (2008).

[29] G.T. Zimanyi, "Graded media: Optimization and energy barrier", J. Appl. Phys. **103**, 07F543 (2008).

[30] D. Suess, J.Lee, J.Fidler, T.Schrefl, "Exchange-coupled perpendicular media", J. Magn. Magn. Mater. **321**, 545–554 (2009).

[31] V. Alexandrakis, D. Niarchos, K. Mergia, J. Lee, J. Fidler and I. Panagiotopoulos, "Magnetic properties of graded A1/$L1_0$ films obtained by heat treatment of FePt/CoPt multilayers", J. Appl. Phys. **107**, 013903 (2010).

[32] D. Makarov, J. Lee, C. Brombacher, C. Schubert, M. Fuger, D. Suess, J. Fidler and M. Albrecht, "Perpendicular FePt-based exchange-coupled composite media", Appl. Phys. Lett. **96**, 062501 (2010).

[33] D. Goll, A. Breitling, L. Gu, P.A. van Aken and W. Sigle, "Experimental realization of graded $L1_0$-FePt/Fe composite media with perpendicular magnetization", J. Appl. Phys. **104**, 083903 (2008).

[34] B.J. Kirby, S.M. Watson, J.E. Davies, G.T. Zimanyi, K. Liu, R.D. Shull and J.A. Borchers, "Direct observation of magnetic gradient in Co/Pd pressure-graded media", J. Appl. Phys. **105**, 07C929 (2009).

[35] C.L. Zha, R.K. Dumas, Y.Y. Fang, V. Bonanni, J. Nogués and J. Åkerman, "Continuously graded anisotropy in single $(Fe_{53}Pt_{47})_{100-x}Cu_x$ films", Appl. Phys. Lett. **97**, 182504 (2010).

[36] R.K. Dumas, Y. Fang, B.J. Kirby, C. Zha, V. Bonanni, J. Nogués, and J. Åkerman, "Probing vertically graded anisotropy in FePtCu films", Phys. Rev. B **84**, 054434 (2011).

[37] H.J. Richter, "Density limits imposed by the microstructure of magnetic recording media", J. Magn. Magn. Mat. **321**, 467–476 (2009).

[38] A. Kikitsu, "Prospects for bit patterned media for high-density magnetic recording", J. Magn. Magn. Mat. **321**, 526–530 (2009).

[39] G.J. Li, C.W. Leung, Z.Q. Lei, K.W. Lin, P.T. Laa, Philip W.T. Pong, "Patterning of FePt for magnetic recording", Thin Solid Films **519(23)**, 8307-8311 (2011).

[40] T. Bublat and D. Goll, “Influence of dot size and annealing on the magnetic properties of large-area $L1_0$-FePt nanopatterns”, J. Appl. Phys. **110**, 073908 (2011).

[41] T. Bublat and D. Goll, “Large-area hard magnetic $L1_0$-FePt nanopatterns by nanoimprint lithography”, Nanotechnology **22**, 315301 (6pp) (2011).

[42] M. Albrecht, G. Hu, I.L. Guhr, T.C. Ulbrich, H. Boneberg, P. Leiderer and G. Schatz, “Magnetic multilayers on nanospheres”, Nature Materials **4**, 203 (2005).

[43] V. Gianneta, M. Huffman and A.G. Nassiopoulou, “Formation of porous anodic alumina templates in selected micrometer-sized areas on a Si substrate. Application for growing ordered Ti nanopillars”, Phys. Stat. Sol. A **206**, No. 6, 1309–1312 (2009).

[44] M.T. Rahman, R.K. Dumas, N. Eibagi, N.N. Shams, Y.C. Wu, K. Liu and C.H. Lai, “Controlling magnetization reversal in Co/Pt nanostructures with perpendicular anisotropy”, Appl. Phys. Lett. **94**, 042507 (2009).

[45] S.M. Weekes, F.Y. Ogrin, and W.A. Murray, “Fabrication of Large-Area Ferromagnetic Arrays Using Etched Nanosphere Lithography”, Langmuir **20**, 11208-11212 (2004).

[46] C.L. Haynes and R.P. Van Dayne, “Nanosphere lithography: A versatile nanofabrication tool for studies of size-dependent nanoparticles optics”, J. Phys. Chem. B **105**, 5599-5611 (2011).

[47] J. Zhang, Y. Li, X. Zhang and B. Yang, “Colloidal self-assembly meets nanofabrication: From two-dimensional colloidal crystals to nanostructure arrays”, Adv. Mater. **22**, 4249–4269 (2010).

[48] M.C. Gwinner, E. Koroknay, L. Fu, P. Patoka, W. Kandulski, M. Giersig and H. Giessen, “Periodic large-area metallic split-ring resonator metamaterial fabrication based on shadow nanosphere lithography”, Small **5**, 400–406 (2009).

[49] M. Retsch, M. Tamm, N. Bocchio, N. Horn, R. Förch, U. Jonas and M. Kreiter, “Parallel preparation of densely packed arrays of 150-nm gold-nanocrescent resonators in three dimensions”, Small **5**, 2105–2110 (2009).

[50] J.K. née Moser, V. Kunej, H.F. Pernau, E. Scheer and M. Albrecht, “Magnetoresistive effects in Co/Pd multilayers on self-assembled nanoparticles”, J. Appl. Phys. **107**, 09C506 (2010).

[51] C.M. Günther, O. Hellwig, A. Menzel, B. Pfau, F. Radu, D. Makarov, M. Albrecht, A. Goncharov, T. Schrefl, W.F. Schlotter, R. Rick, J. Lüning, S. Eisebitt, "Microscopic reversal behavior of magnetically capped nanospheres", Phys. Rev. B **81**, 064411 (2010).

[52] H. Zhong, G. Tarrach, P. Wu, A. Drechsler, D. Wei and J. Yuan, Nanotechnology **19**, 095703 (2008).

[53] W. Peiwen, F. Yikun, T. Xinlin, W. Xiaogong, H. Baoshan and Y. Jun, "Preparation of FePt magnetic nanodot arrays by nanosphere lithography", Chinese Science Bulletin **52 (8)**, 1125-1128 (2007).

[54] L. Graf and A. Kussmann, "Equilibrium diagram and magnetic properties of Pt-Fe alloys", Z. Phys. **36**, 544 (1935).

[55] J.M.D Coey, "Hard magnetic materials: A perspective", IEEE Trans. Magn. **47**, 4671-4681 (2011).

[56] J. Lyubina, B. Rellinghaus, O. Gutfleisch and M. Albrecht, *Structure and Magnetic Properties of $L1_0$ Ordered FePt Alloys and Nanoparticles, Handbook of Magnetic Materials*, edited by K.H.J. Buschow, vol. 19, chapter 5, pp. 291–407, Elsevier, Great Britain, (2011).

[57] P. Rasmussen, X. Rui and J.E. Shield, "Texture formation in FePt thin films via thermal stress management", Appl. Phys. Lett. **86**, 191915 (2005).

[58] K.R. Coffrey, M.A. Parker and J.K. Howard, "High anisotropy $L1_0$ thin films for longitudinal recording", IEEE Trans. Magn. **31**, 2737-2739 (1995).

[59] A. Cebollada, D. Weller, J. Sticht, G.R. Harp, R.F.C. Farrow, R.F. Marks and R. Savoy and J.C. Scott, "Enhanced magneto-optical Kerr effect in spontaneously ordered FePt alloys: Quantitative agreement between theory and experiment", Phys. Rev. B **50**, 3419-3422 (1994).

[60] M.R. Visokay and R. Sinclair, "Direct formation of ordered CoPt and FePt compound thin films by sputtering", Appl. Phys. Lett. **66**, 1692 (1995).

[61] T. Shima, T. Moriguchi, S. Mitani and Y.K. Takanashi, "Low-temperature fabrication of $L1_0$ ordered FePt alloy by alternate monatomic layer deposition", Appl. Phys. Lett. **80**, 288 (2002).

[62] C.P. Luo and D.J. Sellmyer, "Magnetic properties and structure of Fe/Pt thin films", IEEE Trans. Magn. **31**, 2764 (1995).

[63] Y.K. Takahashi, M. Ohmuna and K. Hono, "Effect of Cu on the structure and magnetic properties of FePt sputtered film", J. Magn. Magn. Mat. **246**, 259 (2002).

[64] S. Sun, C.B. Murray, D. Weller, L. Folks and A. Moser, "Monodisperse FePt nanoparticles and ferromagnetic FePt nanocrystal superlattices", Science **287**, 1989-1992 (2000).

[65] I. Zafiropoulou, V. Tzitzios, D. Petridis, E. Devlin, J. Fidler, S. Hoefinger and D. Niarchos, "Optimized synthesis and annealing conditions of $L1_0$ FePt nanoparticles", Nanotechnology **16**, 1603-1607 (2005).

[66] A. Menshikov, T. Tarnoczi and E. Kren, "Magnetic structure of ordered FePt and Fe_3Pt alloys", Phys. Stat. Sol. (a) **28**, K85 (1975).

[67] O. Gutfleisch, J. Lyubina, K.H. Müller and L. Schultz, "FePt hard magnets", Adv. Eng. Mater. **7**, 208 (2005).

[68] W. Jellinghaus, "New alloys with high coercive force", Z. Tech. Phys. (Leipzig) **17**, 33 (1936).

[69] T.J. Klemmer, D. Hoydick, H. Okumura, B. Zhang and W.A. Soffa, "Magnetic hardening and coercivity mechanisms in $L1_0$ ordered FePd ferromagnets", Scr. Metall. **33**, 1793 (1995).

[70] B.D. Cullity and C.D. Graham, *Introduction to Magnetic Materials*, Second Edition, John Wiley & Sons, Inc., Hoboken, NJ, USA (2009).

[71] R. Skomski, *Simple Models of Magnetism*, Oxford University Press (2008).

[72] J. Lyubina, I. Opahle, K.H. Muller, O. Gutfleisch, M. Richter, M. Wolf and L. Schultz, "Magnetocrystalline anisotropy in $L1_0$ FePt and exchange coupling in FePt/Fe_3Pt nanocomposites", J. Phys.: Cond. Matter **17**, 4157-4170 (2005).

[73] J.B. Staunton, S. Ostanin, S.S.A. Razee, B. Gyorffy, L. Szunyogh, B. Ginatempo and E. Bruno, "Long-range chemical order effects upon the magnetic anisotropy of FePt alloys from an ab initio electronic structure theory", J. Phys.: Condens. Matter **16**, S5623 (2004).

[74] C.J. As, L. Szunyogh, J.S. Chen and R.W. Chantrell, "Magnetic anisotropy of FePt: Effect of lattice distortion and chemical disorder", Appl. Phys. Lett. **99**, 132501 (2011).

[75] Y. Kota and A. Sakuma, "Magnetocrystalline anisotropy in FePt with $L1_0$ ordering and tetragonal distortion", J. Appl. Phys. **111**, 07A310 (2012).

[76] S.K. Burke, B.D. Rainford, D E G. Williams, P.J. Brown, and D.A. Hukin, "Magnetization density in ferrimagnetic Pt_3Cr", J. Magn. Magn. Mater. **15-18**, Part1, 505 (1980).

[77] M.J. Besnus and A.J.P. Meyer, "Magnetic properties of the ordered and disordered $CrPt_3$ and CrPt phases", Phys. Stat. Sol. (b) **58**, 533 (1973).

[78] T. Kato, H. Ito, K. Sugihara, S. Tsunashima and S. Iwata, "Magnetic anisotropy of MBE grown $MnPt_3$ and $CrPt_3$ ordered alloy films", J. Magn. Magn. Mater. **272**, 778 (2004).

[79] P.M Oppeneer, I. Galanakis, A. Grechnev and O. Eriksson, "Unusual magnetism and magnetocrystalline anisotropy of CrPt3", J. Magn. Magn. Mater. **240**, 371-373 (2005).

[80] M. Vergoehl and J. Schoenes, "Polar Kerr effect of $MnPt_3$ and $CrPt_3$", J. Magn. Soc. Jpn. **20**, 151 (1996).

[81] J. Cho, M. Park, H.-S. Kim, T. Kato, S. Iwata and S. Tsunashima, "Large Kerr rotation in ordered $CrPt_3$ films", J. Appl. Phys. **86**, 3149 (1999).

[82] P.F. Carcia, A.D. Meinhaldt and A. Suna, "Perpendicular magnetic anisotropy in Pd/Co thin film layered structures", Appl. Phys. Lett. **47**, 178 (1985).

[83] S. Hashimoto, Y. Ochiai and K. Aso, "Perpendicular magnetic anisotropy and magnetostriction of sputtered Co/Pd and Co/Pt multilayered films", J. Appl. Phys **66**, 4909 (1989).

[84] B.N. Engel, C.D. England, R.A. Van Leeuwen, M.H. Wiedmann and C.M. Falco, "Interface magnetic anisotropy in epitaxial superlattices", Phys. Rev. Lett. **67**, 1910 (1991).

[85] M. Getzllaf, *Fundamentals of Magnetism,* Springer-Verlag Berlin Heidelberg (2008).

[86] C.J. Lin, G.L. Gorman, C.H. Lee, R.F.C. Farrow, E.E. Marinero, H.V. Do, H. Notarys, and C.J. Chien, "Magnetic and structural properties of Co/Pt multilayers", J. Magn. Magn. Mater. **93**, 194 (1991).

[87] J.H. Kim and S.C. Shin, "Interface roughness effects on the surface anisotropy in Co/Pt multilayer films", J. Appl. Phys. **80**, 3121 (1996).

[88] M.T. Johnson, P.J.H. Bloemenz, F.J.A. den Broeder, and J.J. de Vries, "Magnetic anisotropy in metallic multilayers", Rep. Prog. Phys. **59**, 1409 (1996).

[89] J.W Knepper and F.Y. Yang, "Oscillatory interlayer coupling in Co/Pt multilayers with perpendicular anisotropy", Phys. Rev. B **71**, 224403 (2005).

[90] N.W.E. McGee, M.T. Johnson, J.J. de Vries, and J. de Stegge, "Localized Kerr study of the magnetic properties of an ultrathin epitaxial Co wedge grown on Pt(111)", J. Appl. Phys. **73**, 3418 (1993).

[91] T. Eimüller, T.C. Ulbrich, E. Amaladass, I L. Guhr, T. Tyliszczak, and M. Albrecht, "Spin-reorientation transition in Co/Pt multilayers on nanospheres", Phys. Rev. B **77**, 134415 (2008).

[92] M.T. Rahman, N.N. Shams, Y. C. Wu, C.H. Lai and D. Suess, "Magnetic multilayers on porous anodized alumina for percolated perpendicular media", Appl. Phys. Lett. **91**, 132505 (2007).

[93] M.T. Rahman, N.N. Shams, C.H. Lai, J. Fidler and D. Suess, "Co/Pt perpendicular antidot arrays with engineered feature size and magnetic properties fabricated on anodic aluminum oxide templates", Phys. Rev. B **81**, 014418 (2010).

[94] N. Siadou, M. Androutsopoulos, I. Panagiotopoulos, L. Stoleriu, A. Stancu, T. Bakas and V. Alexandrakis, "Magnetization reversal in [Ni/Pt]6/Pt(x)/[Co/Pt]6 multilayers", J. Magn. Magn. Mater. **323**, 1671 (2011).

[95] T.C. Ulbrich, D. Assmann and M. Albrecht, "Magnetic properties of Co/Pt multilayers on self-assembled particle arrays", J. Appl. Phys. **104**, 084311 (2008).

[96] P. Weiss, "L'hypothese du champ moleculaire et de la propriete ferromagnetique", J. Phys. **6**, 661 (1907).

[97] F. Bloch, "Zur Theorie des Austauschproblems und der Remanenzerscheinung der Ferromagnetika", Z. Physik **74**, 295 (1932).

[98] L. Néel, "Énergie des parois de Bloch dans les couches minces", C. R. Acad. Sci. **241**, 533 (1955).

[99] J. Frenkel and J. Dorfman, "Spontaneous and induced magnetization in ferromagnetic bodies", Nature **126**, 274 (1930).

[100] H. Frei, S. Shtrikman and D. Treves, "Critical Size and Nucleation Field of Ideal Ferromagnetic Particles", Phys. Rev. **106**, 446 (1957).

[101] H. Kronmüller and M. Fähnle, *Micromagnetism and the Microstructure of Ferromagnetic Solids,* Cambridge University Press (2003).

[102] E.C. Stoner and E.P. Wohlfarth, "A mechanism of magnetic hysteresis in heterogeneous alloys", Phil. Trans. R. Soc. A **240**, 599 (1948).

[103] M Kläui and C.A.F. Vaz, *Magnetization Configurations and Reversal in Small Magnetic Elements, Handbook of Magnetism and Advanced Magnetic Materials,* edited by H. Kronmüller and S. Parkin, vol. 2, part 2, John Wiley and Sons (2007).

[104] T.C. Ulbrich, D. Makarov, G. Hu, I.L. Guhr, D. Suess, T. Schrefl and M. Albrecht, "Magnetization reversal in a novel gradient nanomaterial", Phys. Rev. Lett. **96**, 077202 (2006).

[105] R.H. Victora and X. Shen, "Exchange coupled composite media for perpendicular magnetic recording", IEEE Trans. Magn. **41**, 2828 (2005).

[106] S. Mukherjee and L. Berger, "Switching of composite media by wall propagation", J. Appl. Phys. **99**, 08Q909 (2006).

[107] D. Goll, S Macke and H. Kronmüller, "Exchange coupled composite layers for magnetic recording", Physica B **403**, 338 (2008).

[108] P.E. Kelly, K. O´Gradey, P.I. Mayo and R.W. Chantrell, "Switching mechanisms in cobalt-phosphorus thin films", IEEE Trans. Magn. **25**, 3881 (1989).

[109] E.P. Wohlfarth, "Relations between different modes of acquisition of the remanent magnetization of ferromagnetic particles", J. Appl. Phys. **29**, 595 (1958).

[110] O. Henkel, "Remanenzverhalten und wechselwirkungen in hartmagnetischen teilchenkollektiven" Phys. Stat. Sol. **7**, 919 (1964).

[111] A. Stancu, P.R. Bissell and R.W. Chantrell, "Interparticle interactions in magnetic recording media as obtained from high-order measurements by a Preisach model", J. Appl. Phys. **87**, 8645 (2000).

[112] F. Preisach, "Über die magnetische nachwirkung", Z. Phys. **94**, 277 (1935).

[113] I.D. Mayergoyz, *Mathematical Model of Hysteresis and Their Applications*, Elsevier, Boston (2003).

[114] C.I. Dobrota and A. Stancu, "What does a first-order reversal curve diagram really mean? A study case: Array of ferromagnetic nanowires", J. Appl. Phys. **113**, 043928 (2013).

[115] I. Panagiotopoulos, "A simple approach to the First Order Reversal Curves (FORC) of two-phase magnetic systems", J. Magn. Magn. Mater. **323**, 2148 (2011).

[116] C.R. Pike, A.P. Roberts and K.L. Verosub, "Characterizing interactions in fine magnetic particle systems using first order reversal curves", J. Appl. Phys. **85**, 6660 (1999).

[117] I.D. Mayergoyz, "Mathematical models of hysteresis", Phys. Rev. Lett. **56**, 15 (1986).

[118] I.D. Mayergoyz, "Mathematical models of hysteresis", IEEE Trans. Magn. **22**, 603 (1986).

[119] C.R. Pike, C.A. Ross, R.T. Scalettar and G. Zimanyi, "First-order reversal curve diagram analysis of a perpendicular nickel nanopillar array", Phys. Rev. B **71**, 134407 (2005).

[120] P. Andrei, A. Stancu and O. Caltun, "Differential Preisach model for the description of dynamic magnetization processes", J. Appl. Phys. **83**, 6359 (1998).

[121] A.R. Muxworthy and A.P. Roberts, *First Order Reversal Curve (FORC) Diagrams,* edited by D. Gubblins and E. Herrero-Bervera, Encyclopedia of Geomagnetism and Paleomagnetism, Springer (2007).

[122] E. Della Torre, "Effect of interaction on the magnetization of single domain particles", IEEE Trans. Audio Electroacoust. **14**, 86 (1966).

[123] M. Pardavi-Horvarth, E. Della Torre, F. Vajda and G. Vertesy, "Variable variance Preisach model", IEEE Trans. Magn. **29**, 3793 (1993).

[124] C.R. Pike and A. Fernandez, "An investigation of magnetic reversal in submicron-scale Co dots using first order reversal curve diagrams", J. Appl. Phys. **85**, 6668 (1999).

[125] A. Markou, K.G. Beltsios, L.N. Gergidis, I. Panagiotopoulos, T. Bakas, K. Ellinas, A. Tserepi, L. Stoleriu, R. Tanasa and A. Stancu, "Magnetization reversal in triangular $L1_0$-FePt nanoislands", J. Magn. Magn. Mater. **344**, 224 (2013).

[126] A. Markou, I. Panagiotopoulos, T. Bakas, P. Postolache, L. Stoleriu and A. Stancu, "Magnetization reversal in graded anisotropy Co/Pt multilayers: A first order reversal curve study", J. Appl. Phys. **112**, 123914 (2012).

[127] V. Alexandrakis, D. Niarchos, M. Wolff and I. Panagiotopoulos, "Magnetization reversal in CoPt(111) hard/soft bilayers", J. Appl. Phys. **105**, 063908, (2009).

[128] R. Tanasa, A. Stancu, E. Codjovi, J. Linares, F. Varret and J.F. Létard, "A first order reversal curve investigation of pressure hysteresis in multiferroics spin transition compound", J. Appl. Phys. **103**, 07B905 (2008).

[129] A.P. Roberts, C.R. Pike and L. Verosub, "First-order reversal curve diagrams: A new tool for characterizing the magnetic properties of natural samples", J. Geophys. Res. **105**, 28461 (2000).

[130] F. Brem, L. Tiefenauer, A. Fink, J. Dobson and A.M. Hirt, "A mixture of ferritin and magnetite nanoparticles mimics the magnetic properties of human brain tissue", Phys. Rev. B **73**, 224427 (2006).

[131] M. Ohring, *Materials Science of Thin Films: Deposition and Structure*, Second Edition, Academic Press, New York, USA (2001).

[132] M. Wuttig and X. Liu, *Ultrathin Metal Films: Magnetic and Structural Properties*, Vol. 206, Springer Tracts in Modern Physics, Springer-Verlag Berlin Heidelberg, Germany (2004).

[133] W.R. Grove, "On the electro-chemical polarity of gases", Phil. Trans. R. Soc. Lond. **142**, 87-101 (1852).

[134] K.S. Sree Harsha, *Principles of Physical Vapor Deposition of Thin Films*, Elsevier (2006).

[135] M. Nastasi and J.W. Mayer, *Ion Implantation and Synthesis of Materials,* Springer-Verlag Berlin Heidelberg, Germany (2006).

[136] R.A. Powell and S. Rossnagell, *PVD for Microelectronics: Sputter Deposition Applied to Semiconductor Manufacturing,* Vol. 26, Academic Press (1999).

[137] A. Rockett, *The Materials Science of Semiconductor,* Springer Science and Business Media, LLC, New York (2008).

[138] B.E. Aufderheide, *Sputtered Thin Films Coattings, Coatings Technology: Fundamentals, Testing and Processing Techniques,* edited by A.A Tracton, CRC Press, Taylor and Francis Group (2007).

[139] Y. Lei, S. Yang, M. Wu and G. Wilde, "Surface patterning using templates: Concept, properties and device applications", Chem. Soc. Rev. **40**, 1247-1258 (2011).

[140] R. Giunebretière, *X-Ray Diffraction by Polycrystalline Materials,* ISTE Ltd, London, UK (2007).

[141] W.D. Callister, Jr., *Materials Science and Engineering, An Introduction,* Seventh Edition, John Wiley and Sons Inc. (2007).

[142] W. Borchardt-Ott, *Crystallography, An Introduction,* Third Edition, Springer-Verlag Berlin Heidelberg (2011).

[143] M. Birkholz, *Thin Films Analysis by X-Ray Scattering,* WILEY-VCH Verlag GmbH & Co. KGaA, Weinheim (2006).

[144] K. Nagao and E. Kagami, "X-Ray thin films measurement techniques: VII. Pole figure measurement", The Rigaku Journal **27**, 2 (2011).

[145] P.M. Martin, *Handbook of Deposition Technologies for Films and Coatings: Science, Applications and Technology,* Third Edition, Elsevier Inc (2009).

[146] F. Huang, "X-ray reflectivity studies of thin film", Internal Report, Center for Materials for Information Technology, An NSF Science and Engineering Center.

[147] L. Névot and P. Croce, "Caractérisation des surfaces par réflexion rasante de rayons X. Application l'ètude du polissage de quelques verres silicates", Rev. Phys. Appl. **15**, 761 (1980).

[148] E.N. Kaufmann, "*Characterization of Materials"*, Vol. 1, John Wiley and Sons, New Jersey (2003).

[149] K. Maeda and H. Mizubayashi, *Nanoscopic Architecture and Microstructure, Handbook of Materials Measurement Methods,* edited by H. Czichos, T. Saito and L. Smith, chapter 5, pp. 153–228, Springer Science & Business Media, Inc, Stürz AG, Würzburg (2006).

[150] S. Horiuchi and L. He, *High-Resolution Transmission Electron Microscopy, Characterization of High T_c Materials and Devices by Electron Microscopy*, edited by D. Browning and S.J. Pennycook, Cambridge University Press, Cambridge, U.K. (2004).

[151] G. Binning, C.F. Quate and C. Gerber, "Atomic force microscope", Phys. Rev. Lett. **56**, 930 (2006).

[152] F. Rico, E.P. Wojcikiewicz and V.T. Moy, *Atomic Force Microscopy Studies of the Mechanical Properties of Living Cells, Applied Scanning Probe Methods IX,* edited by B. Bhushan, H. Fuchs and M. Tomitori, Springer-Verlag Berlin Heildeberg (2008).

[153] K.H.J. Buschow and F.R. De Boer, *Physics of Magnetism and Magnetic Materials,* Kluwer Academic Publishers, London (2004).

[154] C.D. Graham, "High-sensitivity magnetization measurements", J. Mater. Sci. Technol **16**, 2 (2000).

[155] Y.M. Hu, J.C. Huang, C.W. Chen, C.H. Lee, M.J. Lin, "Perpendicilar magnetization of epitaxial $CrPt_x$ films", J. Appl. Phys. **98**, 013901 (2005).

[156] A. Borgschulte, D. Zur, D. Menzel, J. Schoenes and P. M. Oppeneer, "Effects of the stoichiometry and chemical order on the electronic structure and magnetic properties of Cr-Pt alloys probed by angular-resolved photoemission", Phys. Rev. B **66**, 144421 (2002).

[157] M. Broschwitz, S. Knetsch, A. Borgschulte, L. Bizdoaca, and J. Schoenes, "Size effects of optical and magneto-optical properties of epitaxial $CrPt_3$ films", J. Appl. Phys. **93**, 2458 (2003).

[158] K. Takanashi, S. Mitani, M. Sano, H. Fujimori, H. Nakajima, and A. Osawa, "Artificial fabrication of an $L1_0$-type FeAu alloy by alternative monoatomic deposition", Appl. Phys. Lett. **67**, 1016 (1995).

[159] N.I. Vlasova, G.S. Kanadaurova, N.N Shchegoleva "Effect of the polytwinned microstructure parameters on magnetic domain structure and hysteresis properties of the CoPt-type alloys", J. Magn. Magn. Mater. **222**, 138 (2000).

[160] M.F. Toney, W.Y Lee, J.A. Hedstrom and A. Kellock, "Thickness and growth temperature dependence of structure and magnetism in FePt films", J. Appl. Phys. **93**, 12 (2003).

[161] N.S. Kurkakov, S.F. Zhemchuzhny and M.I. Zasedatelev, J. Inst. Metals **15**, 305 (1916).

[162] D.W. Pashley and A.E.B. Presland, "The observation of antiphase boundaries during the transition from CuAu I to CuAu II", J. Inst. Metals **87**, 419 (1959).

[163] M. Hirabayashi and S. Weissmann, "Study of CuAu I by transmission electron microscopy", Acta Met. **10**, 25 (1962).

[164] S. Farjami, M. Yasui, T. Fukuda and T. Kakeshita, " Selected formation of a variant in $L1_0$-type CoPt realized by ordering heat treatment under a magnetic field", Scr. Mater. **58**, 811 (2008).

[165] R.F.C. Farrow, D. Weller, R.F. Marks, M.F. Toney, A. Cebollada and G.R. Harp, "Control of the axis of chemical ordering and magnetic anisotropy in epitaxial FePt films", J. Appl. Phys. **79**, 5967 (1996).

[166] V. Karanasos, I. Panagiotopoulos, D. Niarchos, H. Okumura and G.C. Hadjipanayis, "CoPt/Ag nanocomposites with (001) texture", Appl. Phys. Lett. **79**, 1255 (2001).

[167] Y.N. Hsu, S. Jeong, D.E. Laughlin and D.N. Lamberth, "Effects of Ag underlayers on the microstructure and magnetic properties of epitaxial FePt thin films", J. Appl. Phys. **89**, 7068 (2001).

[168] X.H. Xu, T. Jin, H.S. Wu, F. Wang, X.L. Li and F.X. Jiang, "Nearly perfect (001)-oriented Ag/$[CoPt/C]_5$/Ag composite films deposited on glass substrates", Thin Solid Films **515**, 5471 (2007).

[169] A. Breitling and D. Goll, "Hard magnetic $L1_0$ FePt thin films and nanopatterns", J. Magn. Magn. Mater. **320**, 1449 (2008).

[170] H. Zeng, M.L. Yan, N. Powers and D.J. Sellmyer, "Orientation controlled nonepitaxial $L1_0$ CoPt and FePt films", Appl. Phys. Lett. **80**, 2350 (2002).

[171] X.H. Xu, X.H. Shen, X.L. Li, F. Wang, F.X. Jiang and H.S. Wu, "Texture development and magnetic properties of $[ZrO_2/CoPt]_n$/Ag nanocomposite films", Appl. Surf. Sci. **253**, 3382 (2007).

[172] B.Z. Cui, K. Han, D.S. Li, H. Garmestani, J.P. Liu, N.M. Dempsey and H.J. Scnhneider-Muntau, "Magnetic field induced crystallographic texture enhancement in cold-deformed FePt nanostructured magnets", J. Appl. Phys**. 100**, 013902 (2006).

[173] T. Ichitsubo, S. Tojo, T. Uchihara, E. Matsubara, A. Fujita, K. Takahashi and K. Watanabe, "Mechanism of c-axis orientation of $L1_0$ FePt in nanostructured FePt/B_2O_3 thin films", Phys. Rev. B **77**, 094114 (2008).

[174] S. Fahler, V. Neu, M. Weisheeit, U. Hannemann, S. Leinert, A. Singh, A. Kwon, S. Melcher, B. Holzapfel, L. Schultz, "High Performance Thin Film Magnets", 18th Workshop on High Performance Magnets & their Applications, p.566, Annecy, France (2004)

[175] N.P. Suponev, R.M. Grechishkin, M.B. Lyakhova, Yu.E. Pushkar, "Angular dependence of coercive field in (Sm,Zr) $(Co,Cu,Fe)_z$ alloys", J. Magn. Magn. Mat. **157**, 376 (1996).

[176] A. Markou, I. Panagiotopoulos and T. Bakas, "Effects of layering and magnetic annealing on the texture of CoPt films", J. Magn. Magn. Mater. **322**, L61 (2010).

[177] J.-S. Kim, Y.-M. Koo, B.-J. Lee and S.-R. Lee, "The origin of (001) texture evolution in FePt thin films on amorphous substrates", J. Appl. Phys. **99,** 053906 (2006).

[178] J.-S. Kim and Y.-M. Koo, "Thickness dependence of (001) texture evolution in FePt thin films on an amorphous substrate", Thin Solid Films **516,** 1147 (2008).

[179] I.C. Noyan, T.C. Huang and B.R. York, "Residual stress/strin analysis in thin films by X-ray diffraction", CRC Crit. Rev. in Solid State and Mater. Sci. **20**(2), 125 (1995).

[180] M. van Leeuwen, J.-D. Kamminga, and E.J. Mittemeijer, "Diffraction stress analysis of thin films: Modeling and experimental evaluation of elastic constants and grain interaction", J. Appl. Phys. **86,** 1904 (1999).

[181] A. Cazzani, M. Rovati, "Extrema of Young's modulus for elastic solids with tetragonal structure", Int. J. Solids and Struct. **42,** 5057 (2005).

[182] http:/gwyddion.net/

[183] http:/imagej.nih.gov/ij/

[184] R.P. Feynmann, R.B. Leighton and M. Sands, "The discussion on the Bragg-Nye Crystal model", The Feynmann lectures on Physics, Addison-Wesley Publishing, California Institute of Technology Massachusetts, Menlo Park, California, London, Sydney, Manila, 1981 (15^{th} printing, Chapter 30, section 9).

[185] E.W. Rothe, R.J. Baird, C.W. Manke and R. Piparia, "Organic nanostructures on silicon created with semitransparent spheres and 248nm laser pulses", Nanotechnology **19**, 165301 (2008).

[186] W.H. Walton, "Feret's statistical diameter as a measure of particle size", Nature **162**, 329 (1948).

[187] Y. Tsunoda and H Kobayashi, "Temperature variation of the tetragonality in ordered PtFe alloy". J. Magn. Magn. Mater. 272, 776 (2004).

[188] T. J. Klemmer, N. Shukla, C. Liu X.W. Wu, E.B. Svedberg, O. Mryasov, R.W. Chantrell, D. Weller, M. Tanase and D.E. Laughlin, Appl. Phys. Lett. **81**, 2220 (2002).

[189] Y.S. Yu, H.-B. Li, W.L. Li, M. Liu, Y.-M. Zhang, W.D. Fei and D.J. Sellmyer, "Low temperature ordering of FePt films by in-situ heating deposition plus post deposition annealing", Thin Solid Films **518**, 2171 (2010).

[190] A. Markou, I. Panagiotopoulos, T. Bakas, D. Niarchos, G. Safran, W. Li and G.C. Hadjipanayis, "Formation of $L1_0$ with (001) texture in magnetically annealed Co/Pt multilayers, J. Appl. Phys. **110**, 083903 (2011).

[191] P.I. Mayo, K. O'Grady, P.E. Kelly, J. Cambridge, I.L. Sanders, T. Yogi and R.W. Chantrell, "A magnetic evaluation of interaction and noise characteristics of CoNiCr thin films", J. Appl. Phys. **69**, 4733 (1991).

[192] R. Skomski and D.J. Sellmyer, "Cooperative magnetism and Preisach model", J. Appl. Phys. **89**, 7263 (2001).

[193] A. Stancu, C. Pike, L. Stoleriu, P. Postolache and D. Cimpoesu, "Micromagnetic and Preisach analysis of the First Order Reversal Curves (FORC) diagram", J. Appl. Phys. **93**. 6620 (2003).

[194] M. Winklhofer and G.T. Zimanyi, “Extracting the intrinsic switching field distribution in perpendicular media: A comparative analysis”, J. Appl. Phys. 93, 08E710 (2006).

[195] I.D. Mayerdoyz, *Mathematical Models of Hysteresis and Their Applications*, Academic Press, New York (2003).

[196] S. Blomeier, B. Hillebrands, B. Reuscher, A. Brodyanski, M. Kopnarski and R.L. Stamps, “Exchange interaction and magnetic domain formation in periodically inhomogeneous magnetic media”, Phys. Rev. B **77**, 094405 (2008).

[197] S.E. Russek and W.E. Bailey, “Magnetic domain structure and imaging of Co-Pt multilayer thin-film nanostructures”, IEEE Trans. Magn. **36**, 2990 (2000).

[198] S. Okamoto, N. Kikichi, T. Kato, O. Kitakami, K. Mitsuzuka, T. Shimatsu, H. Muraoka, H. Aoio and J.C. Lodder, “Magnetization behavior of nanomagnets for patterned media application”, J. Magn. Magn. Mater. **320**, 2874 (2008).

[199] W. Scholz, J. Fidler, T. Schreff, D. Suess, R. Dittrich, H. Forster and V. Tsiantos, “Scalable parallel micromagnetic solvers for magnetic nanostructures”, Comp. Mater. Sci. **28**, 366 (2003).

[200] S. Okamoto, N. Kikuchi, O. Kitakami, T. Mizayaki, Y. Shimada and K. Fukamichi, “Chemical-order-dependent magnetic anisotropy and exchange stiffness constant of FePt (001) epitaxial films”,

[201] R. Skomski, G.C. Hadjipanayis and D.J. Sellmyer, “Graded permanent magnets”, J. Appl. Phys. **105**, 07A733 (2009).

[202] V. Alexandrakis, T. Speliotis, E. Manios, D. Niarchos, J. Fidler, J. Lee and G. Vargaro, “Hard/graded exchange spring composite media based on FePt”, J. Appl. Phys. **109**, 07B729 (2011).

[203] J.-L. Tsai, H.-T. Tzeng and B.-F. Liu, “Magnetic properties and microstructure of graded Fe/FePt films”, J. Appl. Phys. **107**, 113923 (2010).

[204] V. Bonanni, Y.Y. Fang, R.K. Dumas, C.L. Zha, S. Bonetti, J. Nogués and J. Åkerman, “First-order reversal curve analysis of graded anisotropy FePtCu films”, Appl. Phys. Lett. **97**, 202501 (2010).

[205] B.J. Kirby, J.E. Davies, K. Liu, S.M. Watson, G.T. Zimanyi, R.D. Shull, P.A. Kienzle and J.A. Borchers, “Vertically graded anisotropy in Co/Pd multilayers”, Phys. Rev. B. **81**, 100405 (2010).

[206] C. Kooy and U. Enz, "Experimental and theoretical study of the domain configuration in thin layers of $BaFe_{12}O_{19}$", Philips Res. Rep. **15**, 7-29 (1960).

[207] H.J.G. Draaisma and W.J.M. Jonge, "Magnetization curves of Pd/Co multilayers with perpendicular anisotropy", J. Appl. Phys. **62**, 3318 (1987).

[208] A. Hubert and R. Schäfer, *Magnetic Domains: The Analysis of Magnetic Microstructures*, Springer-Verlag, Berlin (1998).

[209] M.T. Johnson, P.J.H. Bloomen, F.J.A den Broeden and J.J. de Vries, "Magnetic anisotropy in metallic multilayers", Rep. Prog. Phys. **59**, 1409 (1996).

[210] J.E. Davies, O. Hellwing, E.E. Fullerton, G. Denbeaux, J.B. Kortright and K. Liu, "Magnetization reversal of Co/Pt multilayers: Microscopic origin of high-field magnetic irreversibility", Phys. Rev. B **70**, 224434 (2004).

[211] J.E. Davies, O. Hellwing, E.E. Fullerton, J.S. Jiang, S.D. Bader, G.T. Zimányi and K. Liu, "Anisotropy dependence of irreversible switching in Fe/SmCo and FeNi/FePt exchange spring magnet films", Appl. Phys. Lett. **86**, 262503 (2005).

[212] J.E. Davies, P. Morrow, C.L. Dennis, J.W. Lau, B. McMorran, A. Cochran, J. Unguris, R.K. Dumas, P. Greene and K. Liu, "Reversal of patterned Co/Pd multilayers with graded magnetic anisotropy", J. Appl. Phys. **109**, 07B909 (2011).

[213] R.K. Dumas, C.-P. Li, I.V. Roschin, I.K. Schuller and K. Liu, "Magnetic fingerprints of sub-100nm Fe dots", Phys. Rev. B **75**, 134405 (2007).

[214] N. Kikuchi, T. Kato, S. Okamoto, O. Kitakami, N. Tezuka and S. Sugimoto, "Magnetization reversal process and bistability of Co/Pt multilayer dot", J. Appl. Phys. **103**, 07C510 (2008).

List of Publications

1. A. Malainou, K. Tsougrni, K. Ellinas, P.S. Petrou, V. Constantoudis, E. Sarantopoulou, K. Awsiuk, A. Bernasik, A. Budkowski, A. Markou, I. Panagiotopoulos, S.E. Kalabakos, E. Gogolides and A. Tserepi
   "Plasma-Assisted Nanoscale Protein Patterning on Si Substrares via Colloidal Lithography"
   Journal of Physical Chemistry A **117**, 13743 (2013)

2. A. Markou, K.G. Beltsios, l.N. Gergidis, I. Panagiotopoulos, T. Bakas, K. Ellinas, A. Tserepi, L. Stoileriu, R. Tanasa and A. Stancu
   "Magnetization Reversal in Triangular $L1_0$-FePt Nanoislands"
   Journal of Magnetism and Magnetic Materials **344**, 224 (2013)

3. A. Markou, I. Panagiotopoulos, T. Bakas, P. Postolache, L. Stoleriu and A. Stancu
   "Magnetization Reversal in Graded Anisotropy Co/Pt multilayers: A First Order Reversal Curve study"
   Journal of Applied Physics **112**, 123914 (2012)

4. A. Markou, I. Panagiotopoulos, T. Bakas, D. Niarchos, G. Sáfrán, W.F. Li and G.C. Hadjipanayis
   "Formation of $L1_0$ with (001) Texture in Magnetically Annealed Co/Pt Multilayers"
   Journal of Applied Physics **110**, 083903 (2011)

5. A. Markou, I. Panagiotopoulos and T. Bakas
   "Effects of Layering and Magnetic Annealing on the Texture of CoPt Films"
   Journal of Magnetism and Magnetic Materials **322**, L61 (2010)

List of Conferences

1. A. Markou, K.G. Beltsios, I. Panagiotopoulos, A. Tserepi and T. Bakas
   "FePt Nanostructures Obtained by Polystyrene Sphere Array Masks"
   XXVIII Panhellenic Conference on Solid State Physics and Magnetic Materials, Patra, September 23-26, 2012 (Oral)

2. A. Markou, I. Panagiotopoulos and T. Bakas
   "Magnetic Annealing of CoPt Films and Co/Pt bilayers"
   XXVI Panhellenic Conference on Solid State Physics and Magnetic Materials, Ioannina, September 26-29, 2010 (Poster)

3. A. Markou, K.G. Beltsios, I. Panagiotopoulos, M.E. Vlachopoulou, A. Tserepi, V. Alexandrakis, T. Bakas and T. Dimopoulos
   "Magnetic Thin Films Deposited on PDMS Nanotemplates"
   XXV Panhellenic Conference on Solid State Physics and Magnetic Materials, Thessaloniki, September 20-23, 2009 (Poster)